# Charge Transport in Single Cooper-Pair Transistors

Zur Erlangung des akademischen Grades eines
DOKTORS DER NATURWISSENSCHAFTEN
der Fakultät für Physik des
Karlsruher Institut für Technologie (KIT)

genehmigte

DISSERTATION

von

**M. sc. Wanyin Cui**
aus Jiangsu, China

Tag der mündlichen Prüfung: 19. Juli 2010

Referent: Prof. Dr. Hilbert von Löhneysen
Korreferent: Prof. Dr. Alexey Ustinov

# Charge Transport in Single Cooper-Pair Transistors


## Abstract

This thesis describes fabrication, measurements and analysis of single Cooper pair transistor. The samples have been produced using optical lithography, electron beam lithography and shadow evaporation technique. The samples have been investigated in a $^3$He/$^4$He-dilution refrigerator with a base temperature below 20mK by measuring their IV characteristics.

The aim of this work has been to study the physical mechanism for different subgap features and switching currents of the single Cooper pair devices. So the samples have been investigated both in the finite voltage bias regime and with current bias in the supercurrent regime. In the voltage bias regime, the current features are caused by tunneling and cotunneling processes of Cooper pairs and quasiparticles and the subgap features we observe can be well understood by using a simple theoretical model. At the temperatures of our experiments, quasiparticles should be frozen out and pure $2e$ periodicity is expected for the switching current experiments. Nevertheless, we observe considerable quasiparticle poisoning hinting to an unknown source of unequilibrium excitations in accord with observations by other authors.

# Contents

# 1 Introduction

In this thesis, we study single charge effects in the single Cooper pair transistor (CPT) which is the superconducting version of the single electron transistor (SET).

Single charge effects originate from the quantized nature of charges and can readily be measured due to the achievements of nano fabrication technology. Many groups around the world try to utilize this single charge effects for fascinating experiments, e.g. quantum information processing. But are they really feasible in reality? Based on this question, we started to study the single Cooper pair transistor and try to contribute to the understanding of the basic physics of these devices.

For the SET, the island carries integer numbers of excess charges at low temperatures. The current through the SET results from sequential tunneling of single electrons through both junctions. Each tunneling event occurs at a rate which depends on the electrostatic energy change it creates and the transparency of the junctions. Since the electrostatic energy of the island depends on the gate voltage, the current through the whole device is modulated by the gate voltage.

The superconducting case is much more complicated than that. Upon the formation of Cooper pairs, a periodicity corresponding to the number change of Cooper pairs emerges. In the past decade, a lot of theoretical and experimental work has been devoted to the study of single charge transport properties of single Cooper pair transistors at finite voltage bias and many interesting phenomena have been observed, such as Cooper pair tunneling and the Josephson quasiparticle cycle. The coexistence of Cooper pairs and quasiparticles makes it much more difficult to describe the system theoretically.

We focus on the sub-gap features at finite bias voltage including the supercurrent features at zero bias voltage. The single Cooper pair transistor behaves identical to a single Josephson junction with an effective coupling energy $E_j$ which is tunable with the gate voltage $V_g$. We expect a $2e$ periodic dependence of $I(V_g C_g)$. Unfortunately only a couple of experiments showed $2e$ features while in many cases pure $e$ periodic behavior has been found. This is due to the omnipresence of spurious quasiparticles.

This work is organized as follows: In the second chapter, we start with the introduction of single electron devices and Josephson junctions. Then we theoretically study the single Cooper pair transistor, verifying that it behaves with respect to the supercurrent identical to the single Josephson junction with an effective coupling depending on the gate voltage $E_j = E_j(C_g V_g)$. We also describe the bias voltage and gate voltage dependent current features at finite voltage bias regime.

In the third chapter, we describe in detail the fabrication of single charge devices, including optical lithography, electron beam lithography, and shadow evaporation. In chapter four, we explain our experimental setup, focusing on the filtering of electrical noise. The fabrication procedure of metal powder filters is also introduced in this chapter.

The experimental results are presented in chapter five. Parameter characterization is given at the beginning, making use of different sub-gap features which occur at known positions. Measurements with a finite voltage bias of the single Cooper pair devices come second, indicating interesting Cooper pair and quasiparticle tunneling features. Finally, we show the results of switching current measurements with focus on the quasiparticle poisoning of the islands.

We close this work in chapter six with a summary and discussion of our study of single Cooper pair transistors.

# 2 Theoretical background

A detailed description of charge transport in single electron devices can be found in several textbooks (e. g. Grabert and Devoret (1992); Averin and Likharev (1991)). In this chapter we restrict ourselves to a short outline of those aspects relevant to the experiments described later in this work. Samples are prepared from aluminum, which becomes superconducting below 1.2 Kelvin. However, all samples can be forced to the normal-conducting state by means of a magnetic field (For our nano scaled devices, a magnetic field of the order of 1 Tesla is required). To determine important device parameters it is sometimes favorable to suppress superconductivity and we will touch slightly on normal conducting devices in several chapters throughout this work. Therefore, we start off in Sec. 2.1 with a description of the most fundamental single electron device, namely the normal-conducting single electron transistor, thereby introducing the concept of charging energy, the most fundamental theoretical treatment (Sec. 2.1.1), and corrections to it necessary for a better agreement with experimental facts (Sec. 2.1.2). In Sec. 2.2 we turn to the central feature of the devices in the superconducting state and describe the so called Josephson effect of ultra-small junctions in the strong damping limit. As an example for a superconducting device we focus in Sec. 2.3 on the single Cooper-pair transistor.

## 2.1 The single electron transistor in the normal-conducting state

The basis for devices showing single charge transport phenomena of the type we are going to describe in this section are small tunnel junctions interconnecting a system of metallic electrodes. In Chap. 3 we describe one of the standard methods to fabricate such tunnel contacts from aluminum with which the tunneling barriers are formed by an oxide layer naturally growing on the surface when exposing the aluminum to oxygen. In this way high quality junctions with barriers as thin as about 2 nm and electrodes as small as about 20 nm by 20 nm in size can be structured. If such a tunneling contact is cooled down to very low temperature, and if superconductivity is suppressed by a sufficient magnetic field, and if the contact is biased by a voltage $V$ it will respond by a current $I$ obeying Ohm's law, $I = GV$, to very high accuracy.

Besides the conductance $G$, the contact is characterized by a small capacitance $C$, which is geometrically defined by the electrodes separated by the dielectric constituting the tunneling barrier. The capacitance $C$ sets an important energy scale $E_c = e^2/2C$, nicknamed charging energy, which denotes the energy required to charge up $C$ by an elementary charge $e$. For tunneling contacts as small as routinely patterned in modern labs, the charging energy—when expressed as a temperature $T_c = E_c/k_B$—can be as large as several Kelvin and is thus easily accessible by cryogenic methods. However, as long as the voltage across the contact is kept constant by means of an external source, $E_c$ does not alter the Ohmic response of the contact in

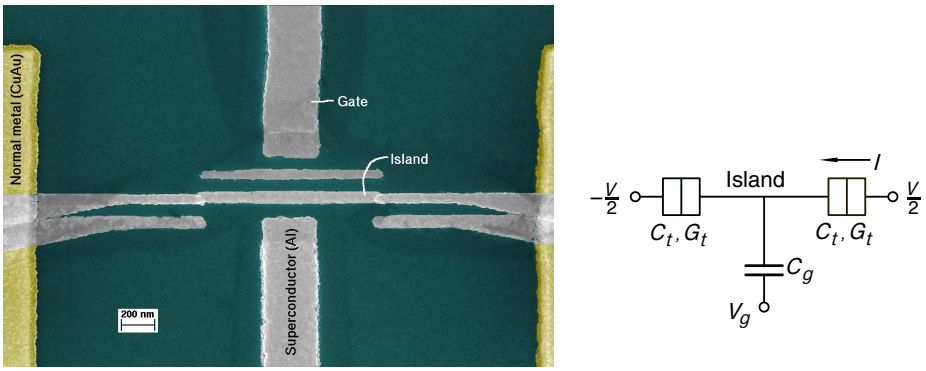


Figure 2.1: Left: Scanning electron microscope (SEM) photo of a single electron transistor. The tunneling contacts can be seen at the junction between the island and the leads. Right: Schematic representation of a voltage biased single electron transistor. The boxes represent tunneling contacts characterized by a capacitance $C_t$ and a conductance $G_t$. The gate can be seen as a capacitance of size $C_g$ coupled to the island.

any noticeable way. The source keeps the mean charge on $C$ constant and the quantized nature of charge manifests itself only in the noise properties of the current flow.

The situation is fundamentally different when we switch from a voltage biased situation to a current biased setup. A constant current $I$ charges up the capacitance $C$ thereby increasing the voltage across it according to $\Delta V = I\Delta t/C$. At the same time the energy stored in the capacitance grows as $E = (I\Delta t)^2/2C$. After a certain time $t_0$ the energy can be lowered by tunneling of an electron across the junction, which—since tunneling is a fast process—all of a sudden changes the charge from $I\Delta t$ to $I\Delta t - e$. It is easy to see that $t_0 = e/2I$ holds. For $\Delta t > t_0$ we gain energy through tunneling, while for $\Delta t < t_0$ we have to pay energy. In the limes of zero temperature tunneling is thus blocked for times before $t_0$ and becomes more and more likely when time passes $t_0$. After tunneling the charging continues leading to a series of tunneling events at times just after $t_n = (n + 0.5)e/I$. For the voltage we expect a sawtooth like behavior: a linear increase interrupted by sudden drops (of size $\Delta V = e/C$) around $t_n$. The mean frequency is given by $f = I/e$ which relates current via a fundamental constant to a quantity which can be measured with extreme precision. In the last two decades considerable interest in a realization of this current-to-frequency conversion can be noticed.

The concept of current bias, while extremely simple in theory, is extremely difficult to realize in experiment. A careful design of the environment which is connected to the sample is needed. The crucial point is the impedance of the environment as seen by the contact in the sense of Thévenin's equivalent circuit (Thévenin, 1883). This impedance should approach virtually infinity for a good current bias while in most practical cases and without a careful design it is dominated by the stray capacitance of the connecting leads which tends to fix the voltage across the contact and always favors an effectively voltage biased situation.

The simplest way around this problem is to structure more than one contact in close proximity forming islands in-between as exemplified in Fig. 2.1 for two serially connected contacts. In

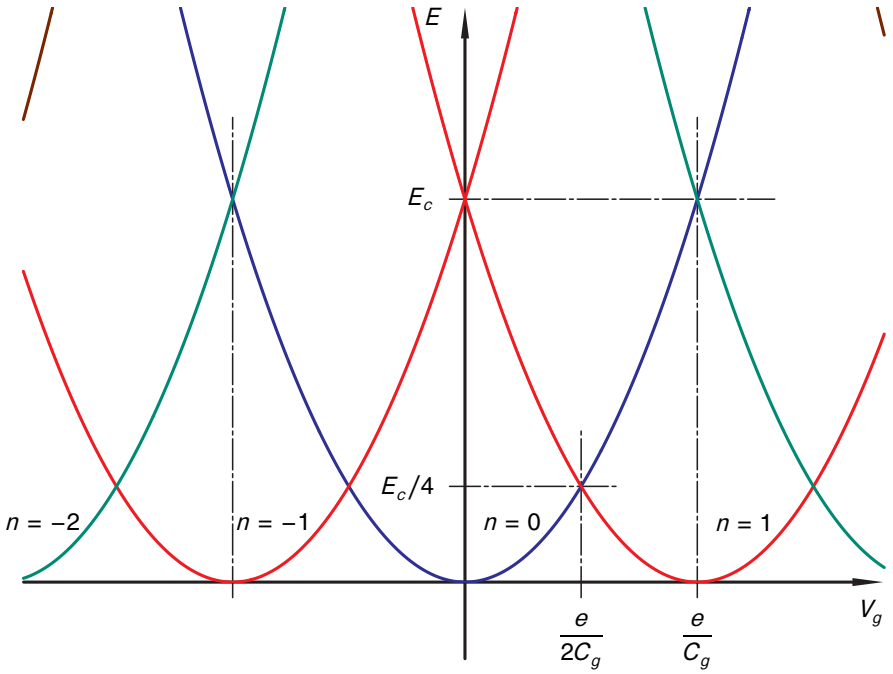


Figure 2.2: Dispersion of the energy of charge states as a function of the gate voltage $V_g$ for a SET. The charge number is indicated close to the individual parabola.

this case the impedance seen by any junction is dominated by the ohmic impedance of the adjacent contacts. Since structuring requires nanoscale resolution anyhow, it turns out to be easy to fabricate microscopic islands with a total capacitance $C_\Sigma$ ($C_\Sigma$ equals the sum of all the capacitance values coupled to the island) which still obeys $E_c = e^2/2C_\Sigma < k_B T$. Then single charge effects are readily observable even when the whole device is tested for current response in a voltage biased mode.

It is for this reason that the basic device of single charge tunneling electronics is not a single contact; it is rather the single electron transistor (SET) imaged in Fig. 2.1 in the voltage biased mode. Major constituents are tunneling contacts on two sides of a small island with total capacitance $C$. In addition at least one gate electrode (in the SEM micrograph of Fig. 2.1 we have two) couples to the island capacitively (i. e. without the possibility to exchange charge between this electrode and the island). Gate electrodes can be used to tune the electrostatic potential on the island.

In case the conductance $G$ of the tunneling contacts is small, we are faced with a situation where the charge on the island is most of the time an integer number $n$ times the elementary charge $e$. The number $n$ might change eventually by tunneling events. However, this is a rare event first due to smallness of $G$ and second because tunneling is an extremely fast process[1]. It

[1] We are going not into details on how to approximate the time it takes for an electron to tunnel. We just state the fact, that this is the smallest timescale in our problem which we cannot detect in our experiments.

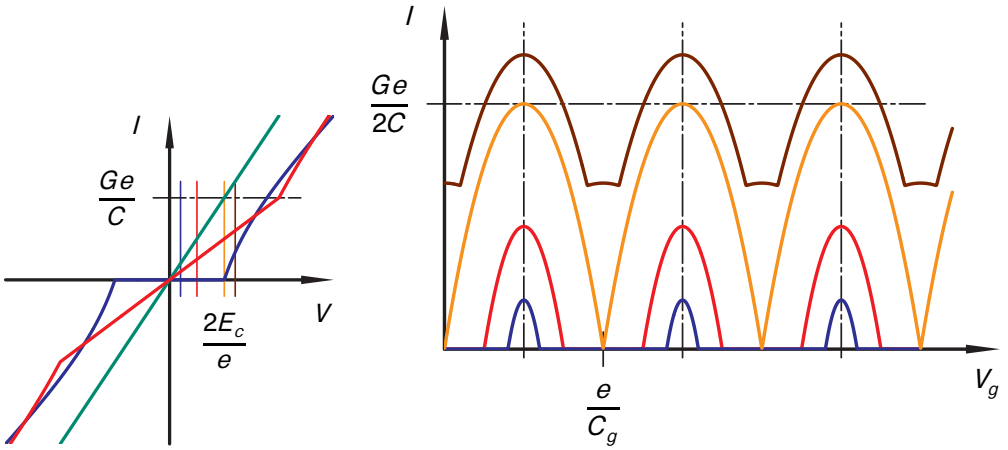


Figure 2.3: Characteristics of a symmetric single electron transistor as predicted by the sequential tunneling model. Left: I-V characteristics at $T \gg T_c$ (green) and zero temperature ($V_g = ne/C$ (blue) and $V_g = (n + 1/2)e/C$ (red)). Right: Coulomb oscillations (at $T = 0$) of the current through a single electron transistor as a function of $V_g$ for constant voltage bias. The bias voltages are indicated in the left part of the figure as vertical lines.

is common to characterize the state of the system by the number $n$ and call such states "charge states". The energy of the charge state depends in a parabolic way[2] on the gate voltage as indicated in Fig. 2.2 for the case of vanishing bias voltage, $V = 0$. The energetically most favorable state close to $V_g = 0$ is the uncharged one ($n = 0$). At $V_g > e/2C_g$ the system can lower its energy by tunneling an electron across one of the tunnel junctions to change the island charge. At low temperature, when the system is in its ground state, the charge on the island is fixed, except close to the degeneracy points where two adjacent charge state parabola cross each other. The linear response conductance is thus zero if the gate voltage does not obey $V_g \sim (n + 1/2)e/C_g$. Transport is blocked, an effect which is nicknamed "Coulomb blockade". Fig. 2.3 displays the behavior of a symmetric SET at finite bias. On the left I-V characteristics for different situations are shown. The low temperature behavior is compared to the ohmic characteristic (green) observed at elevated temperatures $T \gg T_c$. The blue curve indicates the Coulomb blockade at $|V| < 2E_c/e$ as expected for $V_g = ne/C_g$. The blockade is lifted when $V_g$ is tuned to $V_g = (n + 1/2)e/C_g$ as shown by the red curve. Note that the linear response conductance equals half the high temperature value in this case. In the right half of the figure we fixed the bias voltage at different values and display the current as a function of $V_g$. We see a periodic variation of the current with frequency $C_g/e$, commonly named "Coulomb oscillations". At small bias the current differs from zero only in narrow regions around $V_g = (n + 1/2)e/C_g$. At higher bias voltage the blockade is lifted; a periodic variation of the current $I$ remains, though.

[2] More precisely we have: $E_n(V_g) = E_c(n - C_g V_g/e)^2$ if $V = 0$.

### 2.1.1 Sequential tunneling model

Fig. 2.3 is evaluated using the so called "sequential tunneling model" (Averin and Likharev (1991)). This model—often referred to as "orthodox theory"—was developed to explain the basic phenomena associated with single electron charging effects of a system of small island coupled to $m$ external reservoirs. The Hamiltonian of such a device is split into three parts $H = H_{\mathrm{qp}} + H_t + H_{\mathrm{el}}$, where $H_{\mathrm{qp}}$ treats the electronic states on the island and in the reservoirs[3], $H_t$ describes the tunneling of electrons through the various tunneling contacts, and $H_{\mathrm{el}}$ is set up to treat the electrostatic part of the problem. For the latter the tunnel contacts are modeled by plain capacitances. As deduced in App. A, $H_{\mathrm{el}} = E_c(\hat{n}-n_0)^2$ for the transistor. Here $\hat{n}$ is treated as an operator in the quantum mechanical sense. The eigenstates of $H_{\mathrm{el}}$ are the charge states introduced in the last section, and the eigenvalue of $\hat{n}$ equals the number of electrons in the particular charge state. The variable $n_0$ is in the simplest case directly proportional to the gate voltage, $n_0 = (C_g/e)V_g$. In reality, one finds an offset of $n_0$, i. e. $n_0$ does not vanish at $V_g = 0$ but is of order unity. This effect is attributed to charges trapped close to the island (either in the substrate or in the oxide layer covering the island). These so called "background charges" result in an image charge on the island, and thus contribute to $n_0$. Background charges represent a major drawback for the applicability of single charge devices mainly since the position of some of them is not stable in time even at the lowest temperatures. In real devices $n_0$ undergoes jumps of order unity on a timescale of typically several hours or less which are attributed to the rearrangement of background charges. On shorter time scales moving background charges are held responsible for the excessively large 1/f noise in single charge devices.

The tunneling Hamiltonian $H_t$ mixes charge states and the sequential tunneling model treats this mixing pertubatively in lowest order. As indicated by its name, tunneling events are considered as independent of each other and it is implicitly assumed that electrostatic equilibrium is established quickly between successive events. The rate of tunneling events connecting two specific initial and final charge states is estimated in accord with Fermi's golden rule:

$$\Gamma = \frac{2\pi}{\hbar}|\langle \mathrm{fi}|H_T|\mathrm{in}\rangle|^2\delta(\Delta E)$$

Here $\Delta E = E_{\mathrm{in}} - E_{\mathrm{fi}}$ equals the change in electrostatic energy between the initial and final state. In case the tunneling is between an external reservoir and an island this change in energy includes work done or absorbed by the electromotive force of connected batteries (see App. A). The above equation gives with $\beta = 1/k_B T$

$$\Gamma = \frac{g}{h}\frac{\Delta E}{\exp(\beta\Delta E) - 1}. \tag{2.1}$$

This result is depicted in Fig. 2.4. The rate is proportional to the conductance $G$ of the involved tunneling contact in the voltage biased mode in units of $G_0 = e^2/h$, $g = G/G_0$. The above

[3] For normal-conducting devices this states are for the current purpose sufficiently well characterized by a Fermi distribution $f(\epsilon) = 1/\left(1 + \exp\left(\beta\left(\epsilon - \mu\right)\right)\right)$. This also implies that we treat the electronic states as a continuum. In general the electronic states on a small island have a discrete spectrum. However, the level spacing is much smaller than the thermal energy for the metallic islands discussed here.

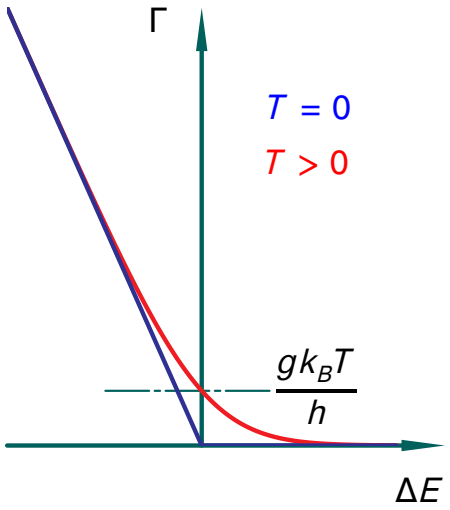


Figure 2.4: Tunneling rate versus electrostatic energy difference $\delta E$. At $T = 0$, the rate vanishes for positive $\Delta E$ as required by energy conservation. Thermal fluctuations make tunneling possible even for $\Delta E > 0$ (at finite temperature).

expression for the rates $\Gamma$ is appropriate for a voltage biased system in which case only elastic tunneling events have to be considered (see Ingold and Nazarov (1992)). In a more general situation of electrical connections with finite—possibly complex—impedance a more elaborated theory is needed which accounts for the exchange of energy between the system and environmental modes during tunneling. For this so called $P(E)$-theory we refer e. g. to Ingold and Nazarov (1992). For the experimental observations presented in this work Eq. 2.1 is sufficient.

Tunneling connects neighboring charge states differing by one electron on a particular island which is transferred to or from an adjacent contact (which can be a reservoir as well as a further island). In many cases only a finite number of charge state have to be considered while all others are energetically too costly to be occupied with a relevant probability. For this finite number of states a master equation can easily be set up which describes the change of occupation probabilities resulting from the rates in Eq. 2.1 (see e. g. Kouwenhoven et. al. (1997)). Finding steady state solutions of the master equation is in general a simple task and allows the calculation of characteristics of the types shown in Fig. 2.3.

### 2.1.2 Higher order electron tunneling

The sequential model is very useful to describe the basic features of single charge transport. In many cases it gives even quantitatively correct results. However, its range of applicability is limited. It is implicitly assumed that the conductance of all tunneling contacts comprising a particular device are small, $G \ll e^2/h$. For real devices with reasonable resistances one finds only partial agreement between experimental results and the prediction of the sequential tunneling model. The most prominent corrections are due to higher order tunneling processes which involve tunneling of more then one electron at the same instant of time. As an example we look at

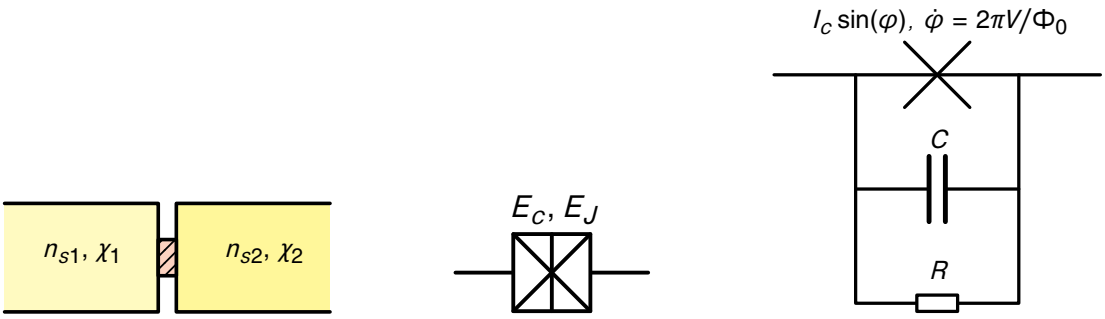


Figure 2.5: Left: Two superconducting electrodes (yellow) coupled via a tunneling contact (red, hashed). Middle: Schematic representation of a real Josephson junction. Right: A real Josephson junction might be represented by an ideal one in parallel with a capacitance and a resistor.

the linear response conductance of a SET as a function of temperature. The sequential tunneling model predicts an exponential suppression at low temperatures: $G \propto \exp(E_c/k_B T)$. This result ignores the possibility that the in-tunneling of an electron can be associated with the out-tunneling of a different electron across the other contact. The sequential transport is blocked by the charging energy (which is the reason for the exponential behavior), while the latter process is energetically favorable at arbitrarily small bias voltage. If co-tunneling processes of this kind are properly taken into account we find (Averin and Likharev, 1992):

$$G \propto g^2 G_0 (k_b T/E_c)^2$$

in accordance with experimental observations. Here $g$ is the serial conductance of both transistor junctions in the voltage biased mode in units of $G_0 = e^2/h$. Thus instead of an exponential we only find an algebraic suppression of the current for $T \to 0$.

The above result for the linear response conductance of the SET is applicable for gate voltages far from the degeneracy points $V_g = (n + 0.5)e/C_g$. At these specific points the low temperature limit of the sequential tunneling model predicts a temperature independent conductance of $G = (g/2)G_0$. In experiments a $\log(k_b T/E_c)$ correction to this simple result is found (Joyez et. al., 1997). An elaborated theoretical treatment is necessary (Schoeller and Schön, 1994; Göppert and Grabert, 2000) to account for this experimental fact as ordinary perturbation theory fails. Nevertheless, today an amazingly good agreement between theory and experiment can be accomplished (Wallisser et. al., 2002) based on Quantum Monte-Carlo calculations applied to the model Hamiltonian introduced in Sec. 2.1.1 without any fitting parameter (all parameters where deduced independently in the experiment). However, this promising result is difficult to carry to more complex situations (Limbach, 2002; Kubala et. al., 2006).

## 2.2 Josephson junction in the strong damping regime

The physics of small metallic tunnel junctions at low temperature gets more complex in case of superconductivity (see e. g. Likharev (1986)). In this work, aluminum with a low $T_c \approx 1\mathrm{K}$ is used, which can be driven normal with a small magnetic field. As predicted by Josephson (1962) and experimentally confirmed shortly afterwards (Anderson and Rowell, 1963) a superconducting tunnel junction can support a sizeable supercurrent. This supercurrent results from the fact that the superconducting condensate of Cooper pairs forms a macroscopic wavefunction $\Psi = \sqrt{n_S}\exp(i\chi)$ the time evolution of which is described by Schrödinger's equation. $|\Psi|^2$ can be interpreted as the density $n_s$ of the condensate. The supercurrent is a $2\pi$-periodic function in the gauge invariant phase difference $\varphi = \Delta\chi - (2\pi/\Phi_0)\int \boldsymbol{A}d\boldsymbol{s}$. Here $\Delta\chi$ is the difference in phase of the condensate wavefunctions in the two electrodes, $\boldsymbol{A}$ is the vector potential associated with the magnetic field, and the integration is from one electrode of the tunneling barrier to the other. Josephson deduced the current-phase relation

$$I_s = I_c \sin(\varphi), \tag{2.2}$$

which is obviously the simplest form of a periodic behavior in $\varphi$ obeying the condition $I_s(\varphi = 0) = 0$. The maximal supercurrent $I_c$ is related to the coupling strength of the two superconducting electrodes. A measure of the latter is given by the normal state conductance of the tunnel junction $G_n = 1/R_n$. A microscopic theory gives for BCS condensates (Bardeen et. al., 1957) the Ambegaokar-Baratoff relation (Ambegaokar and Baratoff, 1963a,b): $I_cR_n = (\pi\Delta(T)/2e)\tanh(\Delta(T)/2k_bT)$ which reduces at low temperatures to

$$I_cR_n = \pi\Delta/2e. \tag{2.3}$$

Thus the $I_cR_n$ product is a material dependent property of a superconducting tunnel junction. In general the observed critical current $I_c$ is somewhat smaller than predicted by Eq. 2.3 (see e. g. Likharev (1986)). The essence of Eq. 2.3 is the proportionality of $I_c$ and $G_n$, which holds despite the fact that the supercurrent results from a second order process in quasiparticle tunneling (at the end it is still electrons not Cooper pairs that tunnel). This nicely proves the coherent nature of the condensate. A supercurrent can flow between two superconductors whenever they are weakly coupled. In some situations the sinusoidal dependence expressed by Eq. 2.2 has to be replaced by $I_s = I_cf(\varphi)$, where $f(\varphi) = f(\varphi + 2\pi)$. Under the obvious condition that at vanishing current (i. e. for a disconnected junction) the phase difference should vanish[4], we get $f(\varphi) = I_s\sin(\varphi) + \sum I_m\sin(m\varphi)$.

Superconducting tunnel junctions embedded in electrical circuits can be found in two distinct states. Either the voltage drop across it vanishes; then the current through the junction

[4] Note that the current through a Josephson junction vanishes at $\varphi = \pi$ as well. In special cases one finds indeed that in a disconnected junction a state with $\varphi = \pi$ is stable. This so called $\pi$-junctions have been reported for weak links with special properties (e. g. Ryazanov et. al. (2000, ferromagnetic links); Cleuziou et. al. (2006, links by carbon nanotubes); Baselmans et. al. (1999, special normal metal links)) or superconductors with order parameters of higher then s-symmetry (e. g. Tsuei and Kirtley (2000); Van Harlingen (1995); Hilgenkamp et. al. (2003)).

is completely characterized by the current-phase relation 2.2. Or one measures a finite voltage drop across the junction, in which case Eq. 2.2 has to be complemented by the so called "phase-voltage relation":

$$\frac{\mathrm{d}\varphi}{\mathrm{d}t} = \frac{2\pi}{\Phi_0} V, \tag{2.4}$$

which states that a finite voltage is associated with a change in the gauge invariant phase difference. The flux quantum $\Phi_0$ is defined as $\Phi_0 = h/2e$. At constant $V = V_{\mathrm{dc}}$ the phase evolves linearly in time resulting in an oscillating behavior of the supercurrent via the current-phase relation. The frequency $f_J$ of this ac-current is related to the dc voltage by the fundamental law $f_J = V_{\mathrm{dc}}/\Phi_0 \approx (483\,\mathrm{MHz}/\mu\mathrm{V})V_{\mathrm{dc}}$.

The current-phase (2.2) and the phase-voltage relation (2.4) together describe what is often called an ideal Josephson junction. Such an idealized version is represented in circuit diagrams by a bare cross (×). In reality further contributions to the current through the junction have to be considered. We represent a real Josephson junction by the symbol depicted in the middle of Fig. 2.5. As indicated we like to think of a real Josephson junction in terms of two competing energy scales, $E_c$ and $E_j$. We have introduced the first one in Sec. 2.1. It is simply related with the junction capacitance, $E_c = e^2/(2C)$, and describes the energy stored in the junction when it is charged up by the charge of a single electron (compared to the uncharged configuration). The second scale $E_j = \Phi_0 I_c/(2\pi)$ equals the energy stored in a Josephson junction if a supercurrent of size $I_c/2$ is driven through it. This can be derived from the two Josephson relations in the following way:

$$E_j = \int_0^{I_c/2} I_s V \mathrm{d}t = \int_0^{I_c/2} I_c \sin(\varphi) \frac{\mathrm{d}\varphi}{\mathrm{d}t} \frac{\Phi_0}{2\pi} \mathrm{d}t = \frac{I_c \Phi_0}{2\pi} \int_0^{\pi/2} \sin(\varphi) \mathrm{d}\varphi = \frac{I_c \Phi_0}{2\pi}.$$

According to quantum mechanics the measurable quantities $\varphi$ and $n$ (the charge on the junction in units of $e$) are associated with Hermitian operators $\hat{\varphi}$ and $\hat{n}$, respectively. It can be shown that they obey the commutation rule

$$[\hat{\varphi}, \hat{n}] = 2i. \tag{2.5}$$

This rule expresses the indeterminacy relation for Cooper pairs

$$\Delta\varphi \Delta N \geq 1.$$

The phase $\varphi$ can only be fixed if the number of Cooper pairs is allowed to fluctuate and vice versa. Josephson junctions with $E_j \gg E_c$ favor states with a fixed phase difference, while junctions with $E_j \ll E_c$ are dominated by charging effects which by definition try to hold the charge constant.[5]

The real Josephson junction can be thought of as a parallel combination of several ideal elements as indicated in the right panel of the same figure. First of all we have the ideal Josephson

[5] The arguments in this paragraph are a bit sloppy. A proper analysis has to take into account the environment into which the Josephson junction is embedded (see below). As in the normal-conducting case charging effects are readily observable in multi island arrangement only. In Sec. 2.3 the superconducting transistor is going to serve as an example.

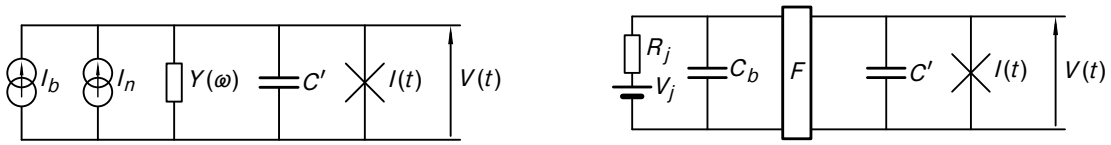


Figure 2.6: Representation of a Josephson junction in a typical experimental environment. See text for details

element and the capacitance associated with $E_c$. It is clear that in the general situation when neither the voltage across nor the current through the junction vanishes dissipation takes place. In the RCSJ (resistively and capacitively shunted junction) model the dissipation is modeled by a resistance. Close to $T = T_c$ dissipation is mainly due to thermally exited quasiparticles and $R \approx R_n$ might be a reasonable choice. At low temperature thermally excited quasiparticles die out. A proper RCSJ model takes this into account by adapting a strongly nonlinear resistance $R(V)$. At $V > 2\Delta/e$ the applied voltage can break up Cooper pairs and $R$ can be approximated by a value close to $R_n$ again. At $V < 2\Delta/e$ no quasiparticle can be generated and $R$ might eventually be ignored completely (which amounts to $R \to \infty$).

In this work we are concerned with Josephson junctions at very low temperatures $T \ll T_c$, so essentially no quasiparticles are present at small bias. We partially follow the arguments given in Joyez (1995, Chap. IV). Suppose we connect a real Josephson junction at low temperature in a typical experimental set-up to a current source $\mathcal{I}$ and a voltmeter. We omit the resistive part in the RCSJ model and view the junction as an ideal Josephson element in parallel with a capacitance $C$. Source, meter and connections (as described in Chap. 4) represent together with the capacity $C$ a linear network of circuit elements which acts on the ideal Josephson element like Norton's equivalent, i. e. as a current source $I_b$ in parallel with an admittance $y(\omega)$. It turns out to be convenient to split up $y(\omega)$ in a capacitance $C' = \lim_{\omega\to\infty}(y(\omega)/i\omega)$ and $Y(\omega) = y(\omega) - iC'\omega$. The capacitance $C'$ is the sum of the junction capacitance $C$ and contributions by the leads. The latter are for small tunnel junction in most cases the dominating part as discussed in Sec. 2.1. We thus arrive at the equivalent circuit schematically drawn in Fig. 2.6. The current $I_n(t)$ models the Johnson-Nyquist noise of the admittance seen by the Josephson element (i. e. its properties are determined by the spectral density $S_{I_n}(\omega) = 4k_bT\mathrm{Re}(Y(\omega))$). Some interesting and general properties of biased Josephson junction follow directly from the equivalent circuit diagram of Fig. 2.6 (see Joyez (1995)). However, to make a useful connection with our experimental set-up a closer look on the wiring is helpful. It is well known that thermalization of mesoscopic devices at dilution fridge temperatures requires careful filtering. Even if the lattice of solid state devices is equilibrated with the surrounding bath at about $T \sim 20\,\mathrm{mK}$ the electronic system might be at considerable higher temperatures due to radiation coming through electric connections. The thermal noise of the room temperature parts of the set-up cause a tremendous load which is in practice hard to sink. Even the black body radiation from the 4 Kelvin stage of the set-up provides photons with energies exceeding the typical charging energies. This leads to out-of-equilibrium photo assisted processes which tend to wash out the Coulomb blockade. In the superconducting state quasiparticles can reach sensitive

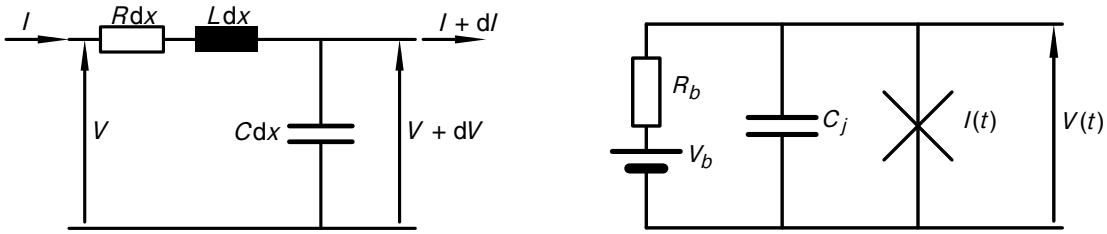


Figure 2.7: Left: An infinitesimal slab of a lossy transmission line. Right: Simple biasing scheme of a junction.

parts of the circuitry at a rate which makes a full equilibration impossible. While in small volumes and at low temperature the number of equilibrium quasiparticles would vanish, these out-of-equilibrium excitations void certain predictions and the electronic temperature seems to saturate at quite high values of typically a few hundreds of millikelvin.

For these reasons efficient filtering of the leads is needed. Simple estimates yield a quality of filtering of 200 dB for frequencies above 20 GHz. The right panel of Fig. 2.6 displays the typical experimental situation. A source $V_b$ with large but finite impedance $R_b$ is connected to a filter stage $F$. The capacitance $C_b$ together with $R_b$ limits the bandwidth of the room temperature side of the set-up. Note that thermal noise can drastically be reduced by putting the resistor $R_b$ at low temperatures. The filter is in essence a lossy transmission line built to lead to almost complete damping of frequencies above a few hundred MHz. The physics of lossy transmission lines is captured by the model pictured in Fig. 2.7 where a infinitesimal slab of the line is characterized by a resistance, an inductance and a capacitance per unit length. In most practical cases the resistance per unit length scales as $\sqrt{\omega}$ at high frequencies due to the skin effect which confines the region of finite current density to the surface layers of the transmission line which gets thinner with frequency. The model leads easily to the so called telegraph equation

$$\frac{\mathrm{d}^2V}{\mathrm{d}x^2} = i\omega C(R + i\omega L)V \tag{2.6}$$

for the voltage along the line which has solutions of the form

$$V(x) = V_1 \exp(\gamma x) + V_2 \exp(-\gamma x). \tag{2.7}$$

Here $\gamma = \sqrt{C(R + i\omega L)} = \omega\sqrt{LC/2}(\sqrt{a-1} + i\sqrt{a+1})$ and $a = \sqrt{(R/\omega L)^2 + 1}$. A transmission line of finite length $\ell$ biased with the voltage $U_0 = V_0 \exp(i\omega t)$ has a Norton's equivalent with a current source and an impedance given by

$$I = \frac{2U_0}{Z_0(l - 1/l)}, \tag{2.8}$$

$$Z = \frac{Z_0(l - 1/l)}{(l + 1/l)}, \tag{2.9}$$

respectively, where $Z_0 = \sqrt{L/2C}(\sqrt{a+1} - i\sqrt{a-1})$, and $l = exp(\gamma\ell)$.

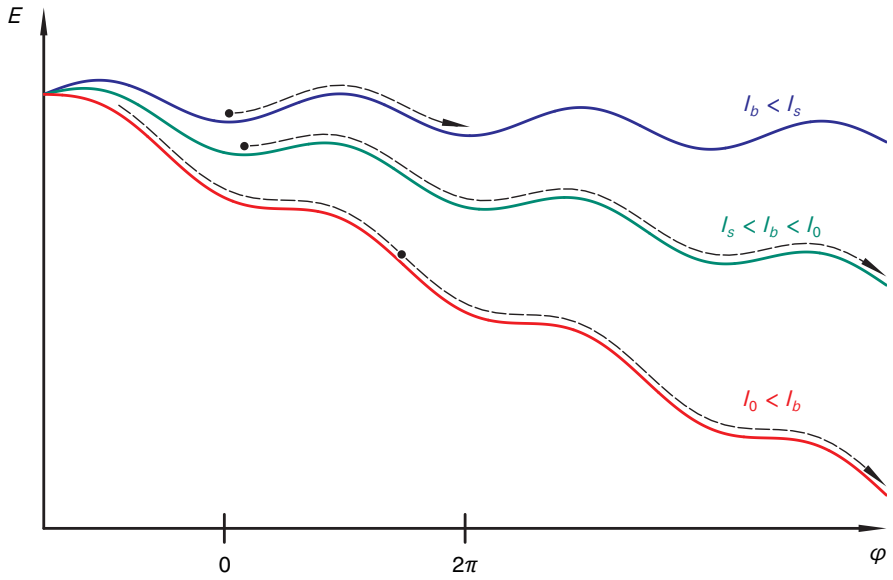


Figure 2.8: Tilted washboard model: The dynamics of the gauge invariant phase difference $\varphi$ is equivalent to that of a particle in a tilted sinusoidal potential. The tilt corresponds to the bias current $I_b$. A frictional force results from the admittance $Y(\omega)$ of the environment. $\boldsymbol{I_b < I_s}$: At small bias $\varphi$ is mostly captured in a local minimum of the potential. Thermal fluctuations, however, lead to a diffusive motion between different minima with a preferred direction due to the energy gain between successive minima. On average a finite current results. $\boldsymbol{I_s < I_b < I_o}$: Above a certain threshold the energy gain between successive minima is larger than the energy loss due to dissipation. Thus, $\varphi$ is in a running state once it escaped a local minimum by thermal activation. $\boldsymbol{I_o < I_b}$: Above the critical current $I_0$ the tilt destroys the local minima altogether and no static solution for $\varphi$ exists.

The sole purpose of the filter is to suppress the transmission of noise at high frequencies. The damping of the transmission line in Neper per unit length at high frequencies is given by the real part of $\gamma$ as apparent by inspection of Eq. 2.7: $\lim_{\omega \gg (R/L)} \Re(\gamma) = (R(\omega)/2)\sqrt{C/L}$. The Norton impedance in the limit of high damping and high frequency is given by $\lim_{\omega \gg (R/L)} Z = \sqrt{L/C}$. In the limit of small frequencies we get $\lim_{\omega \ll (R/L)} Z = R\ell$, i. e. the DC resistance of the filter $R_f$.

From this concise description of the filter's properties the following general picture can be deduced: The filtered set-up facilitates the DC biasing of the Josephson junction with a current source $I_b = V_b/(R_b + R_f)$ (the Norton equivalent impedance is obviously $R_b + R_f$). In practice $R_f$ is of the order of a few ohms and $R_f \ll R_b$ holds. At high frequencies however, the Josephson junction is practically connected to an ohmic impedance $R_j$. While the exact value of $R_j$ depends on the details of the filters, the expression $R_j = \sqrt{L/C}$ deduced for the simple model—$\sqrt{L/C}$ is the wave-impedance of the transmission line—shows that a value of the order of the vacuum impedance $Z_0 = \mu_0 c \sim 120\pi\Omega$ can be expected. For frequencies

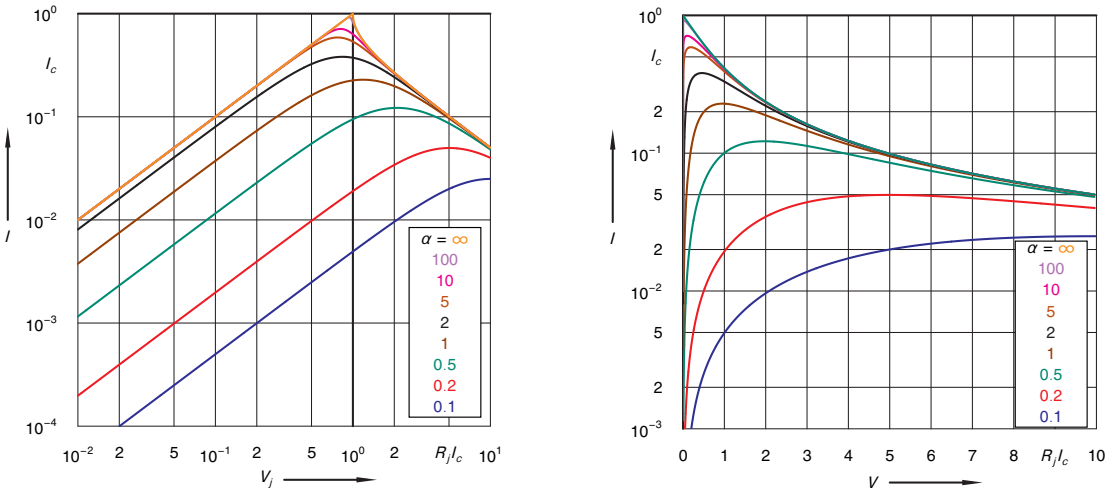


Figure 2.9: I-V characteristics of an over-damped Josephson junction as predicted by Eq. 2.11. Left: Current as a function of bias $V_j$. Right: Current as a function of $V = V_j - IR_j$.

above a threshold $\omega_c$ (for our simple model we got $\omega_c = R/L$) the filters efficiently decouple the circuitries connected at both sides. The dynamics of the Josephson phase involve processes at the plasma frequency $\omega_p = \sqrt{2\pi I_0/(\Phi_0 C)}$. In practice $\omega_c \ll \omega_p$ and on the bias side of the filters time averaged values of $I(t)$ and $V(t)$ are operative only. In the same way any noise contribution present at the room temperature side of the filters with frequency $\omega \gg \omega_c$ cannot reach the Josephson element (this is the intended purpose of the filters). When setting up a differential equation describing the dynamics of $I(t)$ and $V(t)$, we can treat the voltage at the input of the filters (i. e. the voltage at the bias side of $F$ in Fig. 2.6) as quasi-static. If we want to describe the influence of thermal noise, the only relevant contribution comes from $R_j$, i. e. the Norton equivalent resistance of the filters at high frequencies. This virtual resistance is equilibrated at the temperature of the junction, again a feature of filters worth mentioning. Finally we arrive at the fairly simple biasing scheme on the right side of Fig. 2.7. In the figure $V_j = I_b/R_j$ and $R_j$ is noisy with a white noise characteristic of $\langle V_n(t)V_n(t+\tau)\rangle = 2k_bTR\delta(\tau)$. The fluctuation $V_n(t)$ add to the bias $V_j$. The following differential equation can be readily obtained (e. g. Tinkham (1996)):

$$\frac{\mathrm{d}^2\varphi}{\mathrm{d}\tau^2} + \frac{1}{\sqrt{\beta_c}}\frac{\mathrm{d}\varphi}{\mathrm{d}\tau} + \sin(\varphi) = I/I_0, \tag{2.10}$$

where $I = I_b + I_n(t)$, $I_n(t) = V_n(t)/R$, and $\beta_c = (\omega_p RC)^2$ is a parameter first introduced by Steward and McCumber (Stewart, 1968; McCumber, 1968). Time in Eq. 2.10 is measured in units of $\omega_p^{-1}$: $\tau = \omega_p t$. The dynamics of $\varphi$ is thus identical to the dynamics of a particle in a tilted sinusoidal potential (see Fig. 2.8) damped by a viscous force. In the large friction limit (i. e. when $\beta_c$ happens to be small) the first term in Eq. 2.10 can be omitted and we arrive at a first order differential equation (with a stochastic term $I_n(T)$) which can be treated analytically

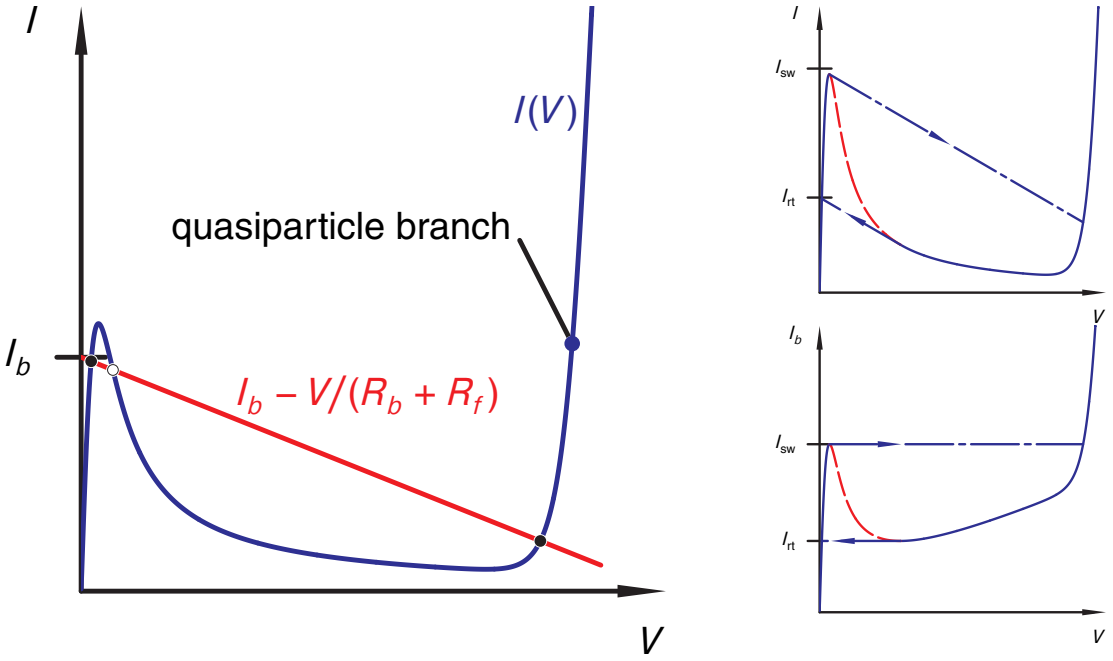


Figure 2.10: I-V characteristics of an over-damped Josephson junction externally biased by a load line with $I_b - V/(R_b + R_f)$. Left: For certain values of $I_b = V_b/(R_b + R_f)$ three solutions of $I(V) = (V_b - V)/(R_b - R_f)$ can be found. Two solutions are stable (•), one is unstable (∘). If $I_b$ is slowly increased starting from $I_b = 0$. The system follows the so called "phase diffusion branch" which is a reminiscence of the supercurrent branch of the under-damped junction. Right: At $I_{sw}$—defined by the local maximum of $I(V)$, the system switches to the second stable solution. Depending on the slope of the load line this solution is at the onset of the quasiparticle branch at $V \approx 2\Delta/e$. On going back in $I_b$ the system retraps at $I_{rt}$ defined by the local minimum of $I(V)$. The lower panel displays the resulting $I_b/V$ characteristic. This corresponds more closely to the characteristic measured in a real experiment.

(Ivanchenko and Zilberman, 1968; Ambegaokar and Halperin, 1969). In this case the mean current $I = \langle I(t) \rangle$ is a single valued function of the bias voltage $V_j$:

$$\frac{I(V_j, T)}{I_0} = \Im \left( \frac{I_{1-i\alpha v}(\alpha)}{I_{-i\alpha v}(\alpha)} \right), \tag{2.11}$$

where $\alpha = E_j/(k_b T)$, $v = V_j/(R_j I_0)$, and $I_\lambda(z)$ is the modified Bessel function of complex order. From $I(V_j, T)$ we get the $I(V)$ dependence by the substitution $V = V_j - R_j I$ (see Fig. 2.9), where $V$ equals the mean voltage across the junction $V = \langle V(t) \rangle$. Thus in the strong damping limit we get a one-to-one correspondence between the time averaged current $I$ through the junction and the time averaged voltage $V$ over the junction. Fig. 2.9 displays the non-monotonic behavior of $I(V)$ at finite temperature. This characteristic is operative at the room temperature side of the filter. If the external bias $V_b(t)$ is a slowly varying function on the

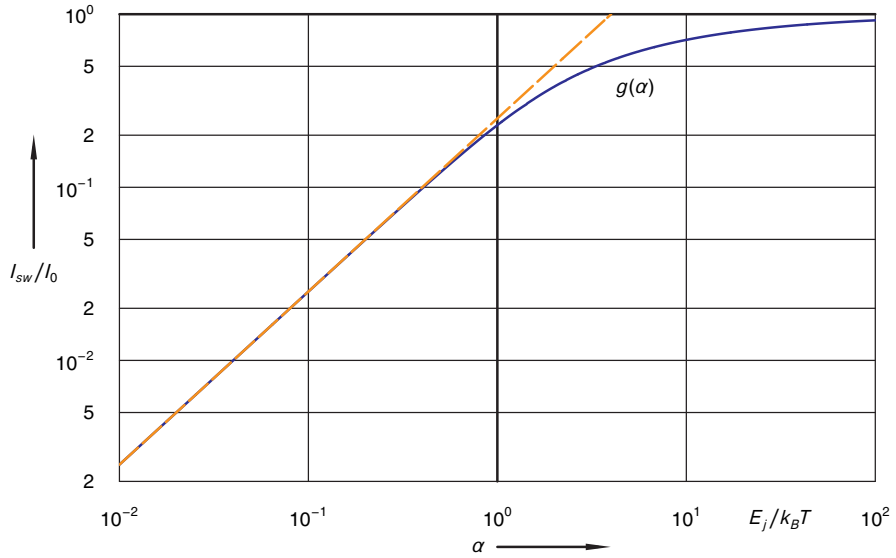


Figure 2.11: Function $g(\alpha)$ describes the ratio between the maximum switching current $I_s$ and the critical current $I_0$ in the over-damped regime. The blue curve shows the numerical results for $g(\alpha)$. For high temperatures $g(\alpha)$ asymptotically converge to $I_s = I_0/4$ (orange curve).

time scale set by $R_bC_b$ we have

$$I(V) = \frac{V_b - V}{R_b + R_f}, \tag{2.12}$$

which implicitly defines $V$. The situation is sketched in Fig. 2.10. The ratio between the maximum current $I_s$ and the critical current $I_0$, depending on $\alpha$, can be written as

$$I_s = I_0 g(\alpha), \tag{2.13}$$

see Fig. 2.11.

## 2.3 Single Cooper-pair transistor (CPT)

The Cooper-pair transistor (CPT), also referred to as single Cooper-pair transistor or superconducting single-electron transistor, is the superconducting version of the single electron transistor which is already described in section 2.1. It consists of two Josephson junctions in series, with a gate electrode coupled through the gate capacitance $C_g$ to the island between the two junctions, see Fig. 2.12. The superconducting island connects to both leads through Josephson junctions. The rich behavior of superconducting tunnel junctions as compared to the normal conducting counterpart leads to an intriguing set of transport phenomena obseverd in CPT. As for the SET, the electrostatic potential of the island can be tuned by the voltage $V_g$ applied to the gate electrode, causing a periodic dependence of the I-V curve on the dimensionless gate-induced charge $n_g = C_gV_g/e$.

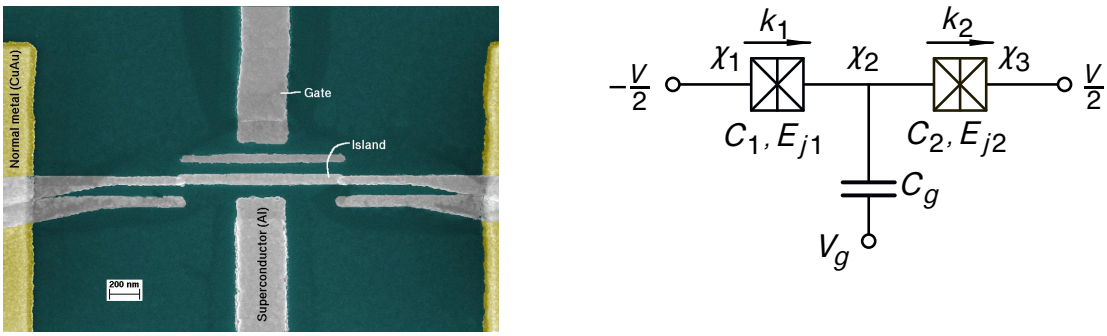


Figure 2.12: The single Cooper pair transistor is the superconducting version of a single electron box, see fig. 2.1. If no magnetic field is applied, the electrodes are superconducting and the transistor behaves as a single Cooper pair transistor. Left: Scanning electron microscope (SEM) photo of a single Cooper pair transistor. The tunneling contacts can be seen as Josephson junctions between the island and the leads. Right: Schematic representation of a voltage biased single Cooper pair transistor. The boxes represent Josephson contacts characterized by a capacitance $C_{1,2}$ and a Josephson coupling energy $E_{j1,2}$. The gate can be seen as a capacitance of size $C_g$ coupled to the island. The phase of the superconducting order parameter on the leads and the island are given by $\chi_1$, $\chi_3$, and $\chi_2$. The number of Cooper pairs which have tunneled from left to right through the junctions is given by $k_1$ and $k_2$.

The CPT has been investigated extensively in the low impedance environment. Both the supercurrent branch (e.g. Geerligs et. al., 1990; Joyez, 1995; Tuominen et. al., 1992; Amar et. al., 1994; Aumentado et. al., 2004) and the finite voltage bias features of the IV curves (e.g. Fulton and Dolan, 1987; Fulton et. al., 1989; Joyez, 1995; Nakamura et. al., 1996, 1997; Haviland et. al., 1994; Fitzgerald et. al., 1998) have been intensively studied. If $E_j/E_c$ is not too low, a finite supercurrent at zero bias voltage can be observed and the CPT behaves in many respects identical to a single Josephson junction with a Josephson coupling tunable with gate voltage. The experiments performed in this regime were mostly studying the modulation of the supercurrent flowing through the CPT with the gate-induced charge. Since the supercurrent is carried by the condensate formed by Cooper pairs, the modulation is expected to be $2e$ periodic in $V_g C_g$. At finite bias voltages $0 < |eV| < 4\Delta$, where charge transport is in principle blocked, rich structure of finite current can be observed. These features can be attributed to various transport mechanisms of coherent and pair-breaking nature and whether certain features can be observed depends again crucially on the $E_j/E_c$ ratio.

We start off this section by giving an outline of physical mechanisms underlying the multiple sub-gap features with a detailed discussion of the most prominent ones. The second half of the section is devoted to the discussion of the supercurrent branch.

### 2.3.1 Sub-gap current positions

In this section, the basic mechanisms of charge transport in the finite voltage bias regime are discussed. Our calculation aims at demonstrating the principles for the generation of current features in the $V/V_g$-plane. We focus on what determines the positions of these features. We are not trying to calculate the size of the current which would be a difficult task beyond the limit of this experimental work.

The relavent circuit considered is shown in Fig. 2.12. In comparison to Fig. 2.1, we have—due to superconductivity—two further energy scales $E_{j1}$ and $E_{j2}$, the Josephson couplings of the two junctions, which take the role of the resistances $R_1$ and $R_2$. The superconducting leads and island are characterized by the macroscopic wave function of the superconducting condensate as indicated by the gauge-invariant phases $\chi_1$, $\chi_2$, and $\chi_3$. Further important parameters are the charge transferred across the junctions which we measure in units of Cooper pairs $2e$, $k_1$ and $k_2$. It is worthwhile noting that the phase $\chi_2$ and the number of Cooper pairs $k$ on the island form a set of quantum mechanically conjugated operators (see Eq. 2.5),

$$[\hat{\chi}_2, \hat{k}] = i. \tag{2.14}$$

As the number of Cooper pairs on the island tends to be fixed, the preferred basis for the states of the system are $\chi_1$, $\chi_3$, and $k$. The Hamiltonian of the system depicted in Fig. 2.12 is given by

$$H = H_{el} + H_T = E_c(\hat{n} - n_0)^2 - eV(k_1 + k_2) + E_j \cos(\hat{\chi}_2)\cos\delta/2. \tag{2.15}$$

The first two terms on the right hand side are related to the electrostatic energy derived in App. A (Eq. A.7),

$$E_{\mathrm{el}} = E_c(n - n_0)^2 - eV(k_1 + k_2).$$

By $n$ we count the number of excess electrons on the island. The last term describes the Josephson coupling and we silently assume $E_{j1} = E_{j2} = E_j$. It couples states of the same parity—odd or even—only. For the sake of simplicity, the bias voltage $V$ is considered to be positive.

Here we are mainly concerned with the electrostatic part of the Hamiltonian. The state of the CPT is characterized by three numbers: $n$, $k_1$ and $k_2$. The state of the CPT will change in case electrostatic energy is gained from the corresponding tunneling processes, $E_{\mathrm{el}}(n+\Delta n, k_1, k_2) - E_{\mathrm{el}}(n, 0, 0) + n_{\mathrm{qp}}\Delta < 0$. With a little algebra, we get the following condition for the bias voltage

$$V \geq \frac{2E_c\Delta n}{e(k_1 + k_2)}(n_{\mathrm{in}} - n_0) + \frac{E_c\Delta n^2 + n_{\mathrm{qp}}\Delta}{e(k_1 + k_2)}. \tag{2.16}$$

Here $n_{\mathrm{in}}$ labels the state at which the process starts and $\Delta n = n_{\mathrm{fi}} - n_{\mathrm{in}}$ is the number change of excess electrons. We also included the possibility that a pair of quasiparticles is created which costs twice the gap energy $2\Delta$, in which case $n_{\mathrm{qp}} = 2$ in the above inequality (otherwise $n_{\mathrm{qp}} = 0$). In the above formula, $|n_0| < 1$. Other values of $n_0$ can be treated by shifting $n_0$ as well as $n_{\mathrm{in}}$ by an appropriate even integer: $n_0 \to n_0' = n_0 + 2m$, $n_{\mathrm{in}} \to n_{\mathrm{in}}' = n_{\mathrm{in}} + 2m$. This leaves the right hand side of Eq. 2.16 unchanged.

The equality in Eq. 2.16 defines straight lines in the $V/n_0$-plane of the form

$$\frac{eV(n_0)}{4E_c} = n_0 a + b + \frac{\Delta}{4E_c} c, \tag{2.17}$$

where $a = -(\Delta n/2)/(k_1 + k_2)$, $b = ((\Delta n^2 + 2n_{\mathrm{in}}\Delta n)/4)/(k_1 + k_2)$ and $c = n_{\mathrm{qp}}/(k_1 + k_2)$. Eq. 2.16 describes whether a process characterized by $\Delta n$, $n_{\mathrm{qp}}$, and $k_1$ ($k_2 = k_1 - \Delta n/2$) is energetically favorable. If so,the state is unstable and the island changes its charge by $\Delta n$ after a certain time. If $\Delta n = 0$, this is directly related to some finite current. For $\Delta n \neq 0$, current will not necessarily result, as the new charge state might be stable. However, a series of further favorable processes with different $\Delta n$ might bring the island back to the original charge state and lead to a cyclic path around a number of states. This cyclic process is then related to finite current. Several of this type of processes have been identified and got specific names in literature.

In the following sections, we are describing current cycles we observed from our experiments which will be discussed in Chap. 5.2. We start up with processes at higher bias and approach features close to zero bias step by step.

#### 2.3.1.1 Quasiparticle transport (QPT)

For $V > 4\Delta/e$, transport is dominated by single electron transport. Single electrons have to be created by exciting quasiparticles from the quantum condensate. In the language in the last section (see Eq. 2.17), one possible cycle comprises two steps:

| Step | $n_{\mathrm{qp}}$ | $n_{\mathrm{in}}$ | $\Delta n$ | $2k_1$ | $2k_2$ | $a$ | $b$ | $c$ |
|---|---|---|---|---|---|---|---|---|
| 1 | 2 | 0 | 1 | 1 | 0 | -1 | $1/2$ | 4 |
| 2 | 2 | 1 | -1 | 0 | 1 | 1 | $-1/2$ | 4 |

The first step describes the generation and tunneling of a quasiparticle across the left junction, the second one the generation and tunneling of a quasiparticle across the left junction. The lines described by the slope $a$ and the intercept $b+(\Delta/4E_c)c$ define together a lower boundary for the onset of this process. However the above considerations are imcomplete and give the correct boundary only in the range $0 < n_0 < 1$. Another similar process which starts at $n_{\mathrm{in}} = -1$ gives another pair of straight lines of lower voltage for $-1 < n_0 < 0$. Combining this two processes and unfolding the combination to the extended picture $-\infty < n_0 < \infty$ defines a zigzag line above which the current cycle runs. The zigzag line is depicted in Fig. 2.13 as thick red line.

#### 2.3.1.2 Josephson quasiparticle cycle (JQP)

For $V < 4\Delta/e$, current can only be carried by more complex cycles, where one process at least involves coherent Cooper pair tunneling. The most prominent example is the so-called Josephson quasiparticle cycle, first described by Fulton et. al. (1989). One possible cycle of this type is given in the following table.

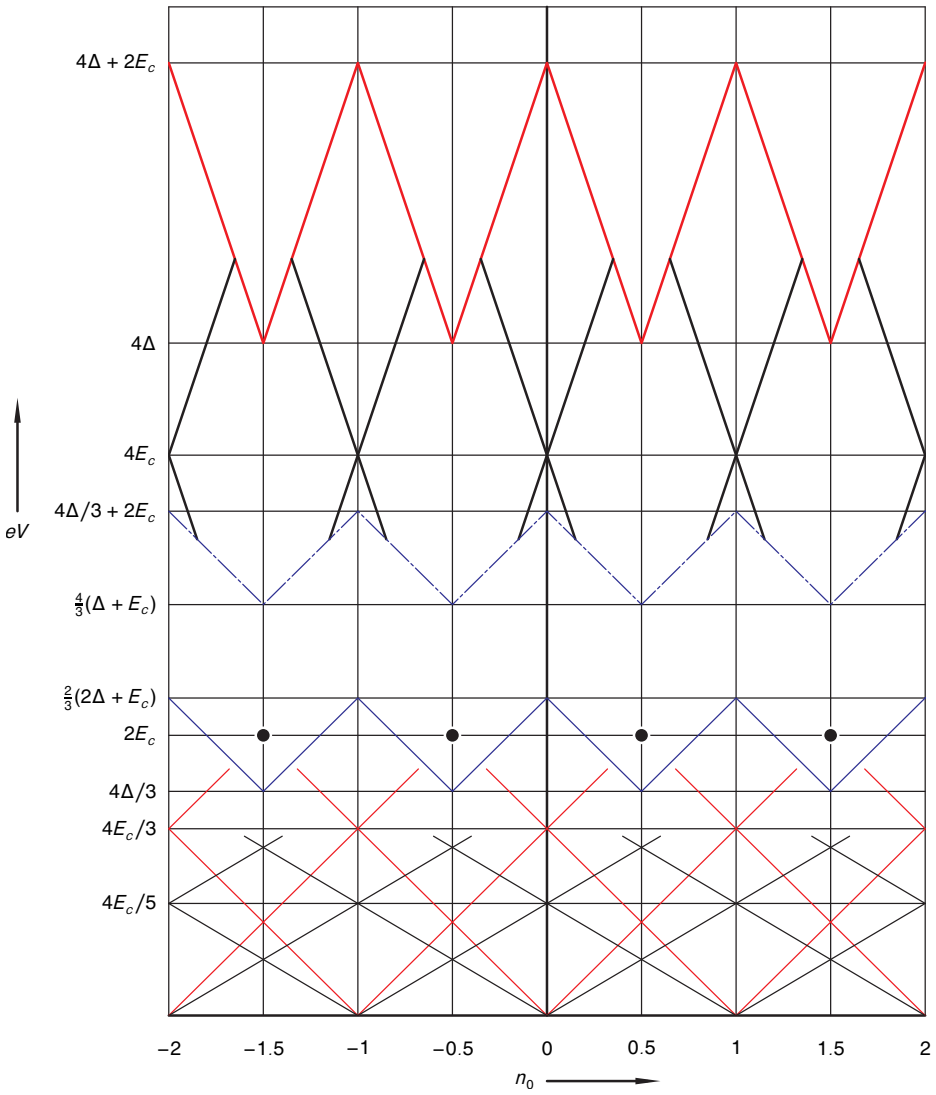


Figure 2.13: Most prominent current features of a CPT with $\Delta = 1.2E_c$ in the $V/n_0$-plane. From large biases $V$ to small biases, we have:

- Onset of quasiparticle tunneling (thick red line)
- Josephson quasiparticle cycle (thick black lines)
- Onset of a higher-order 3e-cycle identified in our experiments (dash-dotted blue line). See Chap. 5 for discussion.
- Double Josephson quasiparticle cycle (Black dots)
- Onset of 3e-cycle (blue line)
- Third order resonant Cooper pair cycle (thin red lines)
- Fifth order resonant Cooper pair cycle (thin blue lines)

| Step | $n_{\mathrm{qp}}$ | $n_{\mathrm{in}}$ | $\Delta n$ | $2k_1$ | $2k_2$ | $a$ | $b$ | $c$ |
|---|---|---|---|---|---|---|---|---|
| 1 | 0 | 0 | 2 | 2 | 0 | -1 | 1 | 0 |
| 2 | 2 | 2 | -1 | 0 | 1 | 1 | $-3/2$ | 4 |
| 3 | 2 | 1 | -1 | 0 | 1 | 1 | $-1/2$ | 4 |

The first step describes the coherent coupling of two Cooper pair states with zero and one extra Cooper pair on the island. This coupling is efficient only close to zero energy change and the inequality 2.16 becomes an equality. The straight line it describes represents a resonance rather than an onset of current as in the previous section. The second step of the cycle describes the decay of the state with one extra Cooper pair to a state with only one quasiparticle on the island. This requires the generation and tunneling of of one quasiparticle across the right junction, and the third step closes the cycle by generating and tunneling out of a further quasiparticle. The last step limits the bias range at which the cycle runs efficiently. The bias range at which the pronounced JQP current happens is $2\Delta + E_c < V < 2\Delta + 3E_c$[6]. JQP is shown as thick black lines in Fig. 2.13.

Aleshkin and Averin (1990) and Averin and Aleshkin (1989) have treated the current due to the JQP cycle quantitatively. Under the assumptions $E_j \ll E_c$ and $g_N \ll 1$, where $g_N$ is the normal state conductance of an individual contact in units of $G_0$, they derived

$$\gamma = \frac{\Gamma_{qp} E_j^2}{4\delta^2 + (\hbar\Gamma_{qp})^2}, \tag{2.18}$$

for the tunneling rate $\gamma$ of Cooper pairs. Here $\Gamma_{qp} \simeq g_N(eV + E_c)/h$ is the rate of the first quasi-particle tunneling and $\delta = 4E_c(1 - n_0) - eV$ is the energy distance from the resonance. For a JQP cycle to happen, this energy difference $\delta$ should be close to 0 for an effective mixing of the two Cooper pair states.

This approach has been used by Nakamura et. al. (1996) and Pohlen et. al. (2000) in a comparison to experimental data and good quantitative agreement has been found. In the validity range of Eq. 2.18, the JQP cycle is bottlenecked by the Cooper pair tunneling process and gives a peak current $I \sim 2eE_j^2/\hbar^2\Gamma_{qp}$ with the peak width $\Delta I \sim \hbar\Gamma_{qp}$.

In many cases, the crossing point of two JQP lines which happens at $eV = 4E_c$ can be used to determine the charing energy $E_c$. We use this method whenever we do not resolve Cooper pair resonances at lower biases (see Sec. 2.3.1.5).

#### 2.3.1.3 Double Josephson quasiparticle cycle (DJQP)

A slightly more complicated current cycle in comparison with the JQP is known as the double Josephson quasiparticle cycle. It comprises the following four steps:

[6] The upper boundary is set by quasiparticle processes interrupting the cycle.

| Step | $n_{qp}$ | $n_{in}$ | $\Delta n$ | $2k_1$ | $2k_2$ | $a$ | $b$ | $c$ |
|---|---|---|---|---|---|---|---|---|
| 1 | 0 | 0 | 2 | 2 | 0 | -1 | 1 | 0 |
| 2 | 2 | 2 | -1 | 0 | 1 | 1 | $-3/2$ | 4 |
| 3 | 0 | 1 | -2 | 0 | 2 | 1 | 0 | 0 |
| 4 | 2 | -1 | 1 | 1 | 0 | -1 | $-1/2$ | 4 |

Similarly to the JQP, a resonant Cooper pair tunneling step is followed by a quasiparticle event. Then a further resonant Cooper pair process happens. The states coupled coherently by step one and three differ in parity. The cycle is completed by a further quasiparticle process. Because two resonant conditions have to be fulfilled, the DJQP happens at singular points in the $V/n_0$-plane, shown as black dots in Fig. 2.13.

#### 2.3.1.4 3e cycle

All the processes we discussed so far are characterized by the same slope in the $V/n_0$-plane. Processes which involved simultaneous tunneling of charges at both contacts can give a different slope, which is clear from inspection of Eq. 2.16. Often reported is the so-called 3e cycle, which in our language can be formulated as follows:

| Step | $n_{qp}$ | $n_{in}$ | $\Delta n$ | $2k_1$ | $2k_2$ | $a$ | $b$ | $c$ |
|---|---|---|---|---|---|---|---|---|
| 1 | 2 | 0 | 1 | 2 | 1 | $-1/3$ | $1/6$ | $4/3$ |
| 2 | 2 | 1 | -1 | 1 | 2 | $1/3$ | $-1/6$ | $4/3$ |

The first step represents a simultaneous tunneling of a Cooper pair on the left junction and a quasiparticle on the right junction. The second step then brings the island back to the original charge state by simultaneously tunneling of a Cooper pair on the right junction and a quasiparticle on the left junction. Like the quasiparticle tunneling, the straight lines defined by the table border a region above which finite current results. This onset is marked by a solid blue line in Fig. 2.13.

#### 2.3.1.5 Resonant Cooper pair tunneling (RCPT)

Further sub-gap resonances have been observed by several authors at voltage biases approaching zero (Haviland et. al., 1994; Joyez, 1995; Billangeon et. al., 2007). Joyez argued that the resonant coupling between adjacent Cooper pair states can lead to current when it is interrupted by an incoherent Cooper pair process. The resonant conditions of different order are described in the following table.

| Order | $n_{qp}$ | $n_{in}$ | $\Delta n$ | $2k_1$ | $2k_2$ | $a$ | $b$ | $c$ |
|---|---|---|---|---|---|---|---|---|
| $3^{rd}$ | 0 | 0 | 2 | 4 | 2 | $-1/3$ | $1/3$ | 0 |
| $5^{th}$ | 0 | 0 | 2 | 6 | 4 | $-1/5$ | $1/5$ | 0 |
| $n^{th}$ | 0 | 0 | 2 | $n+1$ | $n-1$ | $-1/n$ | $1/n$ | 0 |

Third and fifth order are shown in thin red and black lines in Fig. 2.13. In Chap. 5, we present experiments which show resonances following these lines. However, these lines do not start at zero bias but at the first crossing. We postpone the discussion to Chap. 5.

The crossing points of the resonant lines can be used for a determination of the charging energy of the transistor Haviland et. al. (1994); Joyez (1995). In particular, the crossing of the resonances of the third order is extensively used in this work for evaluating the charging energy $E_c$. The crossing of the third order resonant Cooper tunneling lines appears at [7]

$$eV \simeq \frac{4E_c}{3}. \tag{2.20}$$

This method does require relatively large $E_j/E_c$ ratios. Only then resonance lines can be resoluted. In other cases, the crossing of the two JQP lines serves as a good alternative, as mentioned in Sec. 2.3.1.2.

### 2.3.2 The critical and switching current of the CPT

At zero bias, the Hamiltonian 2.15 simplifies to

$$H = E_c(\hat{n} - n_0)^2 - E_j \cos(\delta/2) \cos \hat{\chi}_2.$$

This Hamiltonian can easily be diagonalize in a subspace of charge states and used to find the corresponding energy levels $E_m(\delta, n_0)$, where $m$ is a band index. Figure 2.3.2 shows two lowest energy bands $m = 0, 1$ for symmetric and asymmetric CPTs with different $E_j/E_c$ ratios. The bands are $2e$ periodic in the gate charge and $2\pi$ periodic in the phase $\delta$.

The CPT can be viewed as a single Josephson junction with a coupling energy tunable by a gate voltage. At fixed gate voltage, the function $E_0(\delta, n_0)$ has maxima at $\delta = (2n + 1)\pi$ and minima at $\delta = 2n\pi$. We define $E_0(n_0)$ by

$$E_0(n_0) = \frac{E_0(\pi, n_0) - E_0(0, n_0)}{2}. \tag{2.21}$$

Then

$$f_0(\delta, n_0) = \frac{E_0(\delta, n_0)}{E_0(n_0)} \tag{2.22}$$

is a periodic function in $\delta$ (for fixed $n_0$) with amplitude 2.

The critical current is a function of $n_0$ and given by[8]

$$I_s n_0 = \frac{2\pi}{\Phi_0} \max_{\delta} \left( \frac{\partial E_0(\delta, n_0)}{\partial \delta} \right). \tag{2.23}$$

[7] Joyez (1995) pointed out that a more exact perturbative calculation yields

$$eV \simeq \frac{4E_c}{3} + \frac{3E_j^2}{32E_c}. \tag{2.19}$$

The correction term in the above equation can be neglected in our parameter range.

[8] As explained in the discussion of a single junction in Sec. 2.2, the dynamics of the phase $\phi$ is identical to the dynamics of a mechanical particle in a sinusoidal potential. The bias current corresponds to a tilt of the potential. In the present case, the whole landscape $E_0(\delta, n_0)$ is tilted along the $\delta$ axis.

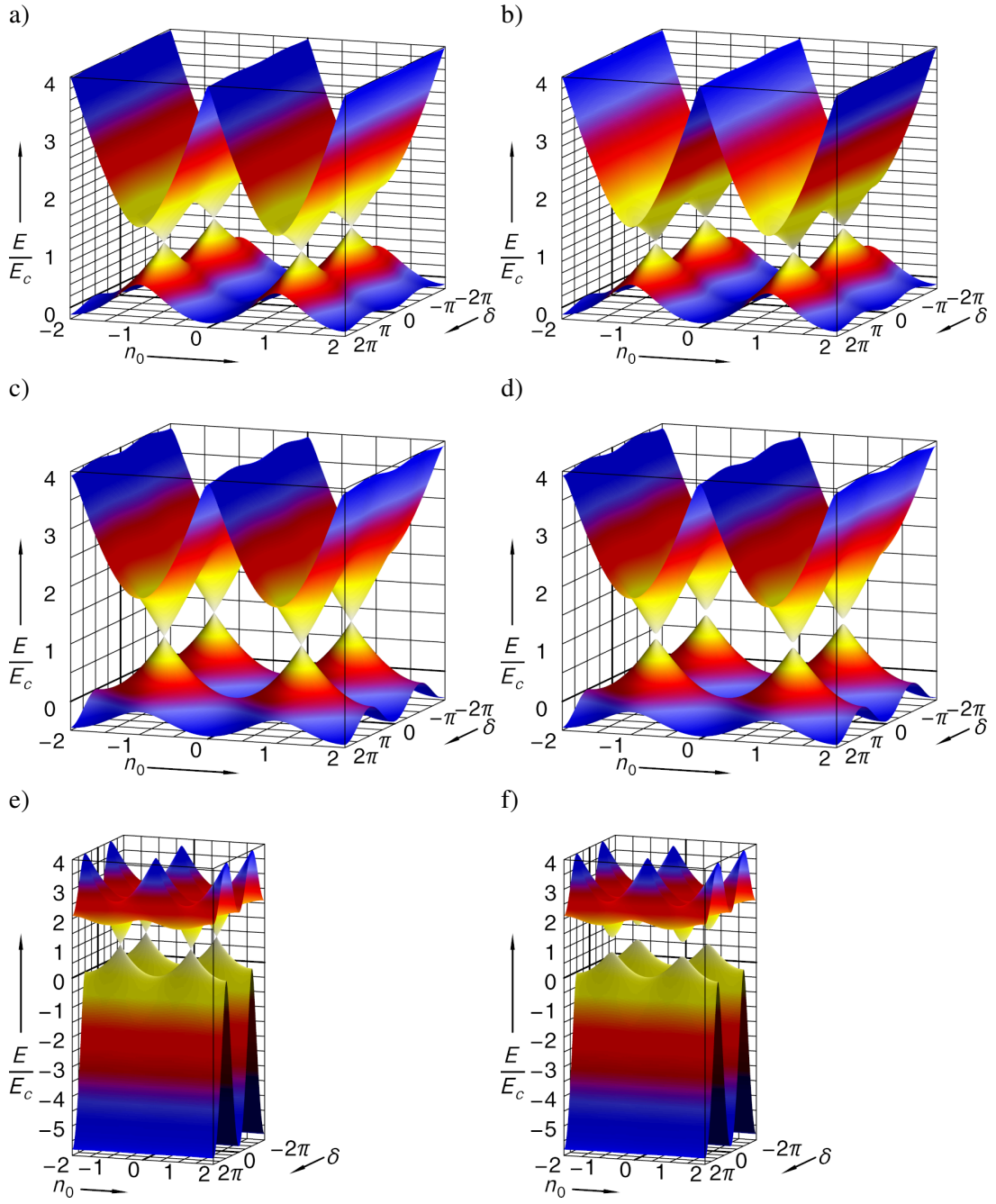


Figure 2.14: 3D plot of the two lowest energy bands as functions of $\delta$ and $n_g$ with different $E_j/E_c$ ratios for symmetric ($E_{j1} = E_{j2}$) and asymmetric CPTs ($\kappa = (E_{j1} - E_{j2})/(E_{j1} + E_{j2})$). The parameters for the six plots are: a) $E_j/E_c = 0.5$, $\kappa = 0$; b) $E_j/E_c = 0.5$, $\kappa = 0.1$; c) $E_j/E_c = 1$, $\kappa = 0$; d) $E_j/E_c = 1$, $\kappa = 0.1$; e) $E_j/E_c = 5$, $\kappa = 0$; f) $E_j/E_c = 5$, $\kappa = 0.1$.

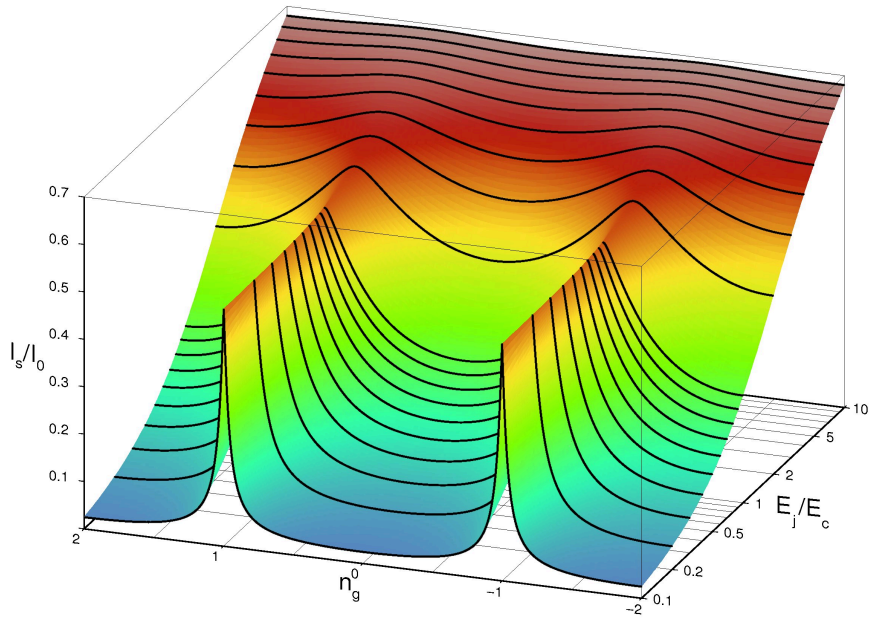


Figure 2.15: Modulation of the critical current of a CPT with gate-induced charge $n_0$ and the $E_j/E_c$ ratio, with eleven lowest levels taken into the numerical calculation. $I_0$ is given by $I_0 = E_j\pi/\phi_0$. Here $E_{j1} = E_{j2}$, i. e. $\kappa = 0$.

Fig. 2.15 shows the critical current $I_s$ as a function of $n_0$ for $\kappa = 0$. We define a further function $\epsilon$ by

$$1 - \epsilon(n_0) = \frac{I_s(n_0)}{E_0(n_0)} \times \frac{\Phi_0}{2\pi}. \tag{2.24}$$

Fig. 2.16 displays $\epsilon(n_0)$ as function of $E_j/E_c$. $\epsilon(n_0)$ is always smaller than 10% and can be ignored in many situations. We then get from Eq. 2.24

$$I_s(n_0) = \frac{2\pi}{\Phi_0} E_0(n_0) \tag{2.25}$$

which has the same dependence as the switching current on the Josephson couplings in single Josephson junction. This justifies to call $E_0(n_0)$ the effective Josephson coupling energy of the CPT. $f_0(\delta, n_0)$ takes the role of the $\cos(\varphi)$ term in the potential energy $E_j \cos(\varphi)$ of the single Josephson junction.

In reality, this calculated critical current will never be measured in real experiments. The electromagnetic environment has a strong influence on the observable critical current just as in the single Josephson junctions (see Chap. 2.2). The only difference is that the switching current is now gate charge dependent, leading to a periodic behavior along the dimensionless charge $n_0$. The relation between the switching current $I_s(n_0)$ and the critical current $I_0(n_0)$ for overdamped transistor can be written as (Ågren, 2002)

$$I_s(n_0) = I_0(n_0)g(\alpha), \tag{2.26}$$

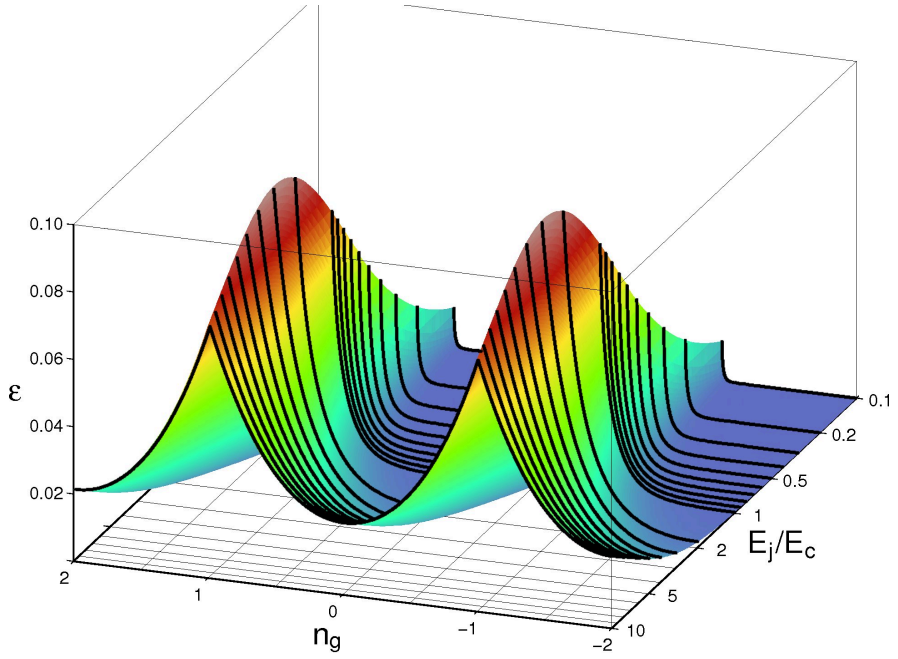


Figure 2.16: $\epsilon(n_0)$ (see text) calculation using eleven charge states, as a function of gate charge $n_0$ and $E_j/E_c$ ratio.

Where $g(\alpha)$ is introduced at the end of Sec. 2.2 (see Fig. 2.11). The function $g(\alpha)$ depends on the ratio $\alpha = E_j/k_BT$ and describes how finite temperatures affects the actually measured $I_s$, compared to the critical current.

### 2.3.3 Equilibrium quasiparticle poisoning model

The $2e$ periodic gate modulation of the charge transport through the Cooper-pair transistor is strongly affected by the presence of unpaired quasiparticles on the transistor island which can smear out the $2e$ periodic gate modulation of the switching current, an effect called "quasiparticle poisoning". In principle one is faced with two types of excitations, one of which is nicknamed "equilibrium quasiparticles". This type is due to thermal excitation of Cooper pairs and thus the number of equilibrium quasiparticles vanishes if the temperature is low enough. In practice, in most cases quasiparticles can be observed even at the lowest temperatures when thermal excitations can be ruled out. This type of quasiparticles are nicknamed "non-equilibrium quasiparticles". The origin of this excitation is not well-known up to date. In the following, we will discuss briefly the model dealing with equilibrium quasiparticles, while leaving the discussion on non-equilibrium quasiparticles to Chap. 5.

The phenomenon of equilibrium quasiparticle poisoning has been studied both theoretically and experimentally by many groups around the world (Joyez et. al., 1994; Joyez, 1995; Amar et. al., 1994; Ågren et. al., 2002; Averin and Nazarov, 1992; Lu et. al., 1996; Tuominen et. al.,

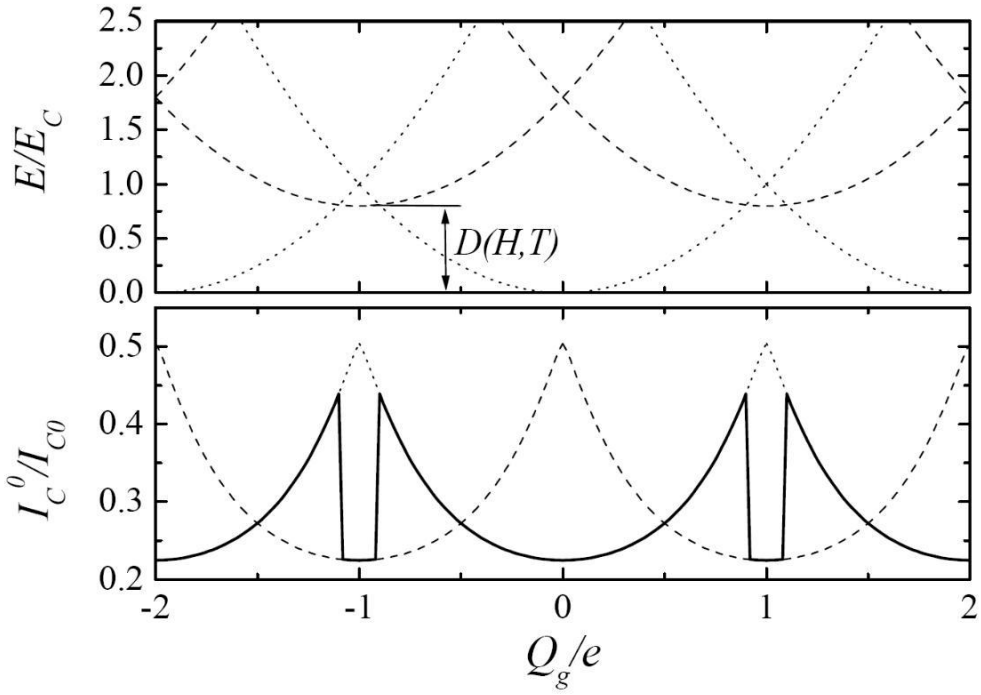


Figure 2.17: (Ågren et. al., 2002) The upper graph shows the lowest energy bands for even parity (dotted lines) and odd parity parity (dashed lines). The lowest energy for odd parity is lifted by $D(H,T)$, compared to the lowest energy for even parity. The lower graph shows the critical currents for both parities (dotted for even and dashed for odd). The solid line shows the respecting critical current (It is even parity at some ranges of the gate voltage but switches to odd parity at the other ranges.)

1993, 1992; Matveev et. al., 1993). This model suitable for describing the equilibrium quasiparticles in a CPT considers it to be in either one of two distinct states: one called even parity (the island is free of quasiparticles and all the electrons are paired into Cooper pairs), and another one called odd parity (one unpaired quasiparticle on the island). The extra energy required to have odd parity state compared to the even state on the island is given by the so-called odd-even free energy difference (e.g. Tinkham, 1996)

$$D(H,T) = \Delta(H,T) - k_B T \ln N_{\text{eff}}(H,T), \tag{2.27}$$

where $\Delta(H,T)$ is the superconducting gap and $N_{\text{eff}}$ the effective number of quasiparticles states available for thermal excitation. At low temperatures $N_{\text{eff}}$ can be approximated by

$$N_{\text{eff}}(T) \approx V_i \rho_n(0) \sqrt{2\pi\Delta(H,T) k_B T}, \tag{2.28}$$

where $V_i$ is the volume of the island and $\rho_n(0)$ is the normal density of states of aluminum. A Cooper-pair transistor with an odd parity on the island can show supercurrent of just the same

size as the one with even parity, but with a gate modulation shifted by $e$. Thus the critical current is still $2e$ periodic in gate charge, but with the peaks at $n_g^{even} = 2n$.

In the ideal case, the odd/even parity is directly determined by the odd-even parity difference, $D(H,T)$. If $D(H,T)$ is larger than the charging energy of the island $E_c$, the island will be in an even state in equilibrium. If $D(H,T)$ is smaller than the charging energy $E_c$, it is energetically favorable for a quasiparticle to stay on the island. This odd-even parity difference is illustrated in Fig. 2.17. The odd parity results in dips in the critical current versus gate charge which is referred to as quasiparticle poisoning regions[9].

The odd-even parity can be tuned by the applied magnetic field or temperature. The superconducting energy can be suppressed by the magnetic field and the $D(H,T)$ gradually decreases. So when $D(H,T)$ slowly approaches the charging energy $E_c$, odd parity occurs, at some range of the gate voltage. The original critical current peak is not showing up any more. Instead the maximal critical current is observed at the positions when the parity switches. $D(H,T)$ is reduced with increasing temperature and parity is affected as well. The crossover temperature $T_0^*$ from $2e$ to $e$ periodicity is given by

$$T_0^* = \frac{\Delta(H,T^*) - E_c}{k_B \ln N_{\text{eff}}(T_0^*)} \tag{2.29}$$

This model ignores external excitations, e.g. noise from the measurement electronics or black body radiation from the 4 Kelvin stage in the cryostat are not included in this model for the parity switching. These non-equilibrium quasiparticle excitations are a dynamic effect which affects the switching current measurements in a more complicated way.

[9] Note that full 2e periodicity can be expected even at zero temperature for $E_c < \delta$ only. This condition is supposed to hold here.

# 3 Sample preparation

The material of choice for the study of single charge transport in mesoscopic devices is aluminum, for several reasons:

- First of all, tunnel junctions, which are the crucial parts in all the devices investigated for this thesis, can easily be prepared using aluminum. Tunnel barriers are formed between two partly overlapping layers of aluminum by converting the surface of the bottom layer to $AlO_x$ in a controlled oxygen atmosphere. Given by the nature of aluminum, this oxidization is a self-terminating process which leads to a homogenous insulating film without pin-holes.
- Second, the insulating barrier thickness is directly related to the oxygen pressure during oxidization. Thus the tunneling transparency can be tuned just by varying the oxygen pressure (e.g. Limbach, 1998).
- Last but not least aluminum becomes superconducting at 1.18 K and has a critical magnetic field of a few mT (e.g. Hunklinger, 2007). These properties offer the chance to study the charge transport in mescoscopic devices at low temperatures in the normal conducting as well as in the superconducting regime by switching the magnetic field on and off.

For the realization of single charge experiments, Coulomb blockade plays a major role. A close study of this effect requires the charge transport not to be dominated by thermal excitations, i.e. $E_c \gg k_B T$. As the $^3$He/$^4$He dilution refrigerator used for our experiments can be operated at temperatures well below 30 mK, fulfillment of the above equation is given for $E_c/k_B \geq 1$ K. This leads to the condition $C \leq 1 \cdot 10^{-15}$ F for the capacitance of the tunnel contacts in our samples.

Due to the extremely thin tunnel barrier (approx. 2 nm), the contact area of the tunnel junctions should be smaller than $100 \times 100\,\mathrm{nm}^2$ to keep the capacitance of the junctions smaller than $1 \cdot 10^{-15}$ F, according to the simple formula for plate capacitors.

For the preparation of our samples we therefore apply a method which by now has become a standard procedure (Niemeyer, 1974; Fulton and Dolan, 1987). Our process is based on two techniques: optical and electron beam lithography. We chose the combination of both to optimize speed and resolution. On the one hand optical lithography is fast but cannot achieve the dimensions described above. For this purpose e-beam lithography is needed. On the other hand macroscopic connections of the devices to the measurement setup are required. Creating these by electron beam lithography is a time consuming business. Therefore it is preferable to prepare them beforehand by optical lithography.

Works previously published in our group already give extensive descriptions of our sample preparation technique. In the theses of Sypli and Limbach (Sypli, 1997; Limbach, 2002), a

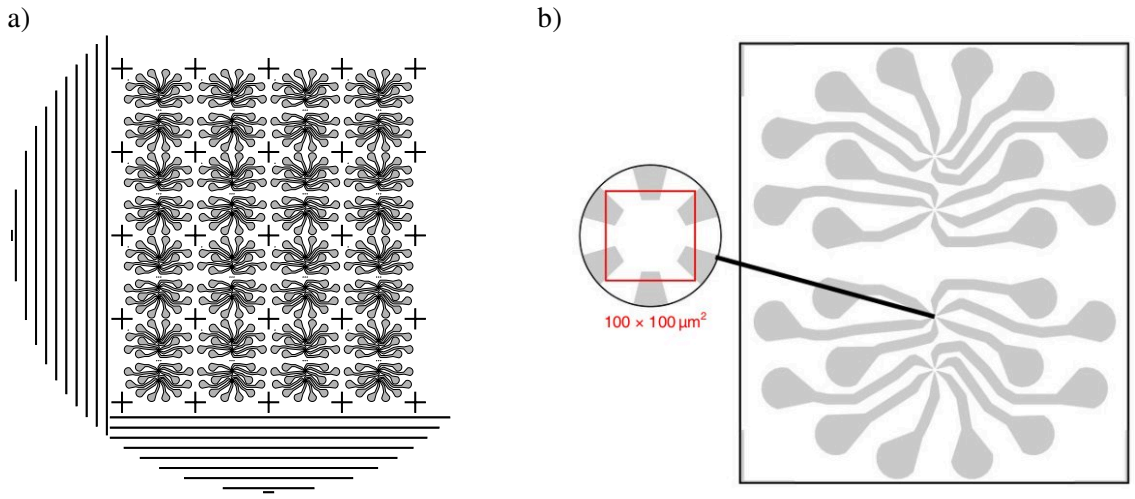


Figure 3.1: a) Mask layout for optical lithography. On each wafer of ⌀ = 2 inches 16 chips of 7.5 × 8.5 mm$^2$ are structured in a single exposure step. b) On every chip 24 macroscopic gold pads are prepared. Always 6 of them are connected to one of the four 100 × 100 µm$^2$ positions for the fine structures.

detailed description of mask preparation and shadow evaporation is given. However, due to equipment changes, further improvements have been made recently. This chapter will focus on the new developments while keeping the explanation of the structuring steps already described by the above mentioned theses relatively short.

## 3.1 Pre-structuring of macroscopic leads

The mesoscopic devices we want to study need good electrical contact to our experimental setup. Macroscopic leads, i.e. in the range of µm to mm, are required. To prepare these, optical lithography, which has a precision in the range of micrometers, is a time saving alternative to the much slower electron beam writing. Fig. 3.1 shows the layout of the mask we use for optical lithography. The substrates, 275 µm thick boron doped silicon wafers of 2 inches diameter with a polished and thermally oxidized surface, were purchased from *CrysTec*. We chose so because the 400 nm thick $SiO_x$ layer provides an insulating barrier between the silicon and the structures prepared on top.

For the macroscopic leads, three layers of metal (Ti, Cu and Au) are evaporated thermally onto the silicon wafers. After that, they undergo optical lithography: covering with resist by spin coating, exposure to UV light under a mask (see Fig. 3.1 a) ) and development. The metal is then shaped by ion etching. Finishing steps are the cutting of the wafers into 16 chips of 7.5 × 8.5 mm$^2$ and the removal of the un-exposed resist.

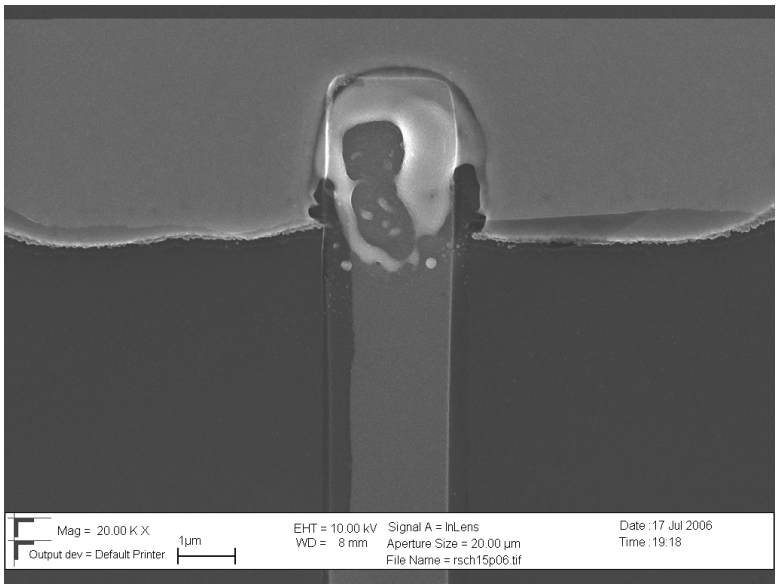


Figure 3.2: Contact between optically structured lead consisting only of gold on titanium and an aluminum lead. A gap interrupts the electric connection due to the formation of an Au-Al-alloy.

### 3.1.1 Metal deposition

Before optical lithography, the sample wafers are covered with three layers of metal by thermal evaporation. In our setup (shown in Fig. 3.3), a tungsten wire (0.1mm diameter) heated by a current of around 3.8 A serves as a hot cathode. It forms a coil around a tungsten or tantalum cup which contains the material to be evaporated and at the same time constitutes the anode. A high voltage $V$ of a few hundred volt drags the electrons from the tungsten wire towards the cup, resulting in heating and finally evaporation of the source metal when the power $P = IV$ is high enough. As the metal vapor reaches the substrate, it condenses there, forming metallic layers. For our purpose, three layers of metal are deposited: titanium, copper and gold. Titanium provides good sticking for the subsequent metal layers. Only a very thin film of 1-2 nm is needed. Initially a gold layer was deposited next but it turned out that it forms an alloy with the aluminum comprising the fine structures (see Fig. 3.2), thereby cutting off the connection. Thus we changed from gold to copper but unfortunately this led to another problem: if the metal was covered with the MAA resist used for e-beam lithography and heated to the required temperature of 150 °C, an insulating green layer of some copper salt formed on the optically structured leads. In the end the best results were achieved if on top of the titanium layer around 30 nm of copper were evaporated, followed by approximately 20 nm of gold.

The evaporation takes place in a self-built chamber. It is relatively small (ca. 5 liters), so that it can be evacuated quickly with a turbo pump to a pressure well below $10^{-4}$ Pa. Figure 3.3 shows its setup. For the copper source a thin tantalum foil is used, whereas gold and titanium are evaporated from tungsten foil. The thickness of the evaporated metallic layers is monitored

by measuring the frequency change of a quartz oscillator which is mounted right next to the sample holder. [1]

### 3.1.2 Optical lithography

For optical lithography a negative photoresist (AZ6632 mixed with PGMEA 5:1 in mass) is applied to the wafer surface by spin coating at a speed of 5000 rpm for 90 s. Afterwards, the resist is dried in an oven at 100 °C for 20 min ("soft baking").

In the following, the wafer is brought into hard contact with the quartz/chromium mask shown in Fig. 3.1 using a mask aligner and exposed to the UV-light of a mercury lamp for 5 seconds. The exposed areas are washed away with a developer (AZ351B diluted with water) in about 45 seconds. The wafer is then cleaned in three successive baths of de-ionized water and dried with compressed air blown to its surface. Hardbaking is omitted as the etching procedure is normally started immediately after optical lithography.

### 3.1.3 Ion etching

After optical lithography the parts of the metal films which are not covered by photoresist any more are removed by ion etching. In a chamber equipped with an iongun, argon pressure is increased to $6 \cdot 10^{-2}$ Pa to ignite a plasma, then reduced to $3 \cdot 10^{-2}$ Pa for stable operation. The ion energy is set to 250 eV and the ion current to 20 mA. The removal of 80 nm of metal takes 10 min.

We found out that the removal of the photoresist is much easier when the ion-etching is done in 20 independent steps of 30 seconds each. Therefore we guess that a continuous etching process causes excess heating, resulting in polymerization of the resist, which makes it less easily removable.

### 3.1.4 Wafer cutting

As soon as the etching process is completed, the whole wafer is deposited in a bath of pure acetone overnight. Should this not be sufficient to get rid of the photoresist, an ultra-sonic bath with around 50 °C is applied, until all remains are removed. Finally, every wafer is cut with a diamond cutter into 16 chips (see 3.1), which are then processed separately by electron beam lithography.

## 3.2 Preparation of fine structures

In this chapter, the preparation of the so-called fine structures will be described in detail. Electron beam lithography is used as the key technique for acquiring ultra-small devices needed for single charge investigations. We will start with an outline of the procedure of this technique. After that, we will explain the dose study we made to improve the layout design. Some samples

[1] It is mounted as close to the sample holder as possible to keep consistency with the layer thickness on the wafer.

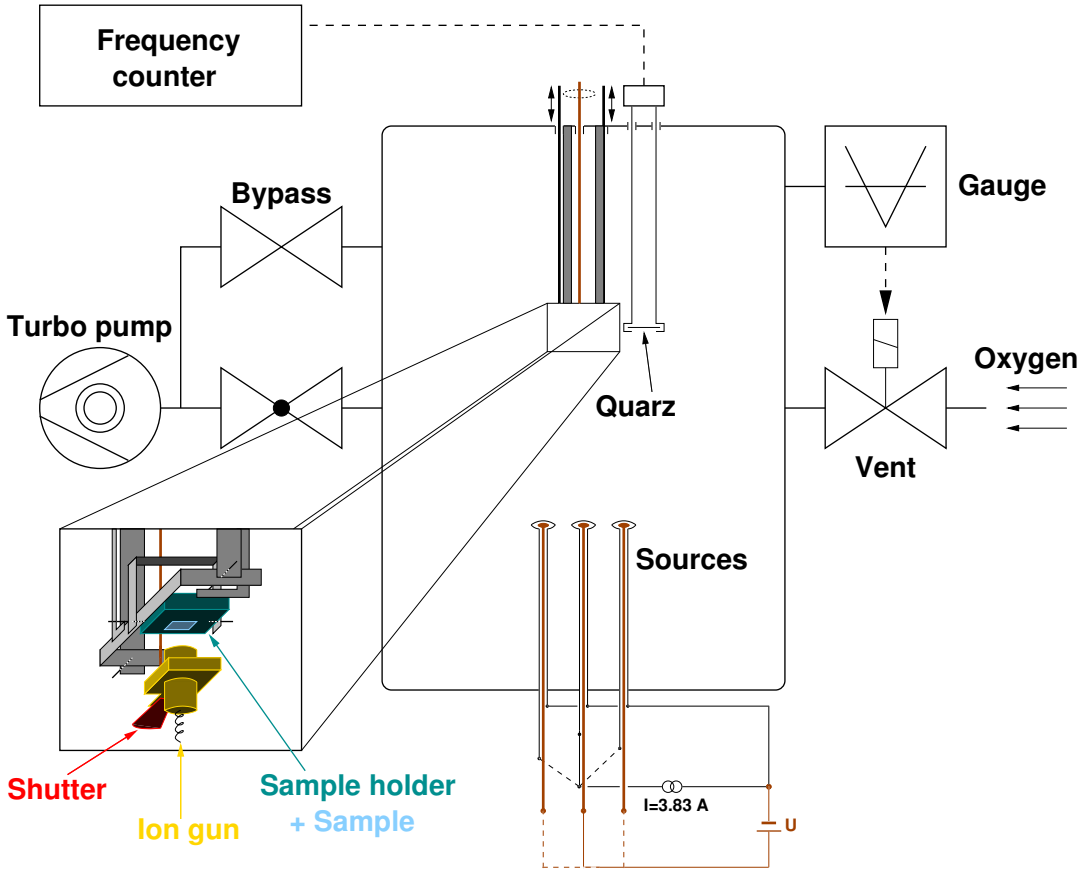


Figure 3.3: Sketch of the high vacuum evaporation chamber used for sample preparation. The middle bottom part shows the evaporation sources. They are surrounded by a coil from tungsten wire of 0.1mm diameter, through which a current of about 3.8 A is drawn during operation. A voltage drop between source (anode) and tungsten wire (cathode) drags the electrons to the source, leading to the melting and evaporation of the metal source. The left-bottom inset shows the mechanical construction near the sample holder. The dark-blue block is the sample holder which can be rotated along the marked axes in two directions (shown in black color in this inset). The light-blue square marks the position where the sample is mounted. The red fan-shaped object is the shutter attached to the ion gun. It is closed against the sample at the beginning of evaporation to avoid the deposition of impurities from the metal source. Only after a constant flow is achieved, which means the impurities with lower melting temperature are almost all evaporated out, we open the shutter and start our metal deposition.

fabricated for this work require two separate electron beam lithography steps. This good match between these two electron beam lithography steps is crucial. The fine writefield alignment technique especially tailored to solve this problem will be introduced in this section. We will also briefly review the well known shadow evaporation technique for material deposit in this part.

### 3.2.1 Electron beam lithography

The previous preparation of macroscopic leads on each sample chip by optical reduces the e-beam lithography structuring time tremendously. Nevertheless, this latter method is crucial to acquire the resolution needed for our ultra-small mesoscopic devices.

Like optical lithography, e-beam patterning requires a medium to transfer the written structures to the surface. Films of polymers whose chemical bonds can be modified by electrons are necessary. Similar to the steps described in the previous chapter, they are applied to the sample via spin coating, then exposed and developed. However, other than for the macroscopic leads, the metal of choice, in our case mostly aluminum, is evaporated after e-beam lithography. In the lift-off step we get rid of superfluous metal parts and are left with the desired fine structures.

Although the electron beam itself has a very small spread of only a few nm, the lower resolution limit for structuring is one order of magnitude larger. This is due to the fact that the main exposure is not due to the primary electron beam but rather due to secondary electrons which are generated by the collision of the incoming electrons with the resist. These secondary electrons have a much lower mean energy and a considerably higher crosssection for cracking the polymer chains. Thus the area exposed is determined by the mean distance over which the secondary electrons give their power to the resist. We will discuss this effect further in the subsection 3.2.1.2.

#### 3.2.1.1 Procedure

For e-beam lithography, every chip is coated with a two layer system of resists, which consist of polymers in solution. We chose a first film of the copolymer MMA (8.5) MAA EL11 (methylmetaacrylate-co-methylacrylate acid in 89% ethyl lactate), short MAA, and on top polymethylmethacrylat with molecular mass 950 kg/mol, solved in 98% anisol, short PMMA 950 K. Both chemicals are dispersed on the sample surface by spin coating at 4000 rpm for 90 s in a clean room. After each coating the sample is baked in an oven at 150 °C for 30 min to remove the solvent. DEKTAK measurements revealed the thicknesses of MAA- and PMMA-films to be approximately 470 nm and 220 nm, respectively.

After resist application the sample is ready for patterning with the SEM. Our e-beam lithography is performed with a scanning electron microscope LEO 1530 equipped with the pattern generator Elphy Plus from Raith GmbH. An additional electrically driven piezo nanostage allowing a positioning of the sample with a precision of a few nm is built to the SEM. The pattern generator drives the e-beam along the desired geometric patterns. For exposure of the MAA/PMMA system, a beam energy of 30 keV is used. The dose $D$ necessary to get the correct exposure for every shape is previously determined in the layout design with the help of a

simulation program, as will be explained in the following subsection 3.2.1.2. Usually it lies around $D$ =300 µA·s/cm$^2$.

The electron beam breaks chemical bonds in the polymers, thus shortening their chains. The shorter molecules are then far better dissoluble in the developer. The e-beam dose for a proper exposure of the copolymer is much lower than that required for PMMA. Thus the upper layer defines the actual structures one would like to have, whilst the lower one causes a larger opening to provide space for the shadow evaporation which will be described in section 3.2.2.

When the desired pattern has been written onto the double resist layer, it is developed in a mixture of isomethylbuthylketon and isopropanol with a volume ratio of 1:3 for 45 s whilst stirring with a magnet bar. To wash away the remains of the developer, the sample is put in pure isopropanol for about a minute. Through the remaining resist mask the structures written with the e-beam are transferred to the sample surface by evaporating the material of choice.

#### 3.2.1.2 Dose study

As was mentioned at the beginning of this section, secondary electrons are mainly responsible for the exposure of the polymers. They are generated in collisions of the impinging primary electrons with the resist and the substrate. Their scattering in resist and substrate leads to an enlargement of the exposure region defined by the primary electrons. The majority of the electrons do not stop in the resist but rather penetrate into the substrate. Here more interaction between the primary beam and matter happens, leading eventually to a backscattering of high energetic electrons. The backscattering results in a larger cone of electrons penetrating the resist from behind and causing a further exposure of considerable amount. It is responsible for the so-called proximity effect: Smaller, isolated structures might receive insufficient dose, while closely packed or larger structures are properly developed with the same exposure. This effect must be taken into account in the pattern design, especially when writing small structures in the sub-µm range.

The electron spread can be described by a point spread function ($PSF$). Usually a double Gaussian is used (e.g. Aparshina et. al., 1997), which also for our work proved fully sufficient:

$$PSF(r) = \frac{1}{\pi(1+\eta)} \left( \frac{1}{\alpha^2} e^{-\frac{r^2}{\alpha^2}} + \frac{1}{\beta^2} e^{-\frac{r^2}{\beta^2}} \right) \tag{3.1}$$

The standard deviation of the first Gaussian, $\alpha$, describes the beam spot enlargement due to secondary electrons generated in the resist. For a beam diameter of 1 nm, a thick resist layer ( > 0.25µm) and a relatively low electron energy ( < 50 keV), the size of $\alpha$ depends mainly on the resist thickness $t$ and the beam energy $EHT$. Usually $\alpha$ is of the order of few tens of nanometers (Broers, 1981). $\beta$ is a measure for the electron spread due to backscattering of electrons from either the substrate or the resist. The value of $\beta$ is determined by the beam energy, the resist and the substrate material. Last, $\eta$ describes the ratio of the dose division between forward ($\alpha$) and backward ($\beta$) scattering (Leunissen et. al., 2004). We used a self-written simulation program based on 3.1 to test our structure design before the actual e-beam lithography. Its application requires the knowledge of the three parameters $\alpha$, $\beta$ and $\eta$ explained above as well as the value

of the base dose $D_0$, i.e. the dose really required to develop through both layers of the resist system.

Except for $\alpha$ all parameters were found experimentally by evaluating the development of reference structures especially created to that end. However, as $\alpha$ is much smaller than $\beta$, and therefore causes a comparably small spread, experimental determination is difficult. It was therefore calculated with an empirical formula derived in (Broers, 1981), which holds under the conditions mentioned above:

$$\alpha = \left( \frac{9.64 \cdot t(\mu\text{m})}{EHT(\text{keV})} \right)^{1.75} \tag{3.2}$$

For our parameters $t \approx 700\,\text{nm}$ and $EHT = 30\,\text{keV}$, evaluation of 3.2 yields $\alpha = 10\,\text{nm}$.
For the experimental determination of $D_0$, a series of directly adjacent bars of $1 \times 30\,\mu\text{m}^2$ was written. The dose increased from each bar to the next in 10% steps from 50% $D$ to 150% $D$. Thus it was guaranteed that (apart from the points near the edges) every point really received the nominal beam dose, i.e. $d = x\% \cdot D$, $x \in [50; 150]$. A crucial point was the length of the bars (30 µm), which has to be larger than $6 \cdot \beta$ to neglect the dose loss by backscattering. Under this conditions the dose $\tilde{x}\% \cdot D$ for which development starts represents the base dose $D_0$: $\tilde{x}\% \cdot D = D_0$. Averaging over values received for varying $D$, the result was $D_0 = 141 \frac{\mu\text{A}\cdot\text{s}}{\text{cm}^2}$ (compare 3.4). The next necessary step was to find $\eta$. The method is illustrated in 3.5:
A series of isolated (spaced 5 µm apart) dots of small size ($100 \times 100\,\text{nm}^2$) is patterned with an e-beam. The dose runs again from 50% $D$ to 150% $D$ for various $D$. For such small and isolated features, only forward scattering determines the deposited dose $d = (1-\eta) \cdot x \cdot D$. After the sample preparation was completed, the number of squares created for each $D$ was counted. This gives the threshold dose $D_1 = x \cdot D$ above which a dot is developed, i.e. $D_0 \leq (1-\eta) \cdot D$. Thus $\eta = (D_1 - D_0)/D_0$ was found to be $\eta = 0.9$. Knowing $D_0$ and $\eta$, $\beta$ can be determined with the bars illustrated in Fig. 3.4 with a method similar to the one applied for $D_0$. As in Fig. 3.4 d), simulation and photo are overlaid once again, this time fitting the form of the borders of the developed areas by changing $\beta$. This yielded $\beta = 4.0\,\mu\text{m}$.

With the determined parameters $\alpha = 10\,\text{nm}$, $\beta = 4.0\,\mu\text{m}$, $\eta = 0.9$ and $D_0$=141µA·s/cm$^2$, the dose factors for proper exposure of all structure components can be adjusted in the layout process without further writing trials.

### 3.2.2 Shadow evaporation

After the development of the resist mask created by e-beam lithography, metal is evaporated onto the sample in the evaporation chamber mentioned already in Sec. 3.1.1 and sketched in Fig. 3.3. Before the metal deposition starts, the substrate surface is cleaned by plasma etching. Argon is let into the chamber until pressure of 30 Pa is reached. We then ignite a plasma with a power of 2 W, which is directed onto the sample surface for 2 min. The plasma burning is confined in a plasma gun which is depicted in Fig. 3.6. This procedure greatly improves contact formation between the optically structured gold leads and the aluminum fine structures.

The technique we use to deposit aluminum is referred to as shadow evaporation. It is sketched in Fig. 3.7. The main idea is to evaporate material under two (or possibly more) different angles

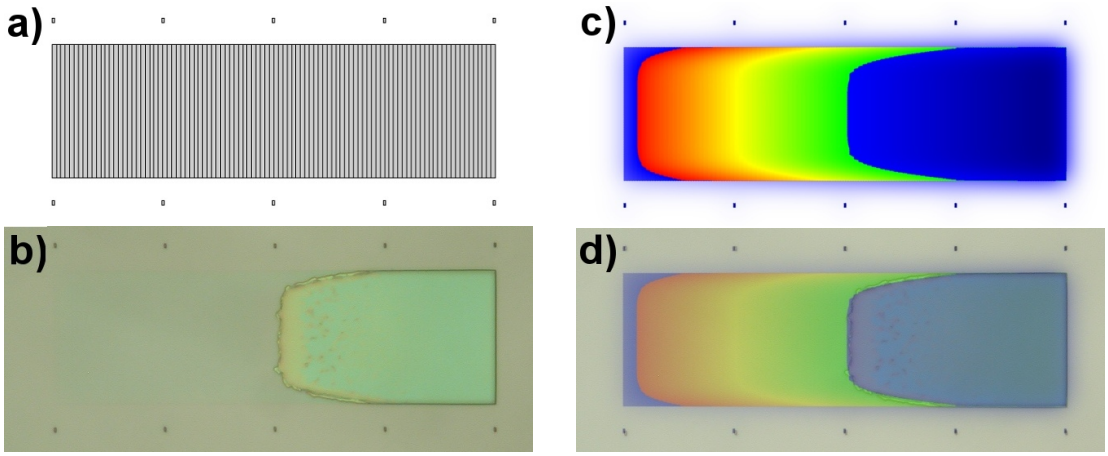


Figure 3.4: Dose study to get the base dose $D_0$ and $\beta$ for our special resist system (470 nm MAA plus 220 nm PMMA 950 K) and substrate material (p-doped Si covered by 400 nm of oxide). a) shows the reference structure designed for this purpose: A series of directly adjacent bars of $1 \times 30\,\mu m^2$ written with from left (50% $D$) to right (150% $D$) in 10% steps increasing dose. b) is a camera picture of the structure taken after development. c) is the corresponding simulation. Red to green represents increasing dose, while blue on the right end corresponds to completely developed resist and on the left end to some very low exposure. d) illustrates the parameter fitting: simulation pictures with varying $D_0$ were laid across the photo until the left edges of the developed regions corresponded. The resulting base dose was $D_0$=141µA·s/cm$^2$. $\beta$ could only be found after the determination of $\eta$ (see 3.5) by adjusting the form of the borders of the developed area. We got $\beta = 4.0\,\mu m$.


Figure 3.5: a) To find $\eta$, a series of 21 dots of $100 \times 100\,nm^2$ spaced 5 µm apart was written with the SEM. The dose was varied from 50% $D$ to 150% $D$ for different values of $D$. b) Counting of squares for each $D$ gives the threshold dose $D_1 = x \cdot D$ above which a dot is developed. Thus $\eta = (D_1 - D_0/D_0)$ was found to be $\eta = 0.9$.

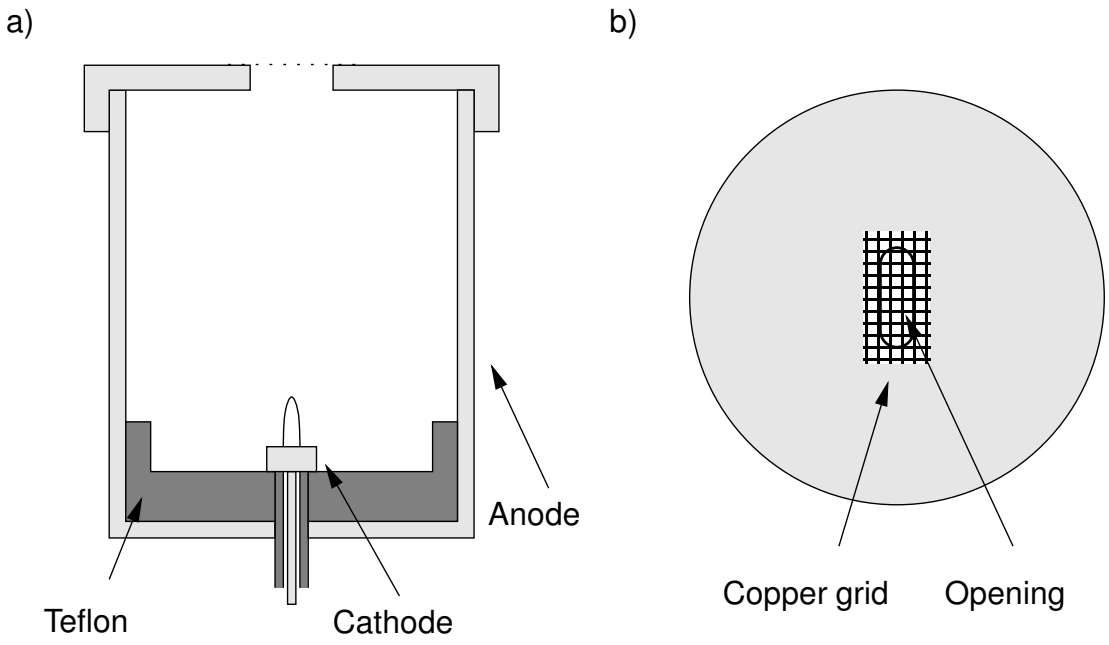


Figure 3.6: A sketch of the plasma gun we use to clean sample surfaces by sputter erosion. a) shows the cross-section of the gun and b) is the top-view of the cover. For operation, an argon pressure of about 30 Pa is created in the vacuum. Then plasma is ignited by the application of a voltage between cathode and anode. The surface of the sample which is mounted close to the gun is cleaned by the collision of ions with the surface.

onto the resist mask. The same pattern is then transferred to the substrate at different positions, acquiring the intended overlap between the deposited materials. For the fabrication of the single charge transistors studied in this thesis, the following procedure is sufficient:
A first aluminum film is deposited onto the sample with the sample holder tilted by 7° in one direction. Afterwards oxygen is let into the chamber to oxidize the surface of the first aluminum film. The thickness of the oxide barrier, and hence the tunneling transparency of the junctions, is determined by the oxygen pressure during this step, which is controlled with a PID controller. The oxygen pressure is adjusted between 0.5 Pa and 15 Pa, depending on the intended barrier thickness. Subsequently a second layer of aluminum is deposited with a tilt of 7° of the sample holder in the opposite direction. With the chosen angles, an overlap between the first and second aluminum layer can be formed with an insulating layer in between. Thus a tunnel junction is created.

Finally the resist mask is removed from the sample in the so-called *lift-off*: The polymer layers are dissolved in an acetone bath. At the same instant, the metal film on top is removed. Last, the sample is cleaned in a 1:1 solution of ethanol and toluol and then spin-dried. It is now ready to be contacted via bonding.

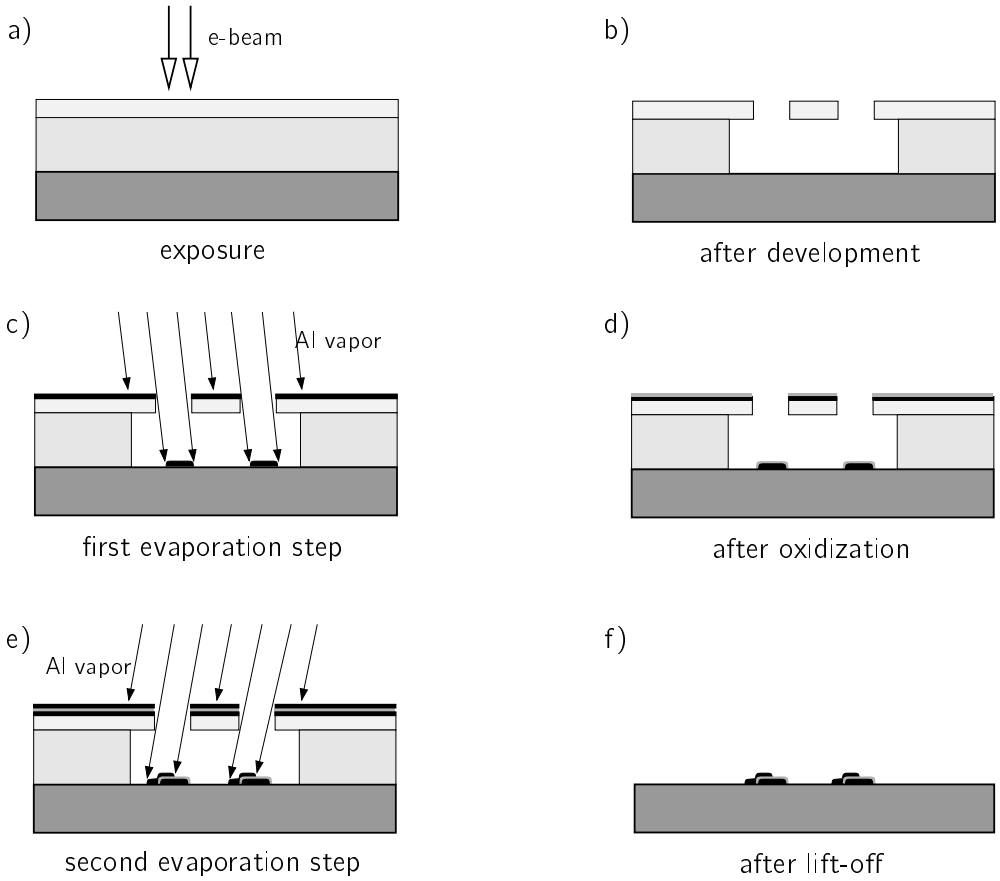


Figure 3.7: A cartoon of the shadow evaporation technique. Dark grey represents the thermally grown $SiO_x$ layer on the Si substrate. The top resist layer consists of PMMA 950 K, the second of the copolymer MAA (compare 3.2.1.1). By changing the evaporation angle, metal can be deposited at different positions through the openings in the PMMA/MAA system. The lift-off removes the resist as well as the material on top, leaving only the metal condensed to the e-beam exposed positions on the wafer.

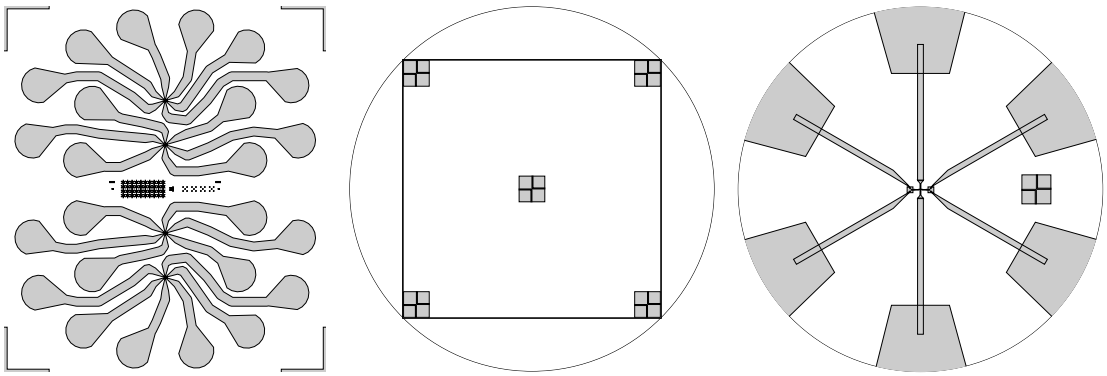

Figure 3.8: Illustration of the fine writefield alignment technique (see text). Left: Layout of an entire sample chip. Middle: One of the four mark positions on the middle right side of the chip. The usage of five marks guarantees a good recovery of the writefield expansion and rotation parameters used in the first writing step. Right: The writing area for fine structures. Another mark can be seen on the right side. It is used to precisely adjust the beam shift.

#### 3.2.2.1 Fine writefield alignment

For the investigation of single Cooper-pair devices, a good filtering of quasiparticle excitations is important. This can be achieved by placing normal metal leads close to the fine structures. Normal metals have continuous energy levels which can be used to relax the quasiparticle excitation states in the superconductor. The optical leads made from normal metals are located relatively far from the actual transistors. Thus they are not sufficient to relax the quasiparticle states excited close to the fine structure. To solve this problem, we have to put normal metal objects closer to the transistor. This is done by fabricating normal metal squares interrupting the superconducting leads in a separate electron beam lithography step.

Because of their relatively large size (2 × 2µm) and compact form, the normal metal boxes are less fragile than the transistors. Therefore they are written in a first e-beam lithography step, along with some alignment marks which enable the user to arrange the transistors in accordance with the boxes in the second e-beam writing process (see Fig. 3.8). Alignment consists of two steps. First, four sets of crosses are placed in the free region, which is the middle right part of the sample chip, are written in the first e-beam step. One of these sets is scanned in the second e-beam procedure and the writefield will be adjusted accordingly [2]. Second, the beam shift has to be adjusted precisely with respect to the structures created in the first e-beam step with the help of another alignment cross which is situated close to the fine structure positions. With this procedure, an accuracy of tens of nanometers can be achieved.

[2] The other sets are fabricated as backups. In case one of the sets is broken, we can quickly switch to another one for doing the fine alignment

## 3.3 Results of sample preparation

With the method described in this chapter, a large number of single electron transistors, coupled single electron transistors, nanoring structures and Josephson junction arrays have been fabricated.

In the following images, some of the samples we prepared are presented. The pictures were taken with a scanning electron microscope (SEM). Layers comprising of different metals can be distinguished. While the darker patterns are formed by aluminum, the brighter areas are covered with copper or gold.

### 3.3.1 Single electron transistors

Gold and copper were not only used for the connecting leads prepared by optical lithography. As they are still normal conducting at low temperatures below 1.18 K, where aluminum becomes superconducting, they were also employed for *quasiparticle traps*. These are designed as small metal squares interrupting the aluminum connections to relax the non-equilibrium quasiparticles (see Fig. 3.9 and Fig. 3.10).

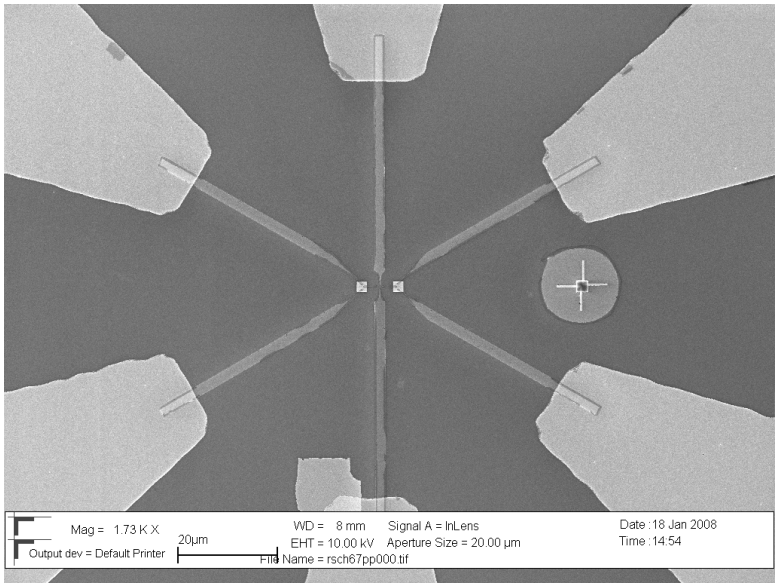


Figure 3.9: SEM picture of one of the single charge transistor samples. At the edges the optically made connecting leads are visible. Aluminum wires forming the fine structures were structured by e-beam lithography. They appear a bit darker. The brighter spots in the center are gold squares for *quasiparticle traps*.

In Fig. 3.10 the square shaped quasiparticle traps can be distinguished clearly from the transistors. They are prepared in an extra e-beam lithography step as described in subsection 3.2.2.1:

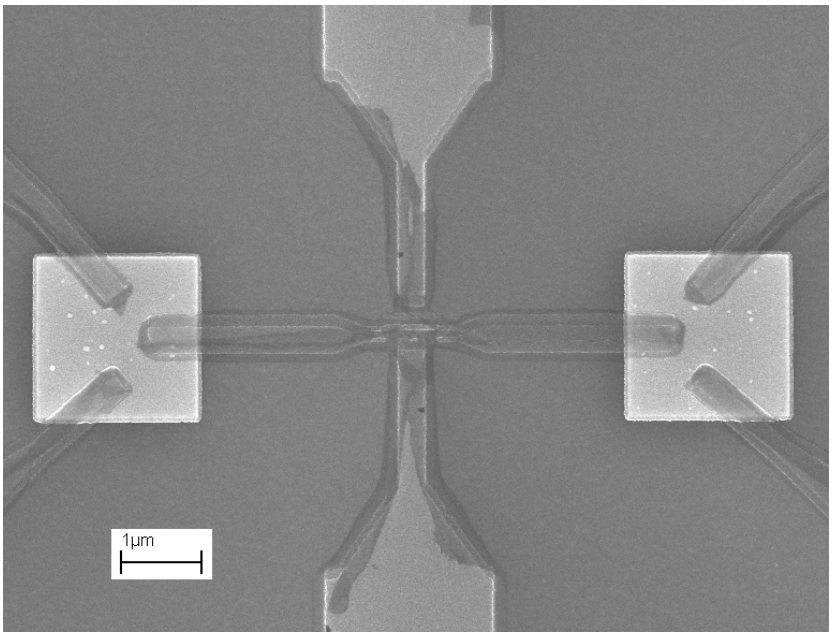


Figure 3.10: Zoom into the fine structure of a single charge transistor. The sample was made in two steps: First a normal conducting metal, e.g. copper, was evaporated onto the substrate. After another SEM writing process, aluminum was evaporated to form a nano-device interrupted by the normal metal.

The high magnification SEM picture shown in Fig. 3.11 shows the core of a single electron transistor sample. The overlap between the island and the connecting leads is around 40 × 40 nm$^2$. Thus the capacitance is small enough to give $E_c \ll k_b T$ (see section 2.1). Generally the tunnel contacts we realized had capacitances between 40 aF and 300 aF and conductances between $0.02\,G_0$ and $5\,G_0$, thus covering a wide parameter range suitable for single electron experiments (e.g. Wallisser, 2002; Limbach, 2002).

### 3.3.2 Josephson junction arrays

With our elaborated sample fabrication technique, a lot of other nanodevices can be realized, e.g. soliton samples, consisting of a series of Josephson junctions connected to each other (see Figs. 3.13 and 3.14).

The main difficulty in the sample preparation is to keep the loop size the same for all SQUIDs. We managed by carefully adjusting the shadow evaporation angles. In order to get 200 nm distance between material condensed on the substrate through the same opening in the resist mask, a tilt of the sample holder of about 9° in both directions is used for the shadow evaporation. Measurements on these soliton samples will be shown soon in publications of our group.

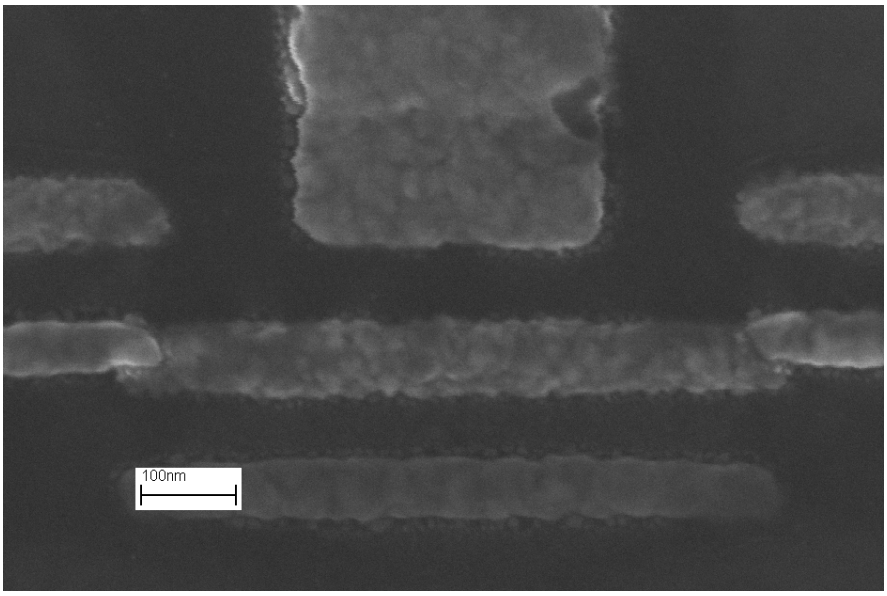


Figure 3.11: Zoom into the core of a single charge transistor. The island separated from the leads via two Josephson junctions as well as the gate can be made out.

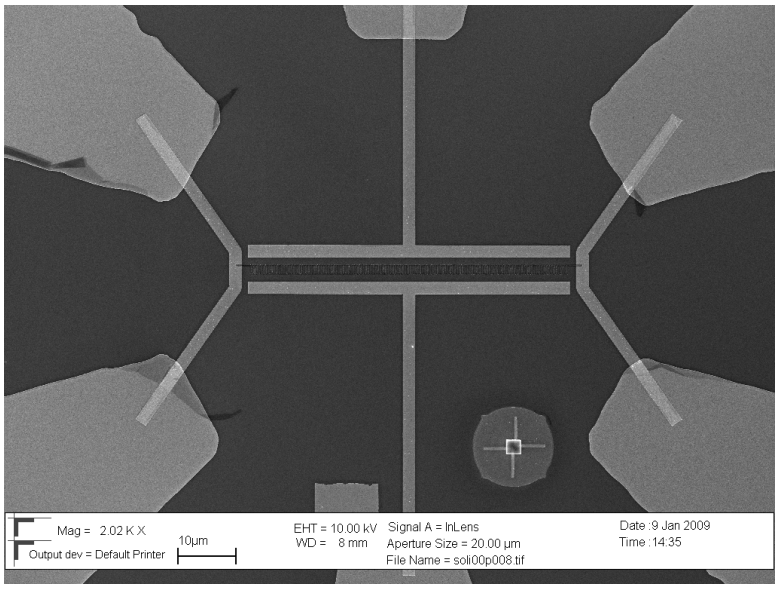


Figure 3.12: SEM picture of the 100µm ×µm writing area of a soliton sample.

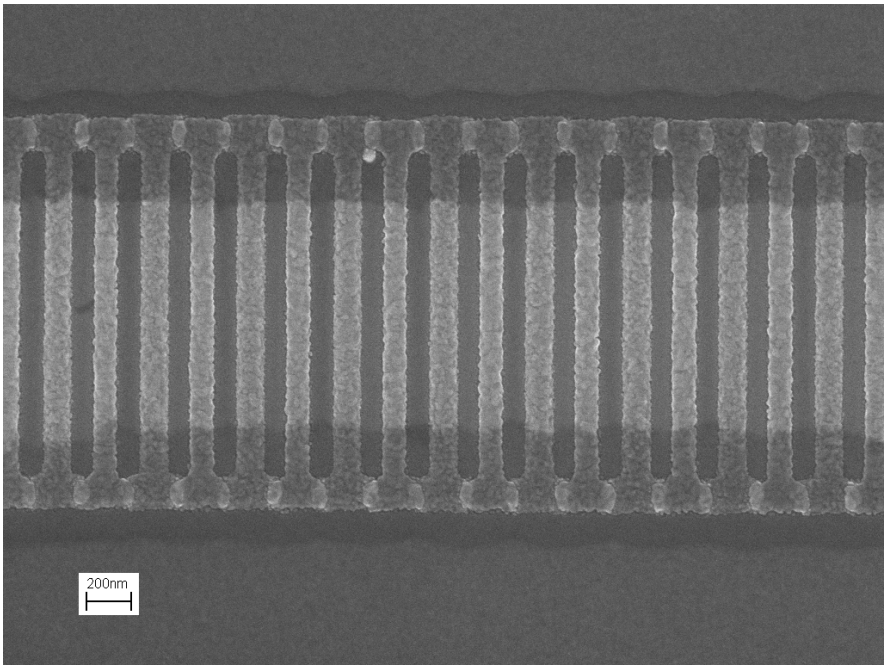


Figure 3.13: SEM picture of a section of a soliton sample. In total 256 aluminum bars are connected serially to each other via two Josephson contacts.

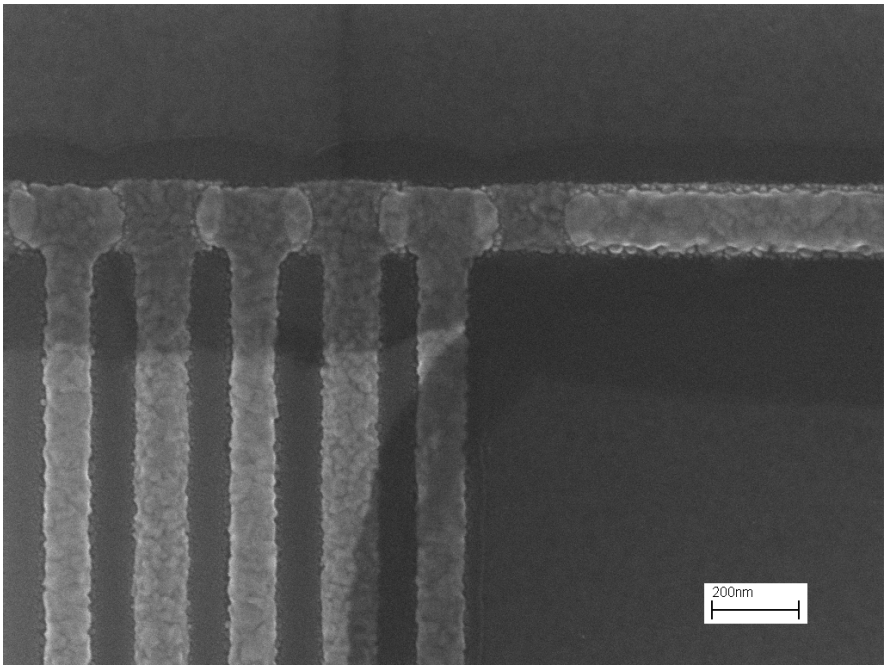


Figure 3.14: SEM picture focusing on an array of Josephson junctions of a soliton sample.

# 4 Measurement techniques

The components for our measurement setup are specialized for current-voltage (I-V) measurements at low temperatures. Throughout this work we use two-point probings to measure the I-V curves. The resistance of the load line $R_{\mathrm{load}}$ is measured in advance and subtracted later to get the I-V curve of the sample itself. At cryogenic temperatures, i.e. in the mK range, the current through a device depends nonlinearly on the voltage drop across it. As a consequence only parts of the nonlinear I-V curve of the sample itself can be explored depending on the impedance of the probing source, while other features in the I-V curve are not accessible. To recover most of the electrical properties of our devices, two main types of set-ups are used, namely a voltage bias with a low impedance source and current bias with a high impedance source.

For measuring our samples with different parameters in both normal conducting and superconducting state, a voltage resolution of 1μV and current resolution of 100 fA is required. Besides, the filtering of high frequencies plays a crucial role in improving the signal-to-noise performance. Photons with frequency up to THz should be filtered because they interfere with single charge effects via photon-assisted tunneling. Experimentally this high frequency noise is seen as an increase of the effective temperature. A good experiment requires a filtering of the environmental noise with a frequency up to 6 THz, which corresponds to a temperature of 300 K (Vion et. al., 1995).

Earlier works in our group were done in $^3$He/$^4$He top loading dilution refrigerator, while we are now working in a standard dilution refrigerator. The new instrument provides more space at the lowest temperature stage, giving us the possibility to mount 10 home made copper powder filters for the damping of high frequency noise. These high frequency filters are mounted in the low temperature part of the cryostat on purpose to keep the Nyquist noise as low as possible.

In the following, the principles of our experimental setup are described at first. Then we explain our measurement electronics with the focus on a homemade amplifier whose functionality is proved with measurement data from the experiments. Later we show in detail the filtering of high frequency noise, including the filtering principles for powder filters, the fabrication of powder filters and their functionality tested with our experiments.

## 4.1 Principles of the experimental setup

To get I-V curves at low temperatures, we use a MX400 $^3$He/$^4$He dilution refrigerator from Oxford Instruments which without any wiring has a base temperature of 9mK. With our current wiring, a base temperature below 20 mK is reached. Our samples are mounted at the bottom of the cryostat insert. A 14 Tesla magnet with an inner diameter of 14 mm is mounted in the cryostat. Since our cryostat is not a top-loading cryostat, changing of samples requires us to

warm up the mixing chamber first. Due to the good functionality of the cryostat, this can be done within one day.

Coming from a 24-pin Fischer plug mounted on top of the cryostat, 24 wire lead down to the mixing chamber through several thermal anchoring stages. Several cables are used for a resistance thermometer and a heater. 15 wires are $RC$-filtered with a $C = 1\text{nF}$ and $R$ between 8 and 15 kΩ. These filtered lines are connected to metal powder filters for further damping of higher frequency noises. In total 10 of these home-made metal filters, 5 of which are made with twisted pairs and the other 5 with single wires are implemented. The twisted pair powder filters have the advantage of reducing the common mode noise, which enhances the performance when they are used to current/voltage biasing our samples. The single wire copper powder filters are used for gate bias.

Our measurements require a current resolution of 100 fA. This is difficult to achieve directly by a very small voltage bias due to the environmental noise. Therefore specially designed voltage dividers and amplifiers are installed as a intermediate stage between the electronics and our samples. A promising amplifier design was developed in our group some years ago (Wallisser, 2002). First we divide the applied voltage by a factor of 1000, so we can work with a higher voltage with the advantage of more tolerance to the environmental noise. The voltage signal is than transferred into current signal with a factor of $10^8$V/A by implementing Burr-Brown operational amplifiers.

The wires leading into the cryostat are filtered by Π-filters mounted close to the insert and $RC$-filters and metal powder filters in the mixing chamber. In addition, the grounding is intentionally done at only one point instead of multiple ones (on purpose to keep the same potential). We use the sample holder which is mounted at low temperatures for another shield to avoid blackbody radiation from being picked up by our measurement circuit. All the measurement electronics are mounted in a rack and are only connected to the cryostat through the filtered lines. A computer using LINUX is responsible for controlling and readout of the measurement electronics via IEEE-Bus.

Temperature dependent measurement can also be done with our cryostat by using a resistor mounted close to the sample as a heater. It is connected to a current source controlled by our measurement computer. The software (PID controller) is implemented to adjust the output of the current source. The temperature is monitored by measuring the resistance of a $RuO_2$ thermometer which is mounted at the top of the sample holder.

## 4.2 Measurement electronics

As in every sensitive electrical measurement, our single charge experiments require a good signal-to-noise performance. Noise has to be reduced as much as possible in order to have a high quality experiment. However, in reality not all the noise can be eliminated. Some of them is intrinsic, e.g., Nyquist (thermal) noise, shot noise and $1/f$-noise[1]. Only the noise due

[1] Shot noise in the single charge experiments originates from the fact that the current is carried by discrete charges. $1/f$ noise is due to background charges close to our single charge devices.

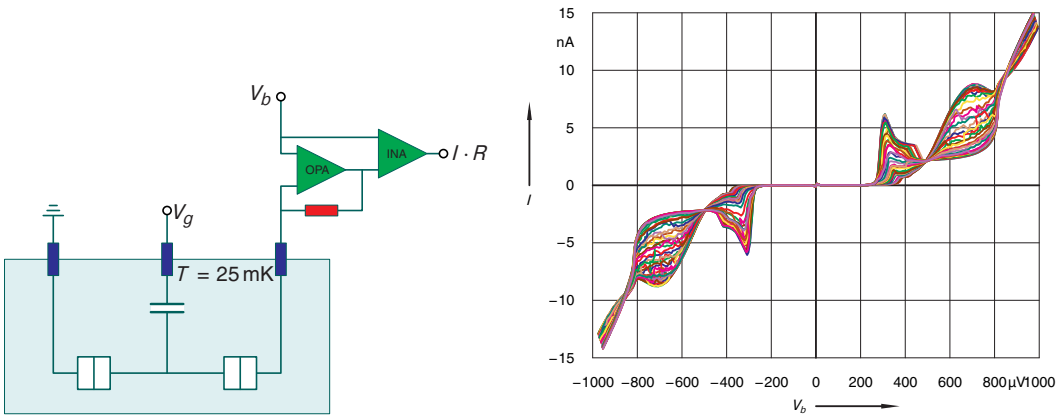


Figure 4.1: The left graph is the simplified sketch of voltage bias setup we used in the experiments. Burr-Brown operational amplifier is the essential part. A voltage bias of $V_b$ is supplied to the sample through a input pin of this amplifier while the current draws through the 100 MΩ resistor. So a trans-impedance amplification magnitude of $10^8$V/A can be achieved with this setup. Right graph shows one of our I-V curves measured in the voltage biased setup.

to non-intrinsic reasons which is often referred to as electromagnetic environmental noise can be reduced. A good measurement requires these environmental noise to be reduced below the intrinsic noise level. The main contributions to environmental noise are the following:

- 50 Hz noise and its higher harmonics,
- radio frequency noise (above 200 kHz), picked up by the wiring,
- noise generated by cable vibrations in a magnetic environment,
- noise coming from sudden switches of the electronic equipments.

Noise can be fatal for our experiments. Therefore, we try to shield it as completely as possible and use a thought-through grounding scheme. For the damping techniques, one can refer to earlier works in our group (Sypli, 1997; Wallisser, 2002).

In our experiments, both voltage and current schemes are used. Fig. 4.1 shows the voltage bias case and we can have a trans-impedance amplification as high as $10^8$V/A which gives sufficient resolution for observing most of the features in a higher voltage range, e.g., the $3e$ process and strong quasiparticle tunneling at $4\Delta$. In this case, the amplifiers and the 100 MΩ resistor are mounted in a box next to the cryostat insert. All cables are carefully shielded and all possible leaks are sealed by indium. With this setup, a resolution of 100 fA is reached which corresponds in the voltage output to 10 µV.

Fig. 4.2 shows the current bias case where we supply a current through the sample and record the voltage drop. This recovers most of the features in the low voltage range, e.g. the supercurrent and the phase diffusion branch. We use a very large resistor in series with a voltage source to represent a current source. Since the resistance is so large the current can

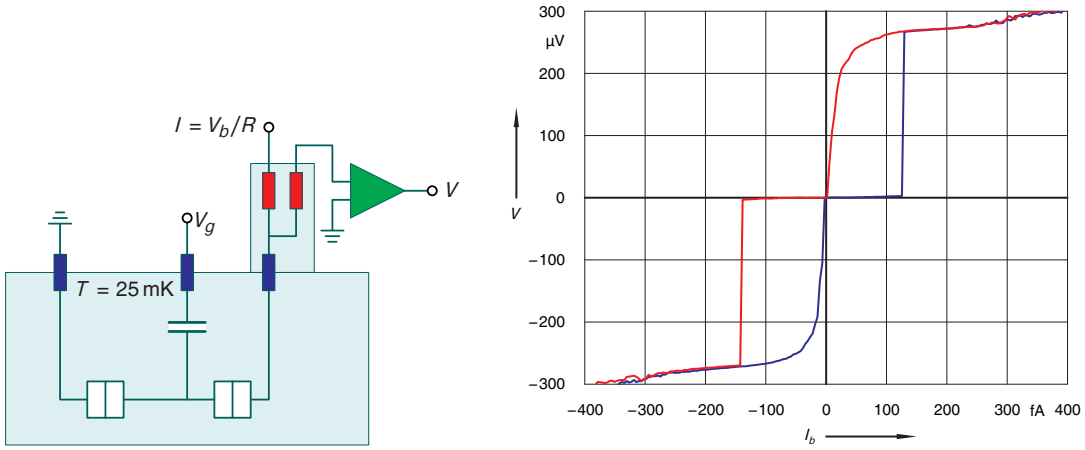


Figure 4.2: The left graph is a simplified sketch of the current bias setup we use in the experiments. A resistor with a much larger resistance compared to the sample is serially connected to it. An applied voltage drops almost completely across the resistor. The small voltage drop across our sample is read out with an instrumentational amplifier. The right graph shows one of our current biased measurements.

be considered as linearly dependent on the applied voltage, ignoring the non-linear sample impedance. As high temperature means large thermal noise (Nyquist noise), we put the resistor in the mixing chamber to minimize it. The root mean square of this noise is in the nV range according to the following formula:

$$v_n = \sqrt{4\,k_B T R \Delta f}, i_n = \sqrt{4\,k_B T \Delta f / R}. \tag{4.1}$$

The right graph of this figure shows one of our I-V curves measured by the current bias. The blue curve is scanning from negative to positive currents while the red curve is the other way around. We gained a clear view of the switching current and the re-trapping behavior.

## 4.3 Environmental noise

In the past paragraphs, we have already discussed the necessity of a good shielding against high frequency radiation. Besides a thoroughly though shield, more things have to be considered to guarantee the observation of single charge effects.

Single charge effects can be easily affected by thermal fluctuations. Tunneling currents can be activated by these noises, destroying the blockade of single charge transports. Even, a small noise signal from the warm parts of the measurement setup is already enough to smear the tunneling effect (Martinis and Nahum, 1993). Our single electron transistors have a typical charging energy of $E_c \approx 1 k_B \cdot \mathrm{K}$. It is therefore clear that thermal fluctuations corresponding to 1 K are not allowed and even the blackbody radiation from the 1 K stage has to be filtered. Translating this into the frequency of photons, a noise with frequency $f \geq (k_B \cdot 1\mathrm{K})/h \approx$

20 GHz is enough to remove the charge blockade. So the tunneling of charges will be affected by the high frequency electric noise along the wiring just as by the thermal noise. All the wires connecting to the sample should be filtered, so that the voltage fluctuations from the warm parts of the wiring will not reach the sample. Several stages of thermal anchoring will not suffice. Thermal anchors, which are done by making a good thermal contact to the cold parts of the cryostat, will damp the phonons carried by the crystal lattices, but not the phonons carried directly by the electrons (Vion et. al., 1995). The samples should also be put in a shielded box to avoid any unwanted direct radiation, e. g. 4 K photons from the helium bath surrounding the mixing chamber.

It has been calculated by Vion et al. (1995) that for a transistor with a typical charging energy of $E_c = 1\, k_B \cdot \mathrm{K}$ the damping should be better than 100 dB in the bandwidth between 10 GHz and 6 THz, corresponding to a noise source with a temperature between 1 K and 300 K. The filters should be mounted at the coldest stage of the experimental setup to damp the noise.

### 4.3.1 Filtering concept

Several types of filters are suitable for the damping of high frequencies at low temperatures. The most commonly used ones are *RLC* on chip, lossy coaxial cable and metal powder filters. Each has its own advantages and disadvantages. Depending on the application, one of them or a combination of several ones can be chosen to meet different requirements.

One method for filtering the high frequency noise in the range from 20 GHz to 6 THz with a damping factor above 200 dB was found by Zorin (1995) and Glattli et. al. (1997). The authors recommend lossy coaxial cables which work as a distributed *RC* low pass filter. For high losses, inner and outer conductor are made from highly resistive materials. In addition the resistance displays a $\sqrt{\omega}$-dependence at high frequencies due to the skin effect. The space between the inner and outer conductor, which is carefully filled with a dielectric, must be small to avoid the propagation of high frequency TM and TE modes. Glattli et al. (1997) use their home-made coaxial cables while Zorin uses commercial Thermocoax cables from Philips. It has been calculated by Zorin that one meter of these wires will already offer enough damping for high frequencies if we mount the upper end at around 10 K and the last 30 cm of the wires directly at the mixing chamber. Glattli et al. measured an effective temperature of 40 mK after using their home-made coaxial cables while no effective temperature under 100 mK was observed without any coaxial cable filtering.

Another method for high frequency filtering is the use of copper powder filters (Martinis et. al., 1987). It contains several tens of centimeters of wires wound up to form a spiral and buried in metal powders with a particle size of around 30 µm. The damping of high frequency noises in this case can be described by the telegraph equation as for the coaxial cables. For earlier experiments in our group this kind of filters were not installed due to the restricted space in top-loading cryostat. The relatively large mass in the mixing chamber would also have resulted in more difficulties for the cooling.

Fukushima and his coworkers (1997) investigated the damping properties of cooper powder filters, including cooper powder filters and stainless steel powder filters, and commercial Thermocoax cables at different temperatures up to 20 GHz. They reported that the stainless

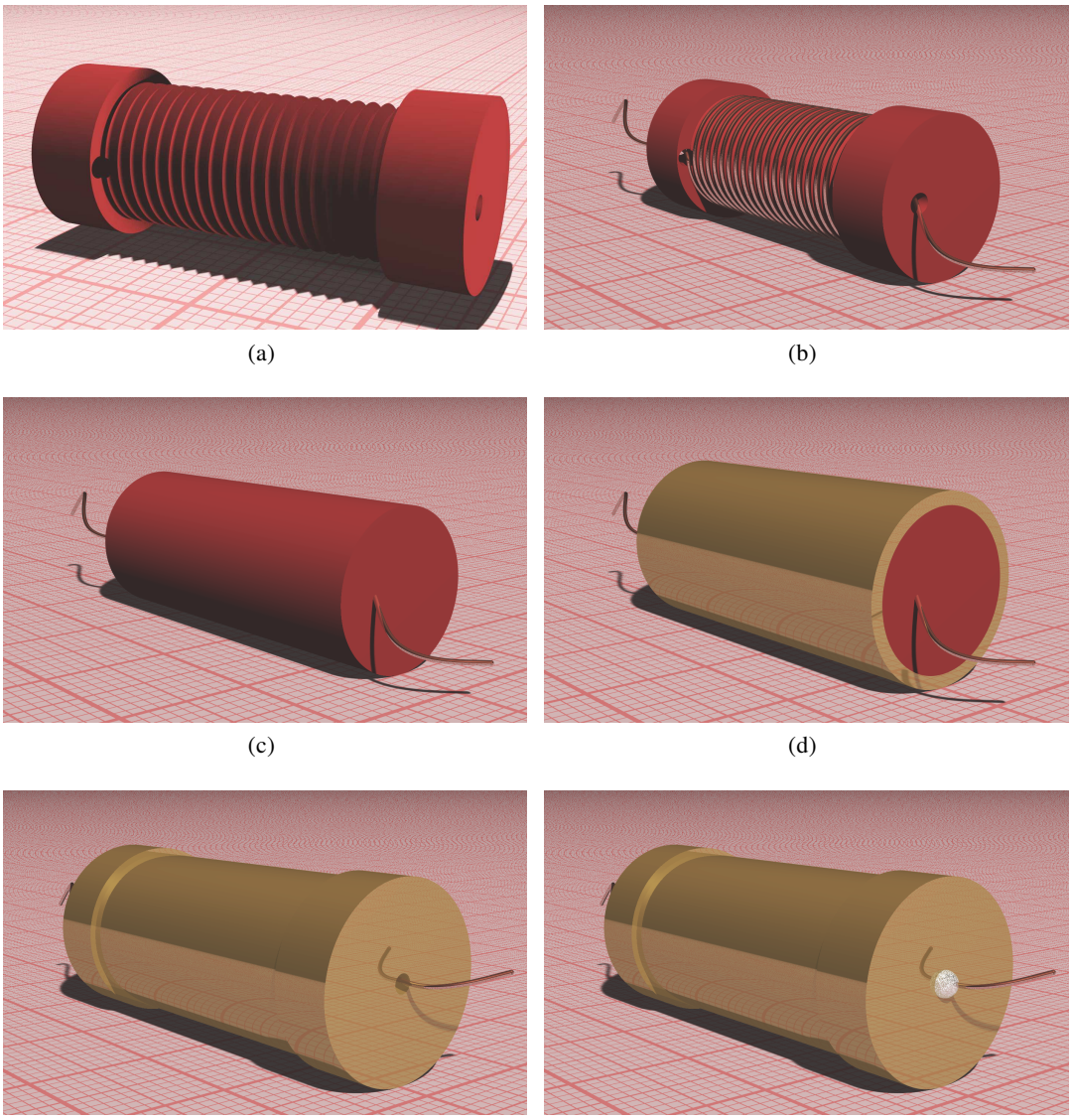

(a) (b) (c) (d) (e) (f)

Figure 4.3: Construction of filters: (a) the fabrication of the rod; (b) wiring cables around the rod; (c) cover with more mixture; (d) coated with a brass tube; (e) close both ends with a brass hat; (f) use a droplet of silver paste to close the gap.

steel powder filter with a particle size of 30 µm has the best performance at all temperatures. But since their damping factor is not really high and barely goes above 80 dB, it is dangerous to rely on this conclusion for the construction of the filtering stage. Bladh et al. (2003) compared different types of $RCL$ filters, coaxial cable filters and metal powder filters and they recommended that a broadband filtering of dc lines can be achieved by combining filters like

$RC$, $RCL$, or $LC$ with Thermocoax or powder filters to cover a frequency range as wide as possible. In our case, a combination of $RC$ and copper/silver powder filters is used.

### 4.3.2 Metal powder filter fabrication

Metallic powder filters have the lowest DC resistance of all high frequency filters discussed so far. We have chosen this concept for our setup because it gives us the highest flexibility for different types of experiments. The cooling power of our fridge is relatively large (400 µW at 100 mK) so that the mass which has to be cooled does not prohibit the application of several metal powder filters in parallel.

The grains in a metal powder filter lead to damping of high frequency signals running along the inner conducting wire. This is due to a capacitive coupling between grains and the wire which yield to displacement currents running due to skin effect in a thin surface layer of the grain. This displacement current is subjected to dissipation which grows as the surface layer gets thinner with increasing frequency. Similar to a lossy coaxial cable, the damping thus scales as $\sqrt{\omega}$. The transmission line picture is well suited for describing the powder filters, just as shown in Fig. 2.7.

Since their invention, copper powder filters have gained a lot of popularity among the single charge effect community. Many proposals are raised by different groups, according to their type of cryostat and experiment. We are heading for the single charge effect in the normal- and superconducting regime with an Oxford MX400 cryostat. This requires 15 wires leading to the mixing chamber with all of them filtered by metal powder filters. Although the space available for mounting the metal powder filters is not really small, such a big amount of filters still constrains the size of each individual one. The efficency of powder filters depends on the length of wire which is surrounded by the metal powder. Thus one should try to wrap as long wires as possible in a limited room while avoiding direct coupling between different parts of the wires.

For the fabrication of our metal powder filters we use the epoxy STYCAST 1266 and a copper and silver alloy powder mixture with mass ratio of 28:72 copper and silver. The maximum powder grain size is 5 µm, providing as much surface area as possible. Epoxy and powder were mixed with a volume ratio of 1:1 to guarantee a high concentration of metal powder. Afterwards this mixture is put into vacuum for de-airing. This procedure removes little bubbles of air, to avoid degasing in the cryostat during operation. Then the mixture is put into a plastic tube with an inner diameter of 8 mm to form a rod. After hardening of the epoxy and removal of the tube, the rod is cut into small pieces of 5 cm length each and each piece is threaded as shown in Fig. 4.3a. A varnish-coated copper wire with a diameter of 0.1 mm is wound along the thread tightly. The wire ends through small holes drilled on both ends of the rod, see Fig. 4.3b. The double wire version to minimize magnetic pickup noise is also prepared this way. The rod is then put into a brass tube and extra epoxy/metal powder mixture is injected to fill the gaps inside the tube, as we can see in Fig. 4.3d. An inside look at the rod is shown in Fig. 4.3c. Then we cover both ends of the tube with a droplet of silver paste to avoid cross talking between the ends. Because of the good controllability of the construction, a total length of 150 cm of wire can be reached, leading to a good skin effect damping of high frequency noise.

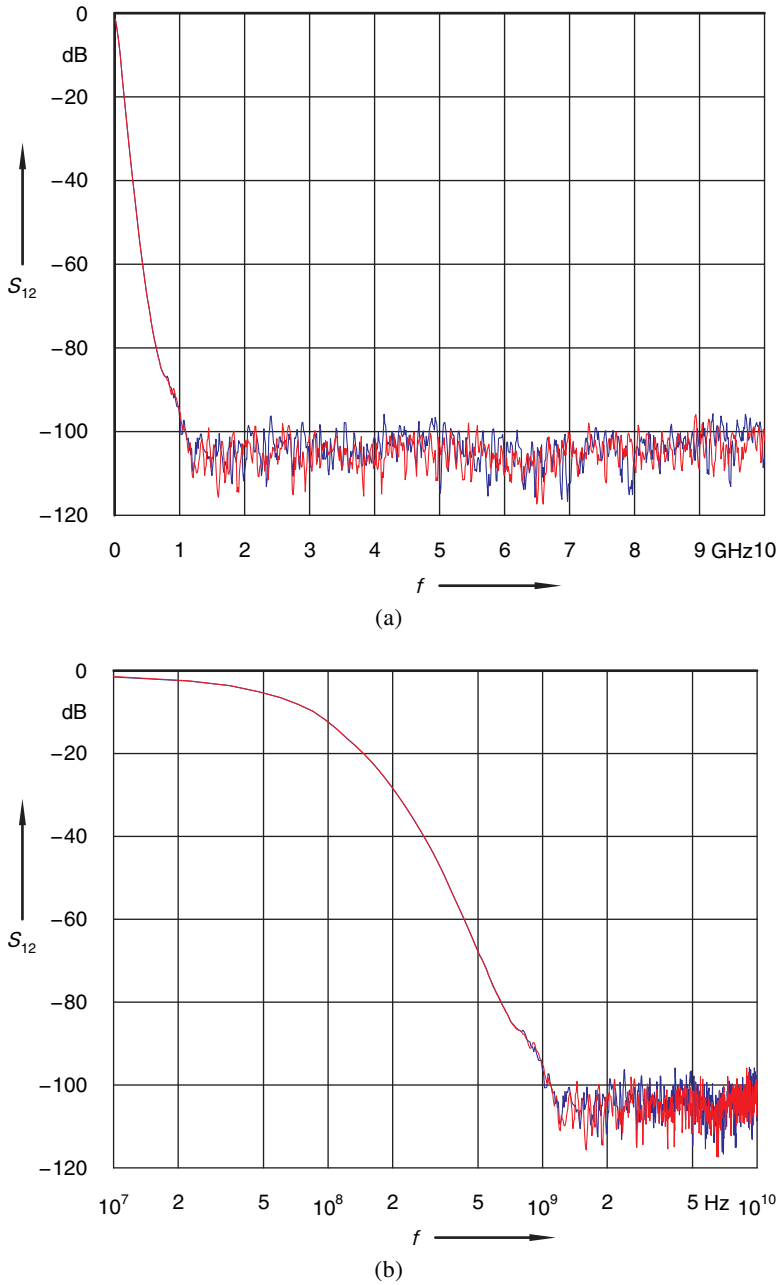


Figure 4.4: The damping of the filters measured at 4.2 K at IMS: (a) linear scale; (b) logarithmic scale. For the frequency range above 10 GHz, damping becomes higher than the noise level of our measurement device. Therefore a real damping factor cannot be determined for these frequencies.

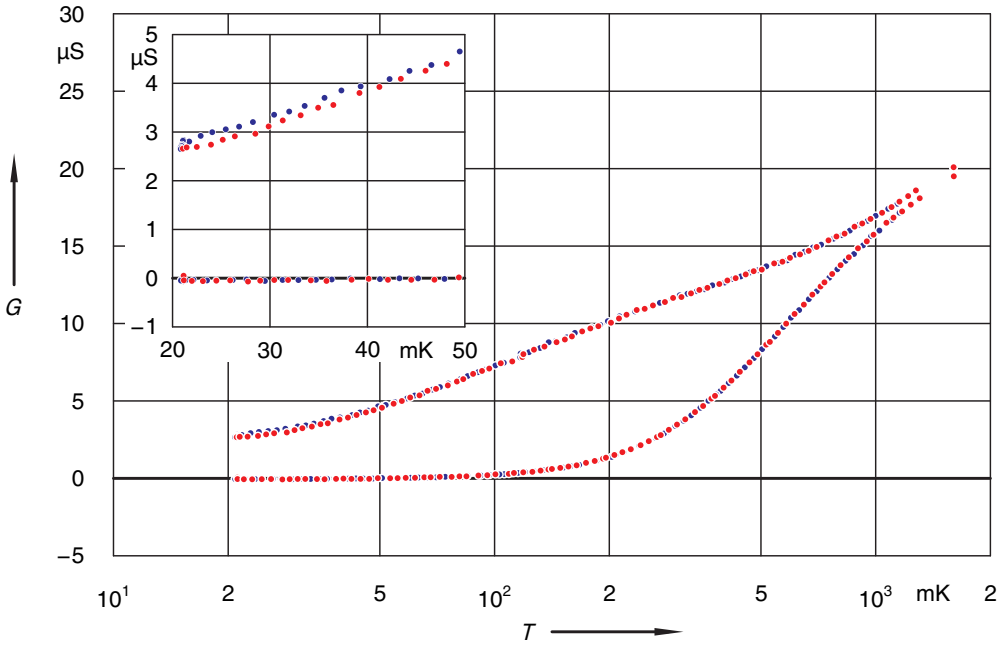


Figure 4.5: Conductance measurement of a normal conducting SET at a small bias voltage in the temperature range from 20 mK to 2 K. The conductance modulates with the gate voltage and for a given temperature is bound by $G_{\min}$ and $G_{\max}$. $G_{\min}$ and $G_{\max}$ are measured with increasing temperature (red) and decreasing temperature (blue) separately. The inset shows the data on an enlarged temperature scale. One sees a slight discrepancy of red and blue points for the maximal conductance branch. This is due to the fact that a certain relaxation time is needed for the transistor to reach thermal equilibrium. The effective temperature for blue points is always a bit higher than the effective temperature for red points at the same environment temperature, thus leading to a more pronounce transport of charges.

### 4.3.3 Filtering effectiveness

An experimental study of the metal powder filters was done by our colleagues from Institut für Mikro- und Nanoelektronische Systeme (IMS), KIT. A metal powder filter was put into a well shielded copper box with both ends connected to SMA collectors. With the help of a network analyzer (Agilent Technologies E8361A), the damping of the filter in a frequency range up to 10 GHz was measured both at room temperature and 4.2 K. As expected, a good damping was observed at high frequencies due to the skin effect of the metal powder. Fig. 4.4 shows our measured attenuation at 4.2 K.

The damping in the frequency range from 10 GHz to 6 THz at low temperatures is very important, but cannot be measured directly using the network analyzer. Wallisser et. al. (2002) have described that the conductance measurement of the single electron transistor is actually a good method to study the filtering. We know that the effective temperature of the electrons depends strongly on the filtering of environmental noise. If any high frequency noise is present,

one has no chance to get a sufficiently low effective temperature of the electrons. The linear response conductance is a periodic function of the gate voltage (see Sec. 2.1). It is bound by a minimal conductance $G_{\min}$ at $V_g = ne/C_g$ and a maximal conductance $G_{\max}$ at $V_g = (n+0.5)e/C_g$. $G_{\min}$ and $G_{\max}$ are shown as a function of temperature in Fig. 4.5. The behavior is governed by the sequential tunneling model (see Sec. 2.1.1), but with strong co-tunneling contributions (see Sec. 2.1.2). The latter is a very complex process and no explicit formula can be found to describe it. As shown by Wallisser et. al. (2002), the path-integral Monte Carlo calculations can reproduce his experimental observations. For very small bias voltages at low temperatures, the maximum conductance $G_{max}$ should fall off proportional to $g\ln(\beta E_c/\pi)$.

Fig. 4.5 shows the data of the minimum and maximum conductance depending on the temperature. One sees that maximum conductance of the SET scales logarithmically with the temperature, which fits well the formula $g\ln(\beta E_c/\pi)$ even down to around 50 mK. As the temperature goes down further, $G_{max}$ still decreases. This observation is a clear evidence that our metal powder filters do work, and we can reach the effective temperature required for single charge experiments (Wallisser et. al., 2002).

# 5 Results

In this chapter the main results of measurements on single Cooper pair transistors are presented. All the measurements were done in our $^3$He/$^4$He dilution refrigerator at IFP, FZK.

Single charge transistor has been studied extensively (Ingold and Nazarov, 1992; Joyez, 1995; Tuominen et. al., 1993; Amar et. al., 1994; Lu et. al., 1996; Joyez et. al., 1994; Geerligs et. al., 1990; Aumentado et. al., 2004). Due to the realization of charge qubits based on single Cooper pair boxes, more efforts have been directed to the research on single Cooper pair transistors in order to understand the basic physical properties of this type of devices. Theoretically, it is expected that the charge transport at small bias on the single Cooper pair transistors is $2e$-periodic in the gate charge. But many experiments observed $e$-periodic behavior which has been attributed to the poor filtering of the measurement setup. But even with good filtering, many experiments still yielded $e$-periodic behavior. Today it is common belief that all experimental results are plagued by the presence of spurious quasiparticles which cannot be explained by the equilibrium quasiparticle poisoning model presented in Sec. 2.3.3. But the origin of quasiparticles is unclear up to day.

We first studied the charge transport at higher bias voltages which is more complicated compared with the charge transport in the single electron transistors. In the single electron transistor, the current is mainly caused by sequential tunneling of electrons while in the single Cooper pair transistors, different mechanisms get involved. The dynamic processes include the Josephson effect and quasiparticle tunneling. Both contribute to the current flow through the device.

The first part of this section describes the analysis of the normal conducting and superconducting measurements for obtaining the device parameters such as the charging energy $E_c$ and the normal-state conductance $g$ which is according to Eq. 2.3 related to the Josephson energy $E_j$ by $E_j = \Delta hg/8e^2$. Observations at finite voltage bias are looked into carefully in the next part. Finally results on the switching current are presented. Some $2e$-periodic as well as $e$-periodic data are given with an effort to explain the reason for the different behavior.

## 5.1 Parameter characterization

### 5.1.1 Analysis of the normal conducting IV curves

Normal conducting IV curves of the samples are measured for the purpose of parameter characterization. The sequential tunneling model predicts that the high-voltage part of the IV curves approaches asymptotically a straight line. The asymptotes at positive and negative voltages are separated by twice the threshold voltage $V_{th}$. For a SET in a low-ohmic environment, this threshold voltage is connected to the charging energy by

$$V_{\mathrm{th}} = 2E_c/e. \tag{5.1}$$

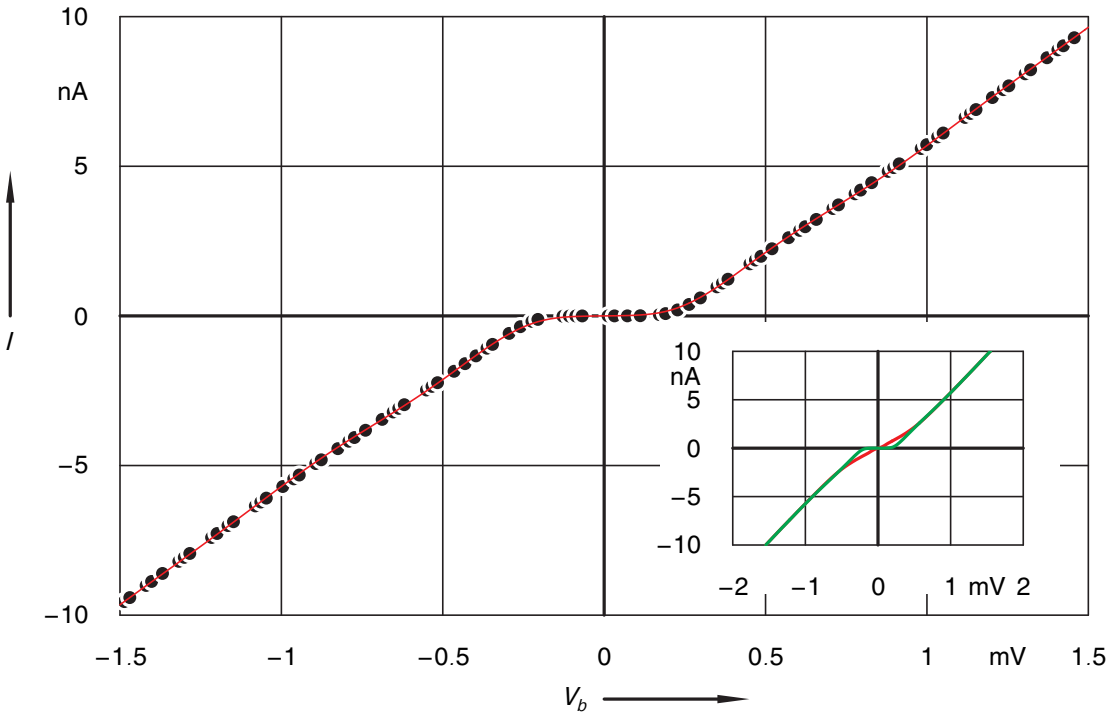


Figure 5.1: IV curve of sample 81III in the normal conducting state ($T$ = 25mK, $B$ = 1T) used for parameter characterization. The dotted line is the measured curve and red solid line is the fitted curve. Inset: Red one shows the IV curve for the same sample where the Coulomb blockade is lifted and green one is with the full blockade.

The slope of the asymptotes equals the serial conductance of the two tunneling contacts.

In our SET layout, only the serial conductance can be measured. An important parameter called coupling strength and defined as

$$\alpha = \frac{G_{\|}}{G_0}, \tag{5.2}$$

is inaccessible. Here $G_{\|} = G_1 + G_2$, the determination of which requires the knowledge of the conductances of individual contacts, while in our layout only the serial conductance $G_s = G_1 G_2/(G_1 + G_2)$ can be determined. Wallisser (2002) remedies this deficiency by defining a layout with four tunnel junctions connected to the island through individual leads. By measuring conductances along different routes and with a little help of algebra the individual tunnel conductances can be evaluated. The device can still be used as transistor by connecting two contacts in parallel to source and drain, respectively. However, we didn't try this layout for this work because of its higher complexity. Therefore in this work the coupling strength can not be directly measured.

It has also been pointed out by Schäfer et. al. (2007) that the slopes of the IV characteristic at large positive and negative bias voltage approach a constant value rather slowly for several

reasons, which limits the determination of the sequential conductance to an accuracy of about 5%. For the discussion of our transistor properties, however, this accuracy is sufficient. Fig. 5.1 is an example for the fitting of the normal conducting IV curve for sample 81III within the sequential tunneling model. It yields a charging energy $E_c = 150\mu eV$ and a serial conductance $G = 8.02\mu S$.

The IV curves of the SET is modulated periodically by the gate voltage $V_g$ which shift the island electrostatic energy by an amount $\Delta E = (2E_c/e)C_g V_g$, see Sec. 2.1. The inset of Fig. 5.1 shows the IV dependence for sample 81III for two different gate voltages. At the so-called linear response regime where the bias voltage is very small, the red curve has a full lifted Coulomb blockade and green one has a full Coulomb blockade. This small voltage bias regime is of special interest due to the minimized self-heating of the transistors (Schäfer et. al., 2007). At elevated temperatures the conductance does not depend on the gate voltages $V_g$. Still, it is renormalized due to the Coulomb blockade in the linear-response regime. The conductance can be described by the formula

$$\frac{g}{g_0} = 1 - \frac{E_c}{3k_b T} + \frac{c}{T^2}. \tag{5.3}$$

It has been reported by Wallisser (2002) that the charging energy obtained in this way is much more accurate than the one achieved by the sequential tunneling model. In our dilution refrigerator, we do not have easy access to the required temperature range. A good alternative is to judge the charging energy directly from the superconducting measurements, see Sec. 5.1.2. Since we are more interested in the superconducting properties of our transistors, it makes more sense to get the charging energy directly from superconducting measurements.

### 5.1.2 Superconducting measurement analysis

The IV characteristics of the transistors in the superconducting state can be measured simply by removing the applied magnetic field which is used for the suppression of the superconductivity, see Sec. 2.3. Typical voltage bias IV measurements are shown in Fig. 5.2. The inset of Fig. 5.2 shows the supercurrent branch close to zero bias, see Sec. 2.3.2. At bias voltages $400\mu V < |V| < 800\mu V$, the current is mostly caused by the Josephson quasiparticle cycle, which leads to a relatively large current, in comparison with the features below $|V| < 400\mu V$ (These features can not be resolved at the current scale of Fig. 5.2). At $|V| > 800\mu V$, quasiparticle tunneling leads to the main contribution of the current and the device behaves similarly to its normal conducting counterpart.

As explained in Sec. 2.3.1.2 and Sec. 2.3.1.5, the superconducting sub-gap features give us several possibilities for the characterization of the sample parameters. [1]

Our samples spread over a wide parameter range. Some samples have more transparent barriers which means a higher coupling to the leads. Voltage biased measurements give pronounced

[1] The charging energy determined from superconducting measurements in such a manner, $E_c^s$, differ from the charging energy determined in the normal conducting state via procedures described in Sec. 5.1.1, $E_c^n$, due to virtual electron-hole excitations. Using lowest order perturbation theory, the following relation between the two charging

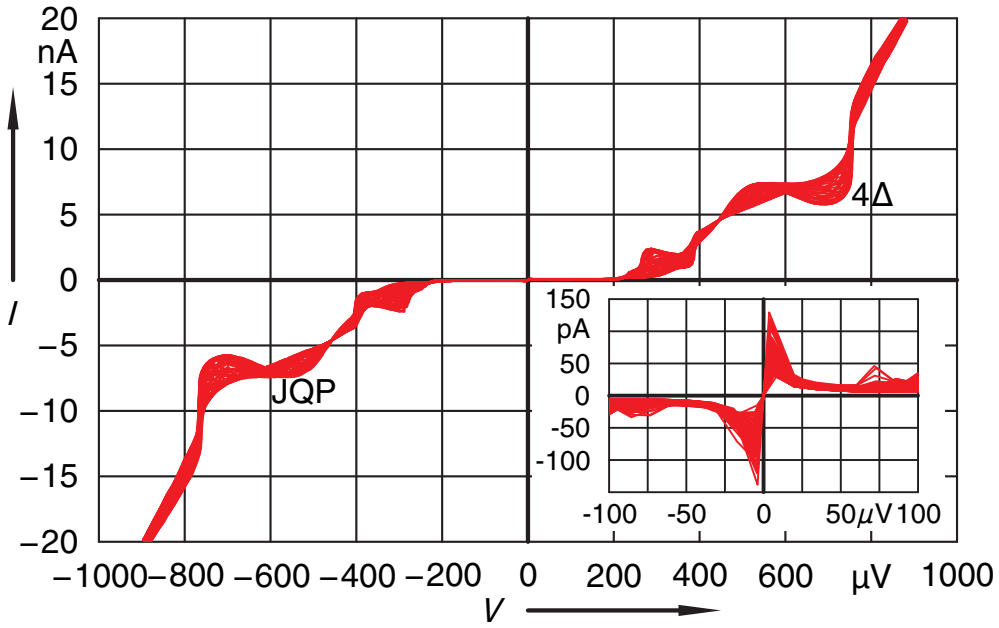


Figure 5.2: I-V measurement using the voltage bias on sample IX: Curves at different gate voltage spanning the period in $2e/C_g$ are superimposed. The Josephson quasiparticle (JQP) peaks are marked , as well as the $4\Delta$ point. The inset shows the enlarged region around zero bias where the supercurrent branch can be clearly visible. The nominal temperature of this measurement is $T = 25$mK.

resonant Cooper pair tunneling peaks, especially for the third order resonant peak (marked with red lines in Fig. 5.3). For some of the measurements, even the fifth order resonance peak can be observed clearly. Making a contour plot of current as a function of gate voltage $V_g$ and bias voltage $V$ gives clear lines due to these resonances. As has been shown in Fig. 2.13, the two adjacent third order Cooper pair tunneling lines cross each other at a bias voltage $V$ close to $4E_c/3e$ and the two adjacent fifth order Cooper pair tunneling lines cross each other at a bias voltage $V$ close to $4E_c/5e$. Taking these points for the determination of the charging energy $E_c$

energies can be achieved (Joyez et. al., 1997; Bouchiat, 1997; Wallisser, 2002)

$$\frac{E_c^s}{E_c^n} = 1 - \frac{\alpha}{\pi^2}\Gamma(\frac{E_c}{\Delta}), \tag{5.4}$$

where

$$\Gamma(x) = x\int_0^\infty u^2 K_1^2(u)\exp(-xu)du \tag{5.5}$$

and $K_1$ is the modified Bessel function of second kind and first order. $\Delta$ is the superconducting energy for aluminum which is around 200μeV and $\alpha$ is the coupling strength defined in Eq. 5.2. $E_c^n$ can be as much as 50% larger than $E_c^s$ for large couplings (which implies large Josephson energies). In our work, we focus ourselves on the superconducting properties which is directly linked to the superconducting charging energy $E_c^s$. From here on, all the $E_c$ presented are $E_c^s$.

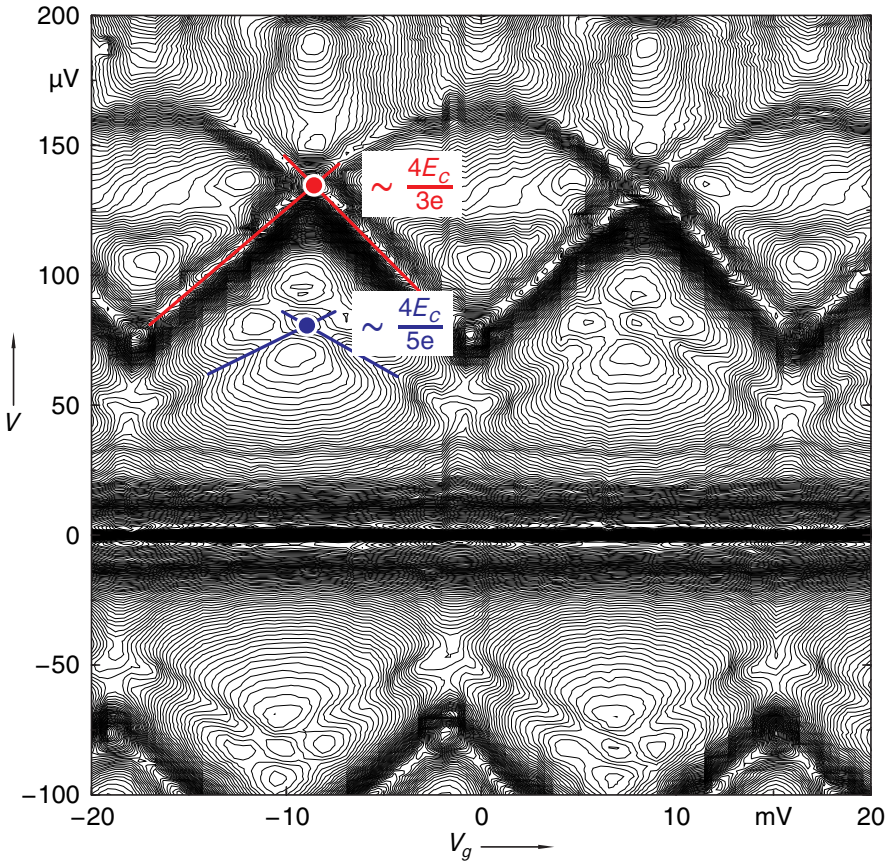


Figure 5.3: Contour plot of the current through the transistor at $T = 25$mK in the superconducting state as a function of the bias voltage $V$ and gate voltage $V_g$ for sample 94III. Different curves in this contour plot represent different constant current values with two adjacent currents differ by 3.2%. The largest current peaks have a magnitude of around 200pA at the bias voltage of $V = 200\mu$V. Resonant Cooper pair tunneling curves are used for obtaining the charging energy $E_c$. Red lines mark third order resonance in one period which crosses at around $4E_c/3$e and blue lines mark fifth order resonance in the same period which crosses at around $4E_c/5$e. Detailed current values are shown in Fig. 5.31.

gives us an uncertainty of only a few percent (Joyez, 1995), which is sufficient for the discussion of physical properties in the rest of the work. Some other samples have thicker junction barriers and the resonant Cooper pair tunneling peaks are not any longer pronounced enough for a precise determination of the charge energy. However, the current peaks induced by the JQP cycle and DJQP cycle (see Sec. 2.3.1.2 and Sec. 2.3.1.3) yields quite sufficient resolution for the determination of the charging energy $E_c$.

Fig. 5.3 shows the contour plot of current in the plane of bias voltage $V$ and gate voltage $V_g$. All the structures in this figure are e-periodic, meaning both even and odd parities have nearly

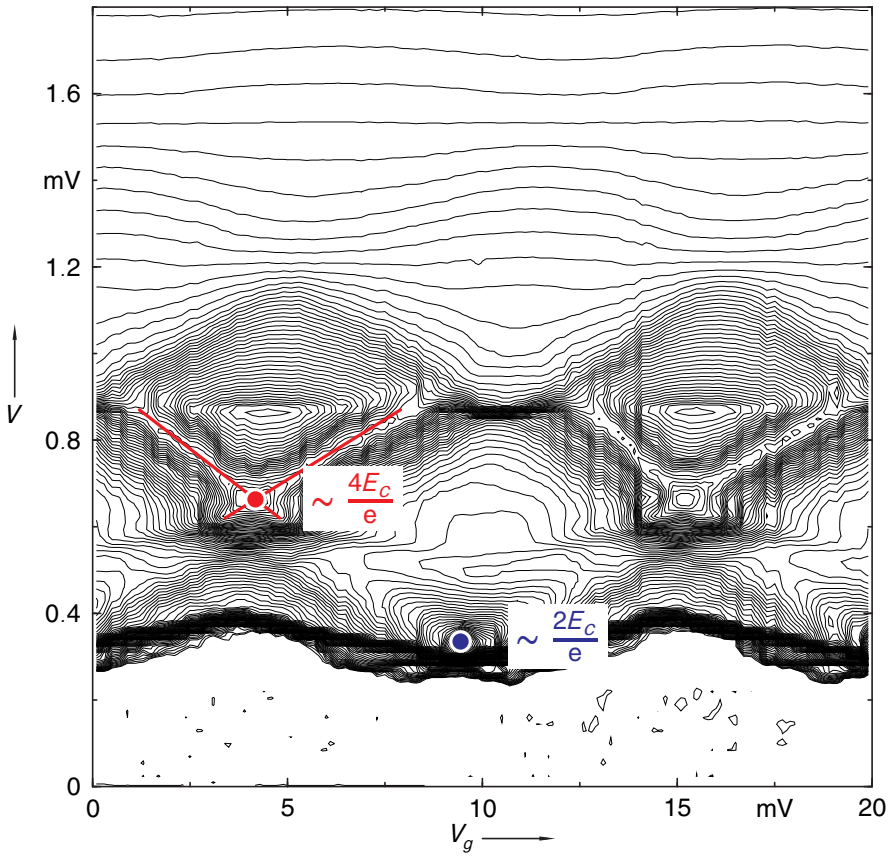


Figure 5.4: Contour plot of the current through the transistor at $T = 25$mK in the superconducting state as a function of the bias voltage $V$ and gate voltage $V_g$ for sample 81III. Current peaks due to Josephson quasiparticle cycles are used for obtaining the charging energy $E_c$. Red lines mark two adjacent quasiparticle cycle lines in one period which crosses at around $4E_c/e$ and blue dot marks the DJQP cycle which happens $2E_c/e$. Detailed current values are shown in Fig. 5.17.

equal weight for this sample. The current peaks can be grouped into lines with clearly different slopes. These lines are related to different order RCPT events. Red lines mark two adjacent third order RCPT features. They cross each other at the bias voltage $V = 133\mu$V. Using the formula

$$V = \frac{4E_c}{3e} = 133\mu\text{V}, \tag{5.6}$$

we get the charging energy $E_c = 100\mu$eV. Blue lines mark two adjacent fifth order RCPT features. They cross each other at bias voltage $V = 82\mu$V. Using the formula for fifth order

$$V = \frac{4E_c}{5e} = 82\mu\text{V}, \tag{5.7}$$

we have a charging energy $E_c = 103\mu$eV, which is consistent with the third order result.

| Sample | $R_N$ kΩ | $C_\Sigma$ fF | Δ μeV | $E_j$ μeV | $E_c$ μeV | $I_0$ nA | $E_c/E_j$ | traps |
|---|---|---|---|---|---|---|---|---|
| 70I | 37.3 | 0.47 | 201 | 34.8 | 169 | 16.9 | 4.86 | Cu/Au |
| 70Ib | 34.0 | 0.52 | 205 | 38.9 | 155 | 18.9 | 3.98 | Cu/Au |
| 73II | 10.5* | 1.11 | 204 | 125 | 72 | 61 | 0.57 | Cu/Au |
| 81II | 148.4 | 0.46 | 215 | 9.34 | 174 | 4.55 | 18.6 | Cu/Au |
| 81III | 124.8 | 0.51 | 215 | 10.9 | 164 | 5.33 | 14.3 | Cu/Au |
| 82IIIa | 30.6 | 0.54 | 200 | 42.2 | 125 | 20.5 | 2.96 | Cu/Au |
| 82IVa | 32.5 | 0.55 | 200* | 39.7 | 135 | 19.3 | 3.4 | Cu/Au |
| 82IVb | 25.3 | 0.69 | 200 | 49.6 | 114 | 24.8 | 2.27 | Cu/Au |
| 94I | 24.6 | 0.53 | 190 | 49.8 | 150 | 24.3 | 3.01 | Pd/Au |
| 94III | 22.6 | 0.58 | 188 | 53.7 | 103 | 26.1 | 2.59 | Pd/Au |

Table 5.1: Collection of the important parameters of the measured samples.

Fig. 5.4 is the contour plot of current as a function of the bias voltage $V$ and gate voltage $V_g$ for sample 81III. We can see current peaks falling on lines in the $V/V_g$-plane in the bias voltage range from 0.6mV to 0.84mV. These peaks are due to the Josephson quasiparticle cycle. Red lines mark two adjacent Josephson quasiparticle cycle lines which cross each other at around 0.66mV. From our discussion in Sec. 2.3.1.2, we easily have $4E_c = 660$μeV, yielding a charging energy of 165μeV. This is quite consistent with the DJQP point which is marked in Blue in Fig. 5.4, which happens at a bias voltage of $2E_c/e$ =328μV, giving a charging energy 164μeV.

The superconducting energy gap Δ can also be determined from the superconducting IV measurements. In Fig. 5.4, above the voltage 0.86mV, quasiparticle tunneling leads to the main current contribution. This means the bias voltage $V$ is large enough to overcome the superconducting energy gaps of both left and right junctions. So from this condition, we have $4\Delta = 860$μeV, leading to an energy gap $\Delta = 215$μeV. There might be a slight different height of the superconducting energy gaps for the electrodes which are formed during different evaporation steps. This can only be done by studying the superconducting energy gap of separately fabricated electrodes.

### 5.1.3 Sample parameters

The main characteristics of the samples are given in table 5.1. All the charging energies $E_c$ presented in this table are obtained from the superconducting measurements by studying the resonant Cooper pair tunneling peaks and Josephson quasiparticle cycle peaks. The superconducting $E_c$ applies more directly for the studying of our devices in their superconducting states. The normal state serial resistance $R_N$ is obtained by fitting the IV characteristics of the normal state measurements with the sequential tunneling model. Since our sample layout doesn't allow for the individual resistance measurement of each junction, we assumed both junctions in the transistors to be identical. The critical current $I_0$ of each junction and the Josephson coupling energy $E_j$ of each junction are calculated by using the Ambegaokar-Baratoff formula

$I_0 = \pi\Delta/2eR_N$ and $E_j = g_N\Delta/8$ where $g_N = G_N/G_0$. The superconducting energy gap $\Delta$ is directly obtained from the $4\Delta$ positions around 800μeV where quasiparticle tunneling starts to dominate.

All the samples we measured have normal metal leads fabricated close to the tunnel junctions to prevent quasiparticle poisoning, see Fig. 3.9. The first few quasiparticle traps are made from Au/Cu alloy. The later ones are fabricated with Au/Pd alloy to increase the efficiency of quasiparticle damping.

The normal conducting IV characteristics are measured for most samples except for sample 73II. So the normal resistance $R_N$ for 73II is obtained by calculating the slope of the superconducting IV curve when $V > 4\Delta/e$ where the effect of the superconducting energy gap is overcome and the current is caused by quasiparticle tunneling. For sample 82IVa, we only measured the current in the bias range from -250μV to 250μV. So we can only assume a superconducting energy gap $\Delta$ =200μeV which is the energy gap for the other two samples on the same chip.

## 5.2 Voltage bias measurements

### 5.2.1 Results

In this section we present our experimental data obtained with the voltage bias setup. A typical IV measurement as shown in Fig. 5.5 and Fig. 5.6 comprises 300 IV curves, taking at different values at fixed gate voltages. Each IV curve is recorded in five minutes by setting $V$ to 300 different values and measuring the resulting current with our transimpedance amplifier (see Chap. 4). The output voltage of this analog amplifier is recorded with an Agilent 3458A digital multimeter with an aperture of 100μs. Other measurements presented in this section are obtained in a similar way.

In all cases, we present the same data in two plots side by side given a 3D perspective on one hand and a 2D false color projection on the other hand. The color coding gets apparent from the 3D plot. In many cases, tiny features in the sub-gap region (which we code by a grayish color) are difficult to resolve by pure color coding. We therefore apply a pseudo illumination technique to the 3D data in the following way. The gradient of the 3D plane is calculated and the scalar product with a constant vector is calculated and the color saturation is adjusted according to the resulting value. This method turns out to be very efficient to make even the slightest current feature clearly visible.

Most of the figures show a well-known phenomena. From time to time, the periodicity in $V_g$ is disturbed by sudden jumps in phase. They result from the rearrangement of background charges coupling capacitively to the transistor island. These background charges thus give a contribution to $n_0$, offsetting it slightly with respect to the simple formula in App. A. Amazingly, we find in our experiments most of the time small contributions. In case of a jump in $n_0$, we regularly observed a tendency to jump back to the original location. In this respect, sample 81II is a rare exception.

All the measurements are done at the base temperature of our cryostat $T \sim$ 25mK. Measurement data on ten samples are presented which were taken in a time span of roughly one

year. Our samples have charging energies varying between 72μeV and 174μeV. The Josephson coupling energies span a broader range between 9μeV and 54μeV. The superconducting gaps are all close to 200μeV. In the voltage bias setup, all the sub-gap features are e-periodic. Only the superbranch of sample 94I show clear signs of 2e-periodicity.

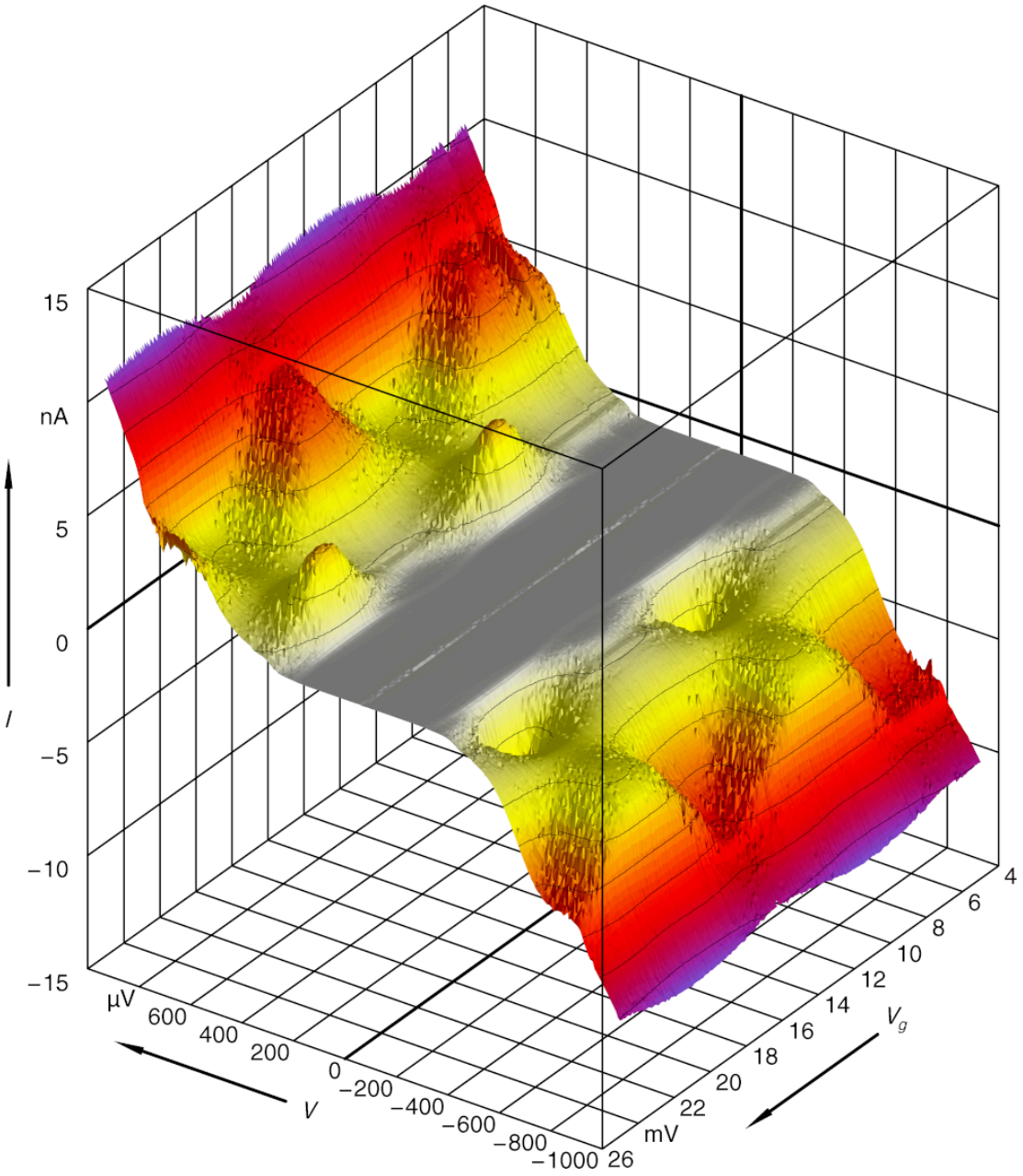


Figure 5.5: Another 3D plot of the measured current $I$ as a function of bias voltage $V$ and gate voltage $V_g$ for sample 70I.

Fig. 5.5 and Fig. 5.6 show our measurement data for sample 70I. This is one of the first samples we fabricated and the measurements were done during our measurement setup optimization process. We cannot observe pronounced sub-gap features besides the JQP cycle. The weaker processes might be obscured by environmental noise.

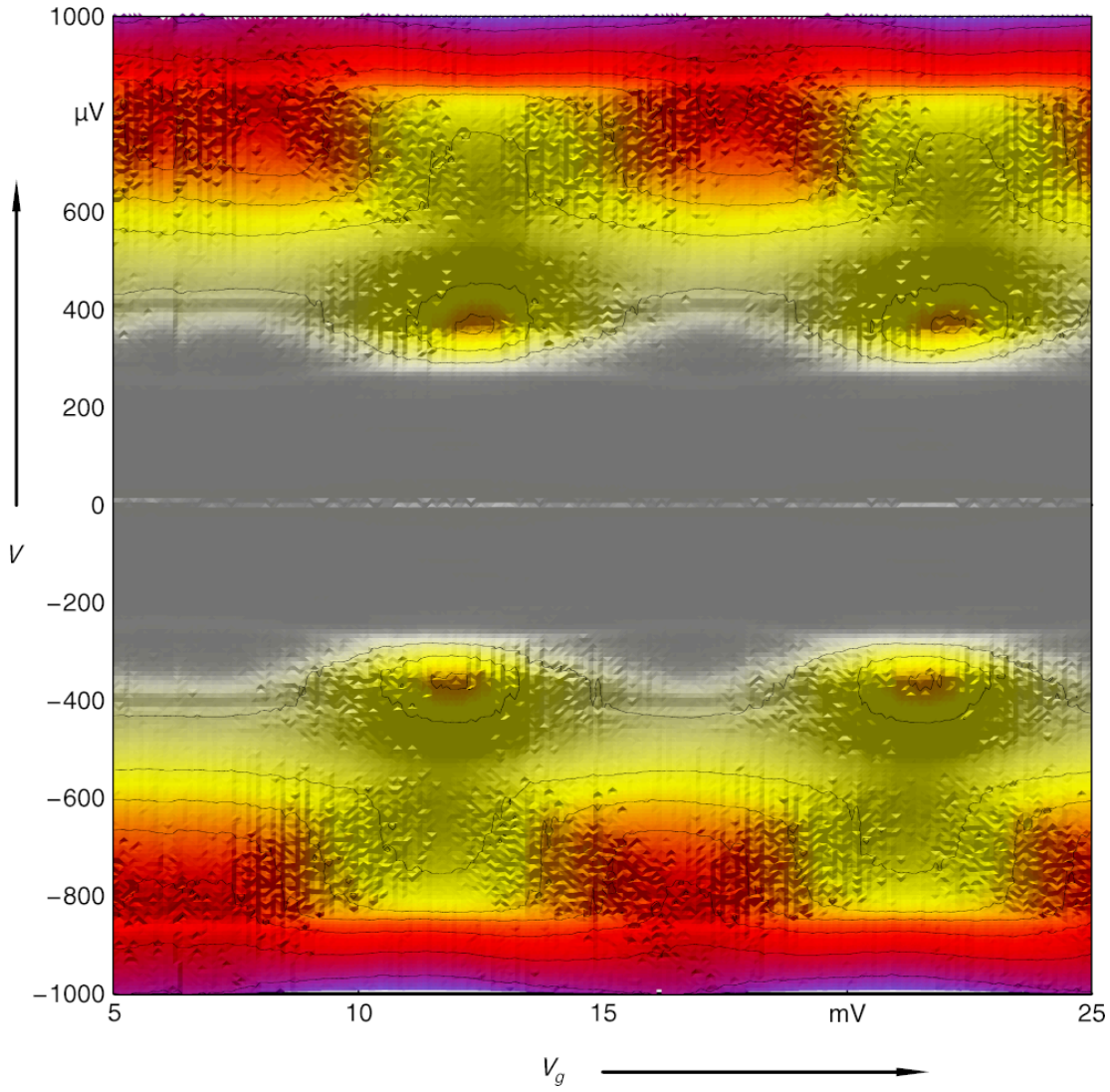


Figure 5.6: The same data as shown in Fig. 5.5 for sample 70I plotted in the 2-dimensional $V/V_g$-plane.

The peaks observed at $|V| \sim$340µV and 680µV represent the DJQP singular points and the crossing of the JQP lines, respectively. These features are used to derive $E_c$ =170µeV. They are more robust than other sub-gap features against noise because the current is bottlenecked by the Cooper pair tunneling which can only happen when the resonant condition is fulfilled.

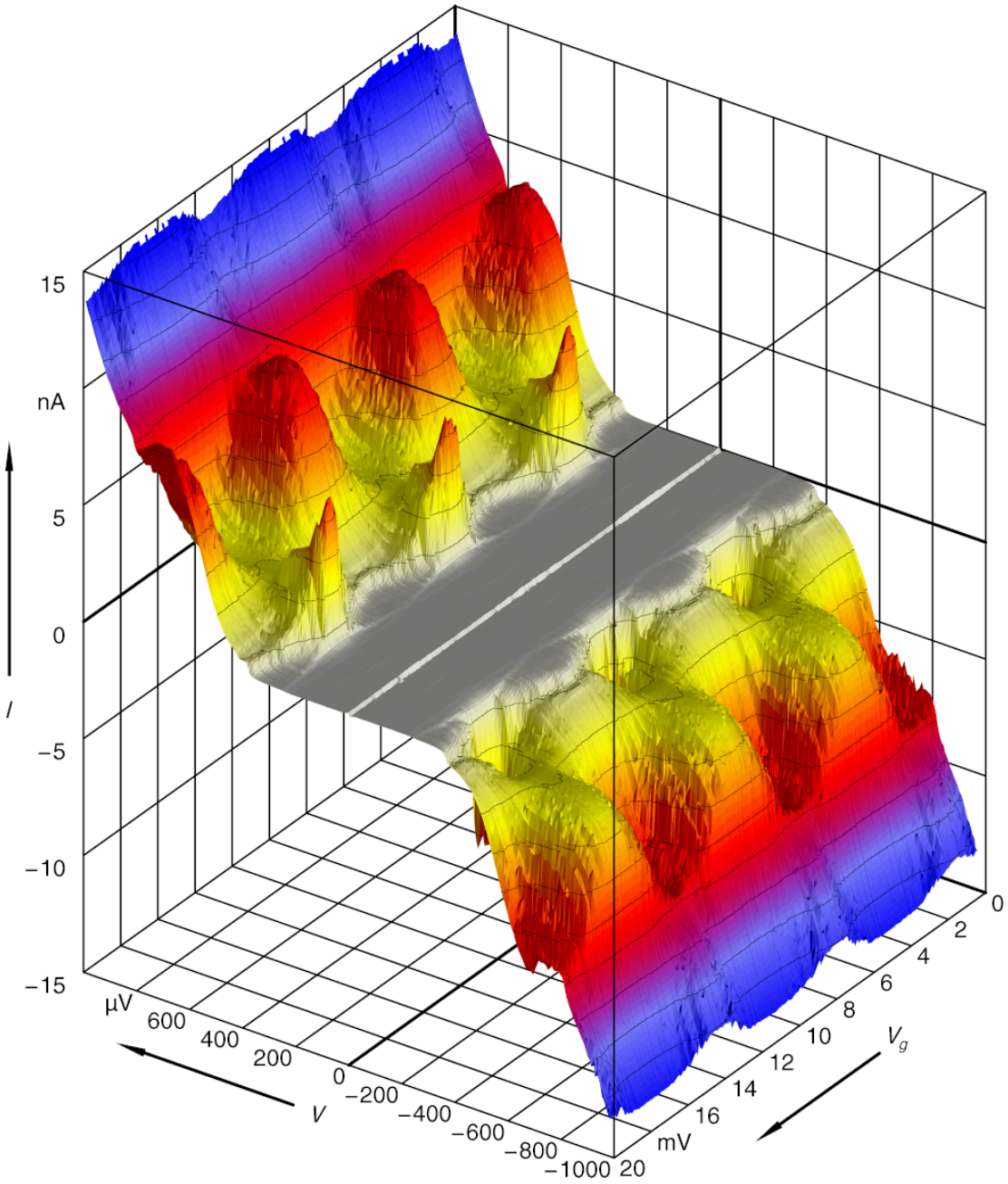


Figure 5.7: 3D plot of the measured current $I$ as a function of bias voltage $V$ and gate voltage $V_g$ for sample 70Ib.

Fig. 5.7 and Fig. 5.8 show the measurement data of sample 70Ib which is fabricated on the same chip as sample 70I. Because sample 70 and sample 70Ib are made by the same process, they have very similar characteristics. The DJQP peaks for sample 70Ib are at the bias voltage

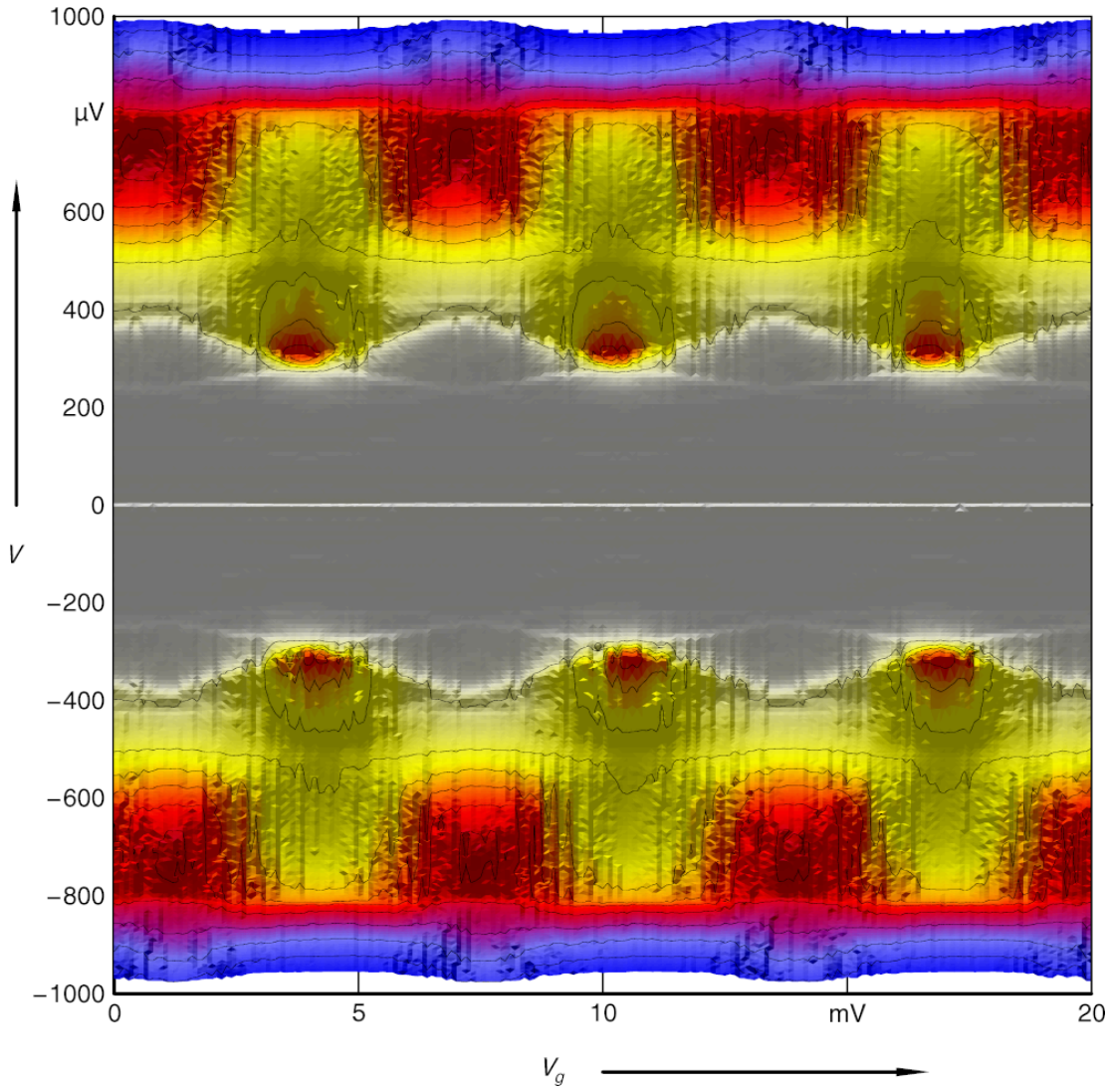


Figure 5.8: The same data as shown in Fig. 5.7 for sample 70Ib plotted in the 2-dimensional $V/V_g$-plane.

$V$ =310μV which gives the charging energy $E_c$ =155μeV. The current peaks at $4E_c$ which are due to the crossover of adjacent Josephson quasiparticle cycle lines are also consistent with the $E_c$ value obtained from DJQP. The superconducting energy obtained from the $4\Delta$ positions is 205μeV.

We have a slightly improvement on the noise performance of this sample: the 3e process can be seen clearly in this measurement. In Fig. 5.8, this happens at the voltage range between 270μV and 370μV. The improved quality of this measurement is due to an upgrade in the grounding scheme of our room-temperature setup.

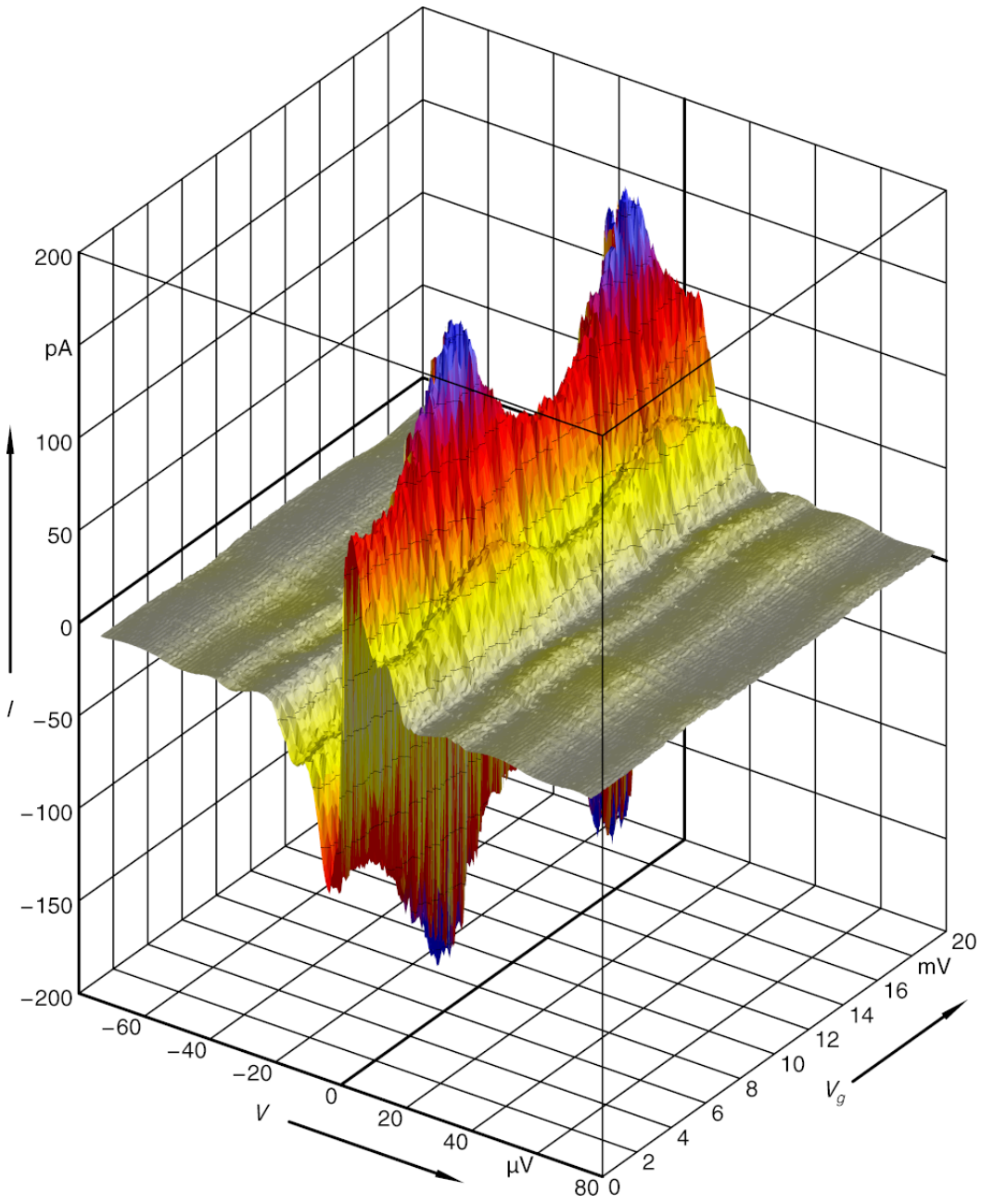


Figure 5.9: Another 3D plot of the measured current $I$ as a function of bias voltage $V$ and gate voltage $V_g$ for sample 70Ib.

Fig. 5.9 shows the measured current through the transistor 70Ib as a function of the bias voltage and gate voltage for the same sample as Fig. 5.7. These data are taken for a reduced bias voltage range -75μV< $V$ <75μV and provide a closer look at the supercurrent branch.

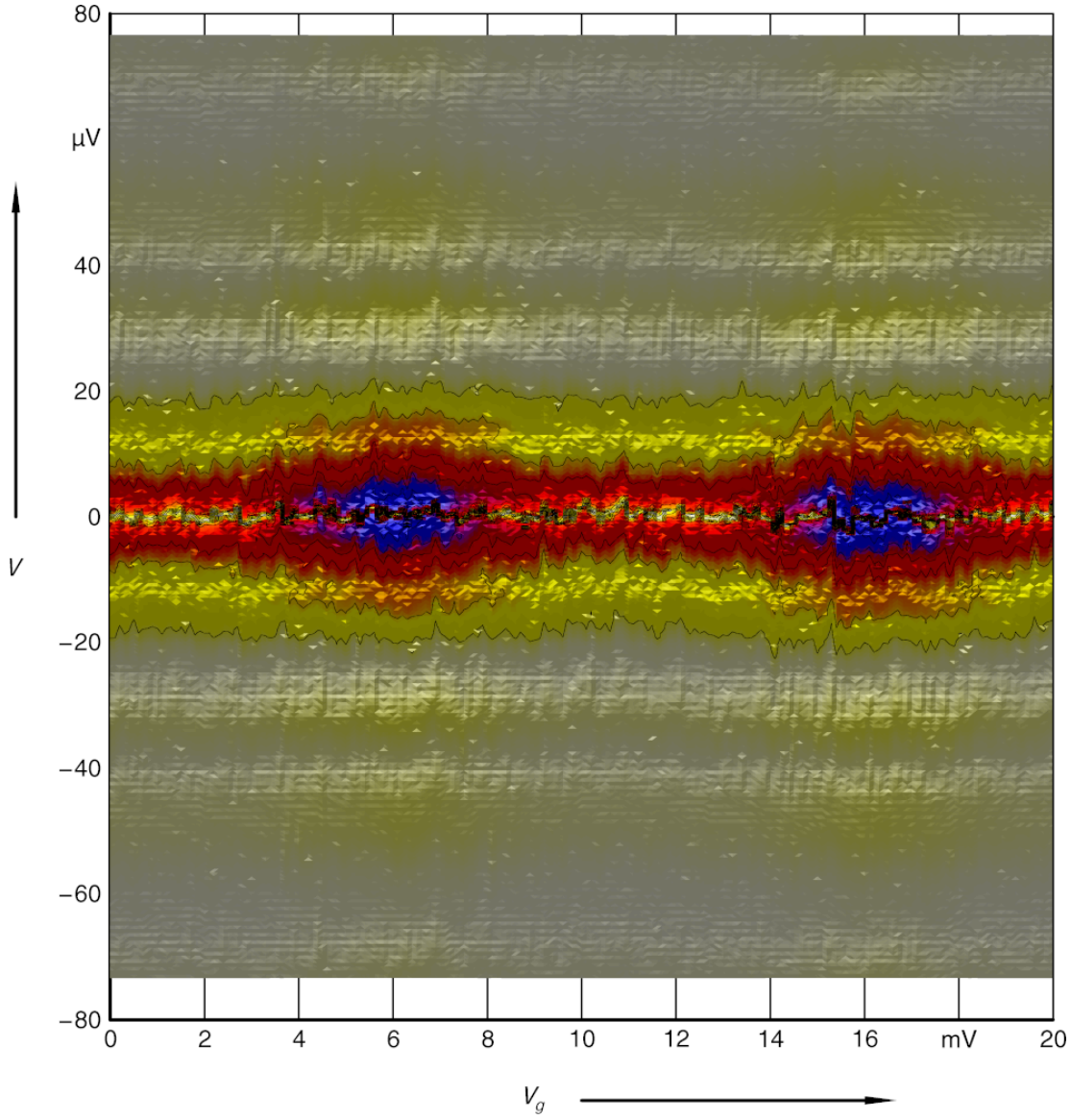


Figure 5.10: The same data as shown in Fig. 5.9 for sample 70Ib plotted in the 2-dimensional $V/V_g$-plane.

We clearly see a e-periodic modulation of the peak height. The overall peak height of around 100pA is well below the predicted switching current.

Fig. 5.10 shows the same data as Fig. 5.9. A series of horizontal parallel lines can be seen in this figure. We could not identify the origin of these lines, but attribute them to an unknown noise source, presumably related to interference with RF radiation.

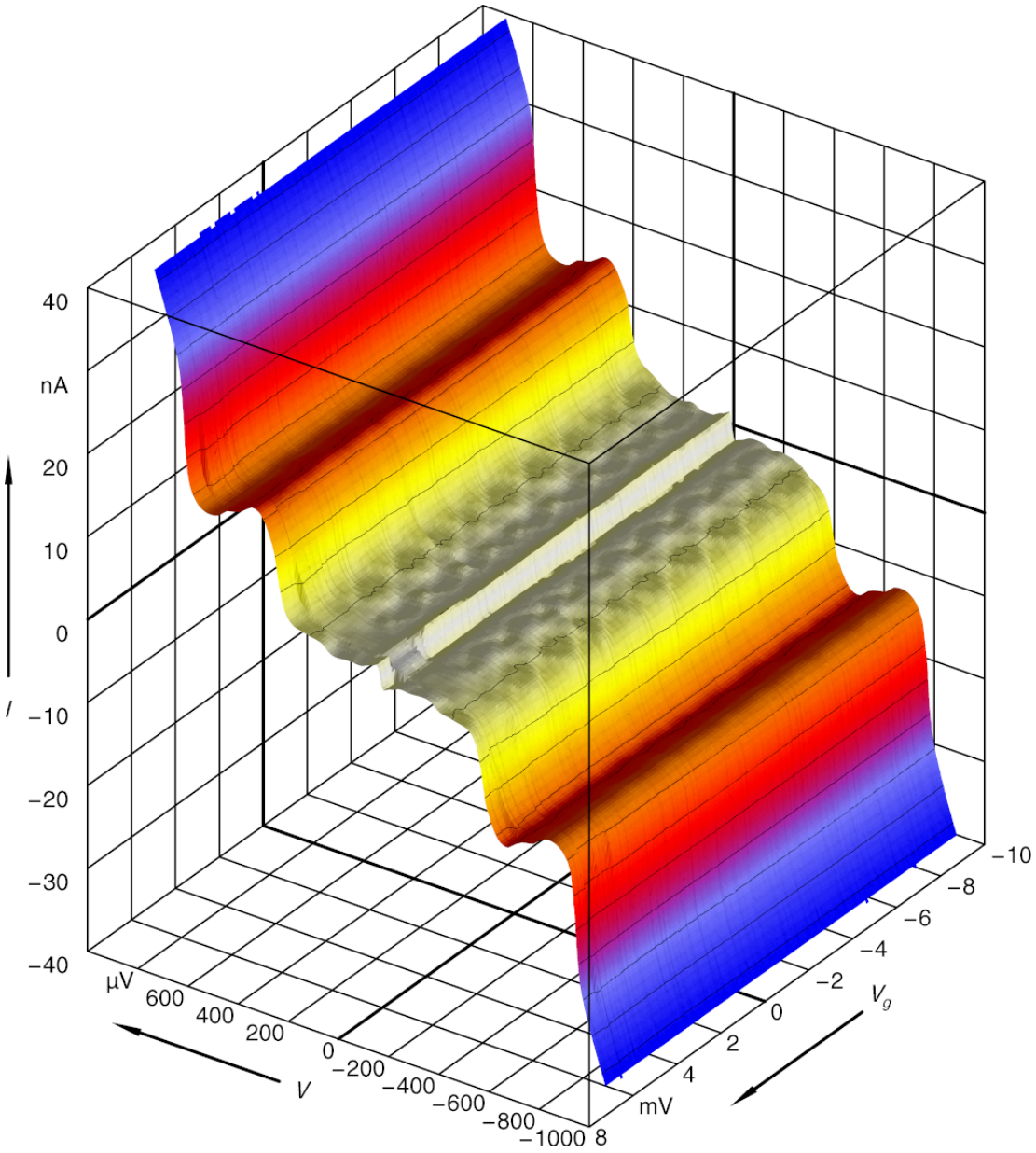


Figure 5.11: 3D plot of the measured current $I$ as a function of bias voltage $V$ and gate voltage $V_g$ for sample 73II.

Fig. 5.11 and Fig. 5.12 show the measured current of sample 73II. From this measurement on, we installed low temperature load resistances to reduce the Nyquist noise. Each sample is equipped with a high valued resistor which can be used to current bias the device in parallel with a lower valued resistor ($R \sim 8\text{k}\Omega$) which can be used either as voltage bias lead or as a voltage tap (in the voltage bias mode, the high resistor can be used for this purpose). As can be

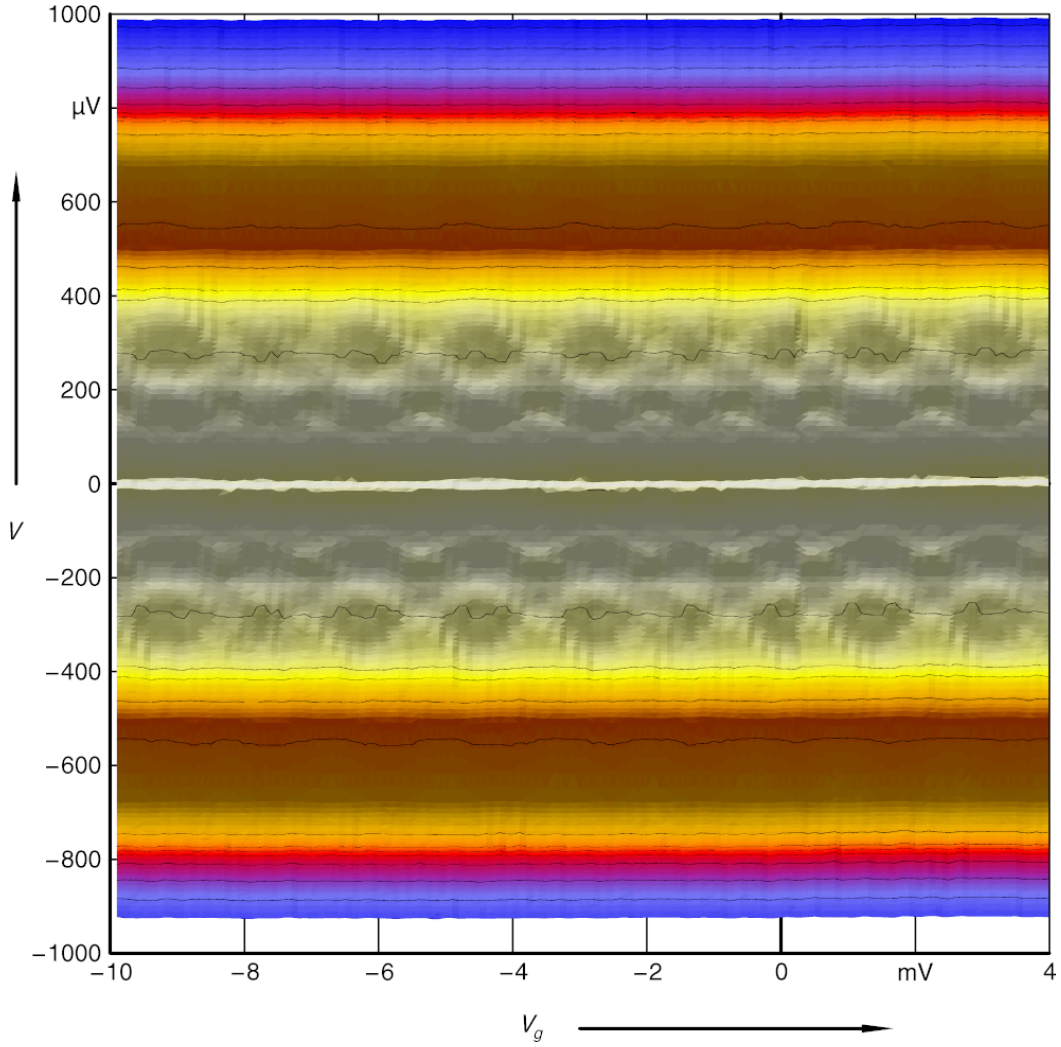


Figure 5.12: The same data as shown in Fig. 5.11 for sample 73II plotted in the 2-dimensional $V/V_g$-plane.

seen from the figures, this new setup gives us considerable improvement.

Sample 73II behaves differently than all other samples presented here. Presumably, the sample had larger tunneling contacts which lead to a reduced resistance (and larger $E_j$) as well as larger capacitances (and smaller $E_c$). The smallness of $E_c$ results in a shifting of JQP and DJQP to lower bias voltages. The ridges at 400µV and 800µV are due to the onset of Andreev reflection related transport and the usual quasiparticle tunneling process. The latter feature does not show any noticeable gate dependence which again can be explained by the large Josephson coupling strength.

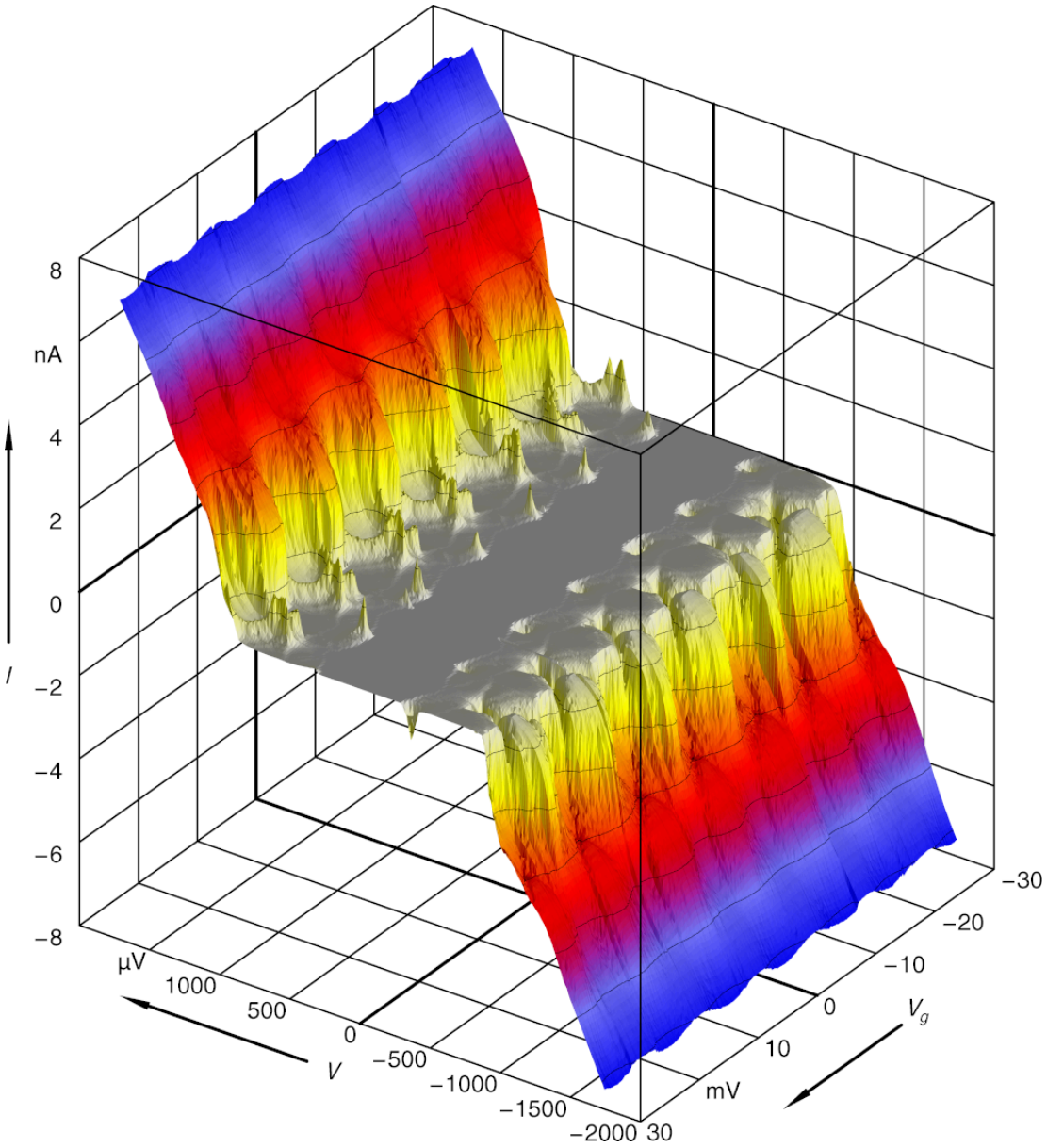


Figure 5.13: 3D plot of the measured current $I$ as a function of bias voltage $V$ and gate voltage $V_g$ for sample 81II.

Big improvement was made for the measurement of sample 81II. We installed capacitors between our sample and the low temperature resistors, thus forming a cold RC filter of bandwidth 10kHz. By doing so, we effectively reduced low frequency noise contributions which are below the cutoff frequency of our metal powder filters. The improvement can be seen clearly in Fig. 5.13 which depicts the results of sample 81II. JQP lines, DJQP peaks, sequential quasi-

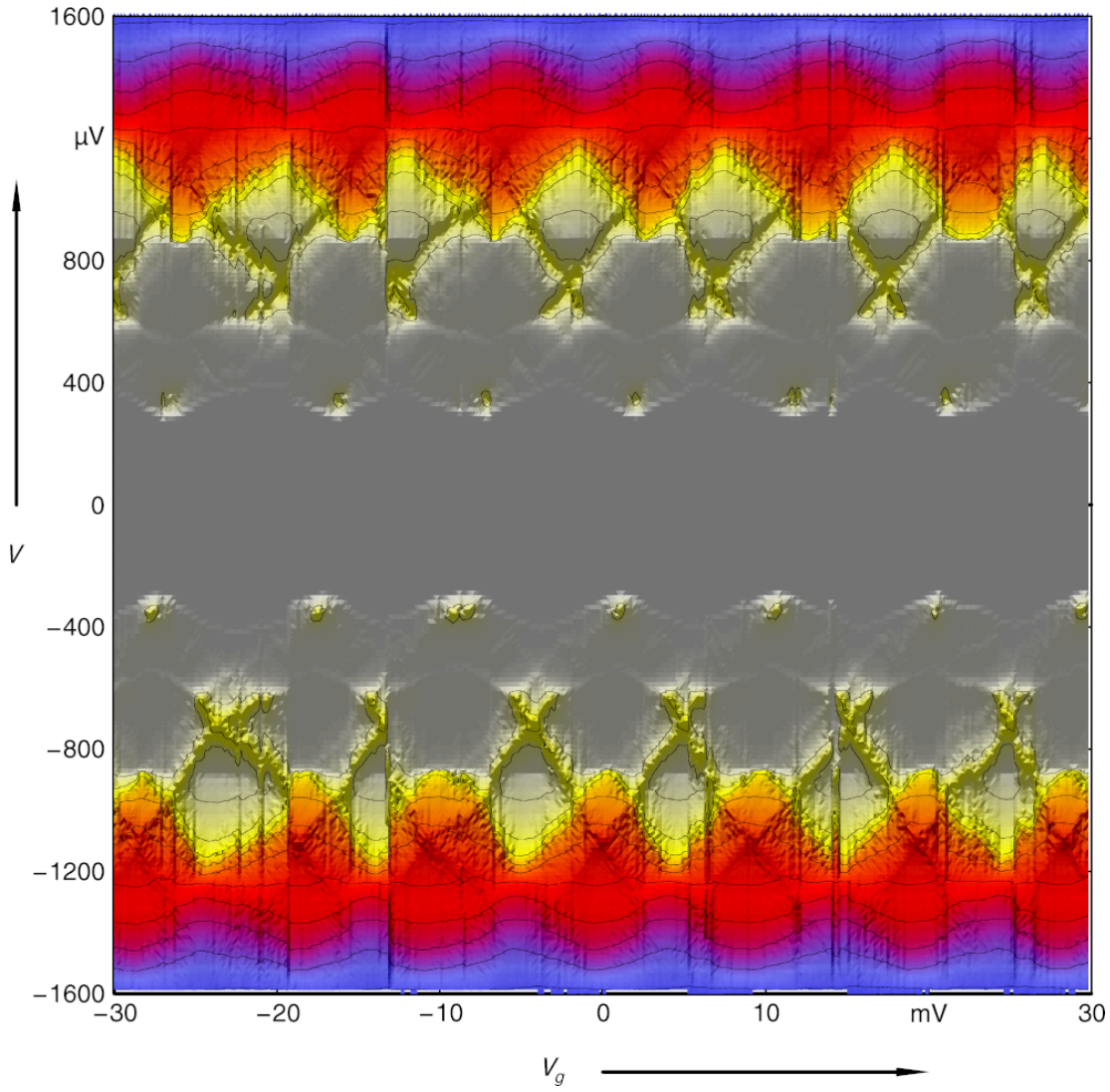


Figure 5.14: The same data as shown in Fig. 5.13 for sample 81II plotted in the 2-dimensional $V/V_g$-plane.

particle tunneling thresholds, and 3e features are well resolved and rather sharp.

In the measurement present in Fig. 5.15 and Fig. 5.16, we focus on the minus voltage bias side between -1.4mV and -0.2mV. The reduced bias range gives us higher resolution and numerous current features get more pronounced.

From the small voltage bias side, we can see the DJQP features at bias voltage $V = -347\mu V$ in Fig. 5.16. Close to these points, current ridges form white lines with a characteristic slope which identifies them as 3e processes.

Another interesting feature in this plot is the JQP ridge lines. Fulton et. al. (1989) gives the

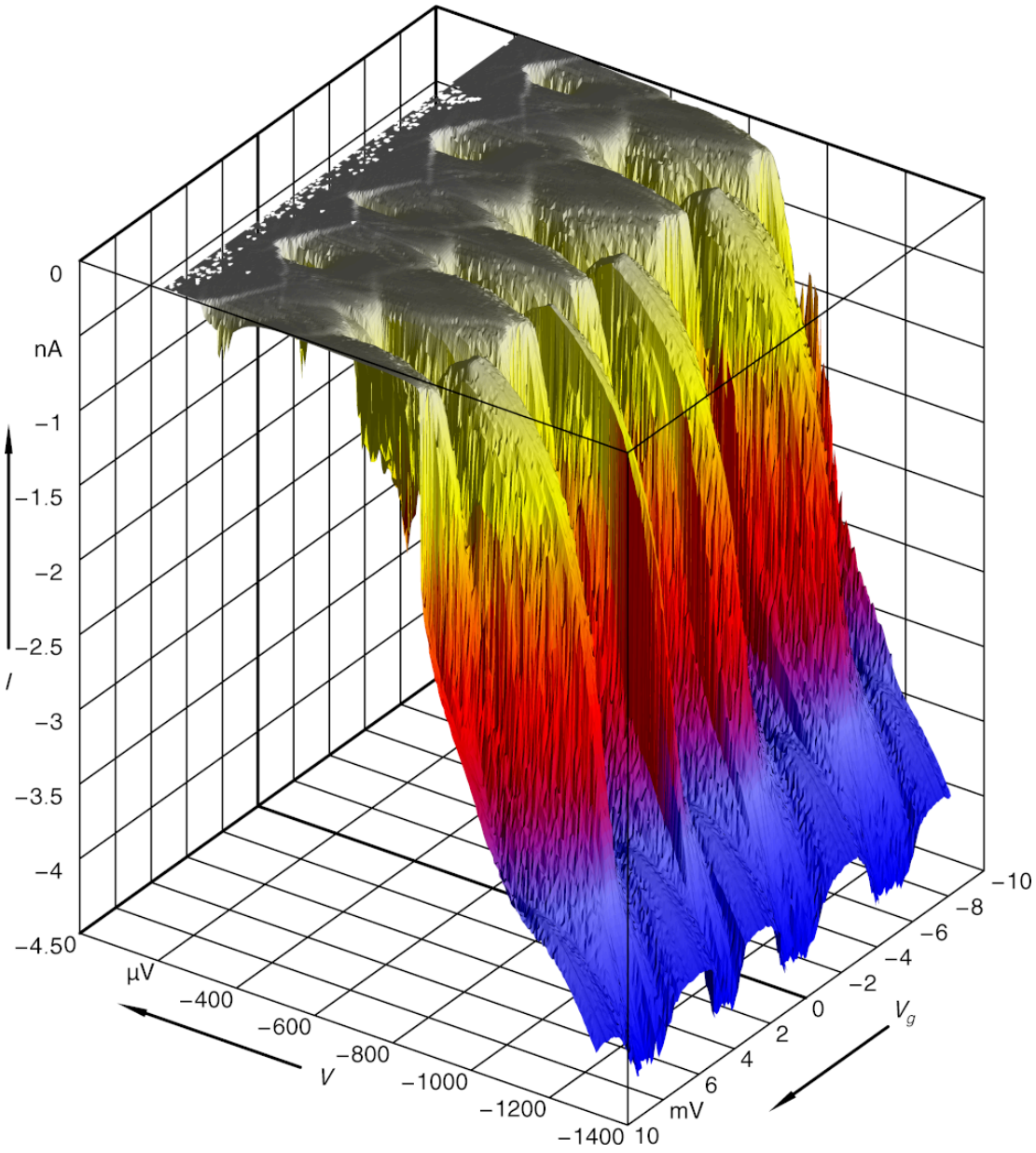


Figure 5.15: Another 3D plot of the measured current $I$ as a function of bias voltage $V$ and gate voltage $V_g$ for sample 81II.

limit that JQP happens for $2\Delta + E_c < |eV| < 2\Delta + 3E_c$. As stated in Sec. 2.3.1.2, it is normally assumed that an upper boundary for the JQP process exists and is given by the crossing of the Cooper pair resonance line with the quasiparticle tunneling ridge. Most experiments confirm this assumption which rely on the fact that a running JQP cycle requires a certain charge state to

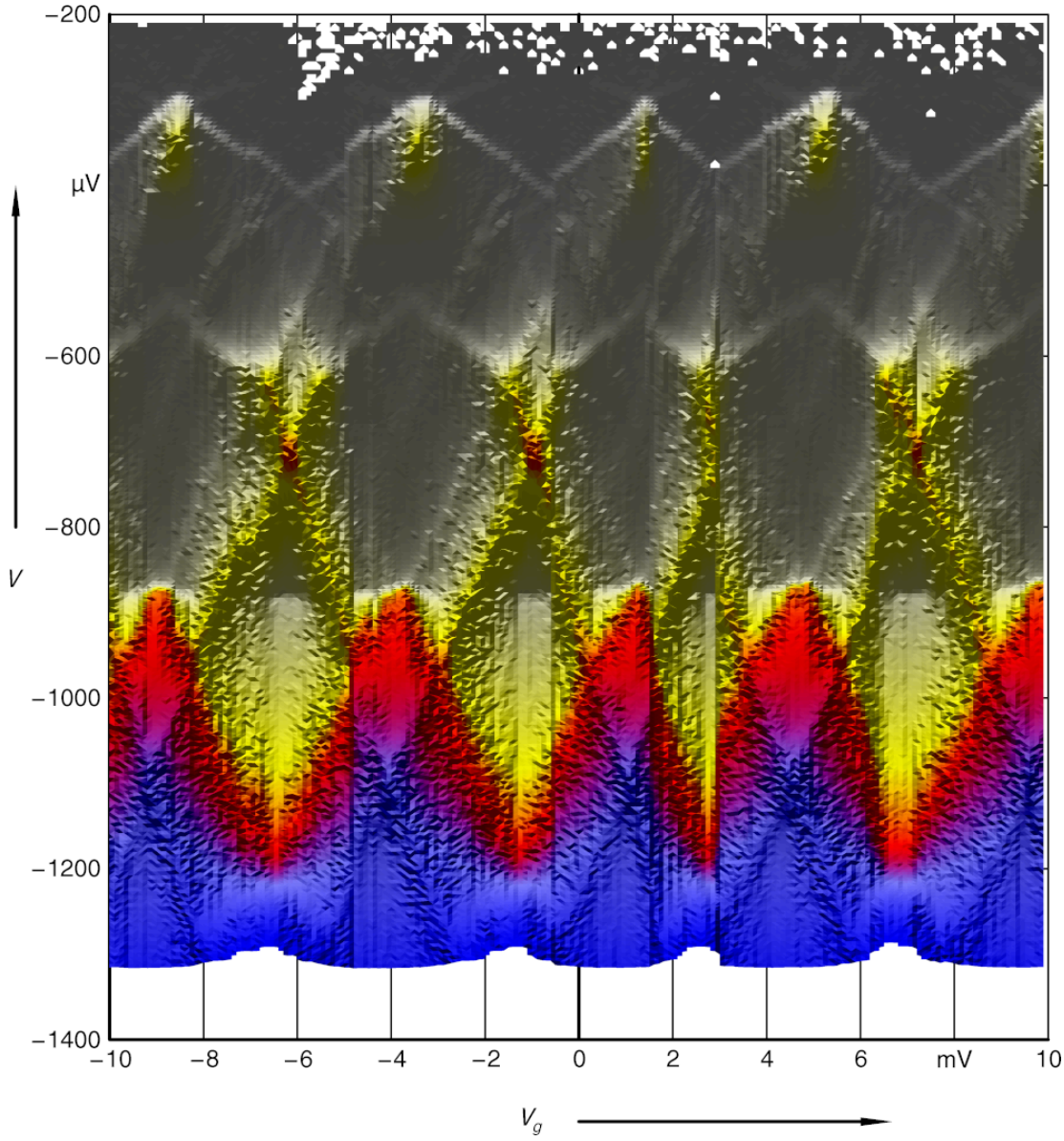


Figure 5.16: The same data as shown in Fig. 5.15 for sample 81II plotted in the 2-dimensional $V/V_g$-plane.

be stable. Above the quasiparticle threshold, the resonant state is unstable against decaying to an adjacent quasiparticle charge state in which the resonant condition is not fulfilled any more. The extension of the JQP line across this border indicates relatively low quasiparticle rates, so as to make it possible to leave the cycle running for a considerable time.

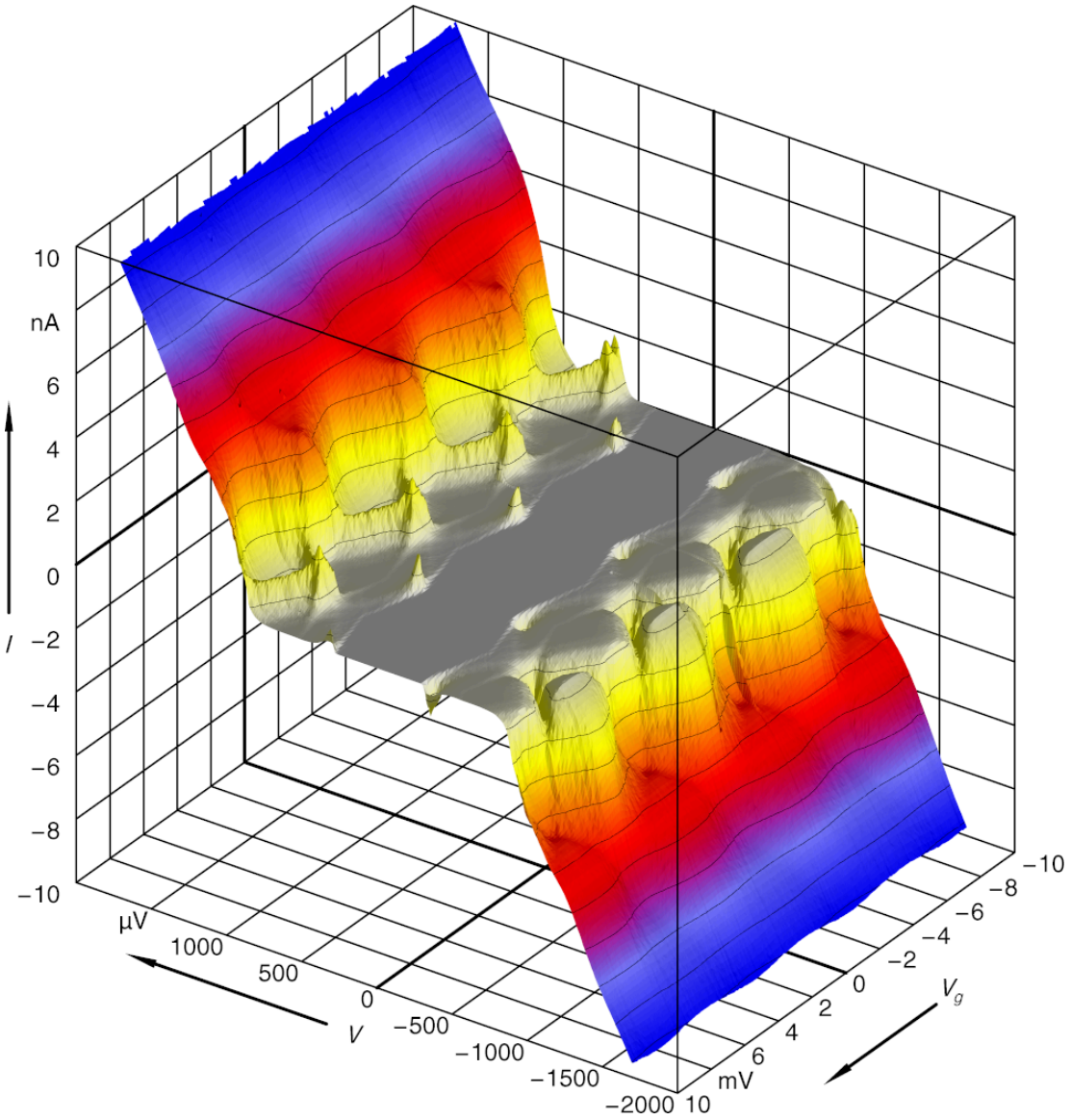


Figure 5.17: 3D plot of the measured current $I$ as a function of bias voltage $V$ and gate voltage $V_g$ for sample 81III.

Measurements on sample 81III do have an even higher quality, presumably due to differences in the wiring lines. The most interesting features are related to 3e processes. First of all, the usual current onset can be observed in Fig. 5.18 as zigzag line aligned with the DJQP singular points just below 400μV. In addition, and surprisingly, we find a further zigzag line at higher bias aligned with the lower bias crossing of the JQP. We are going to discuss this feature in Sec. 5.2.2.

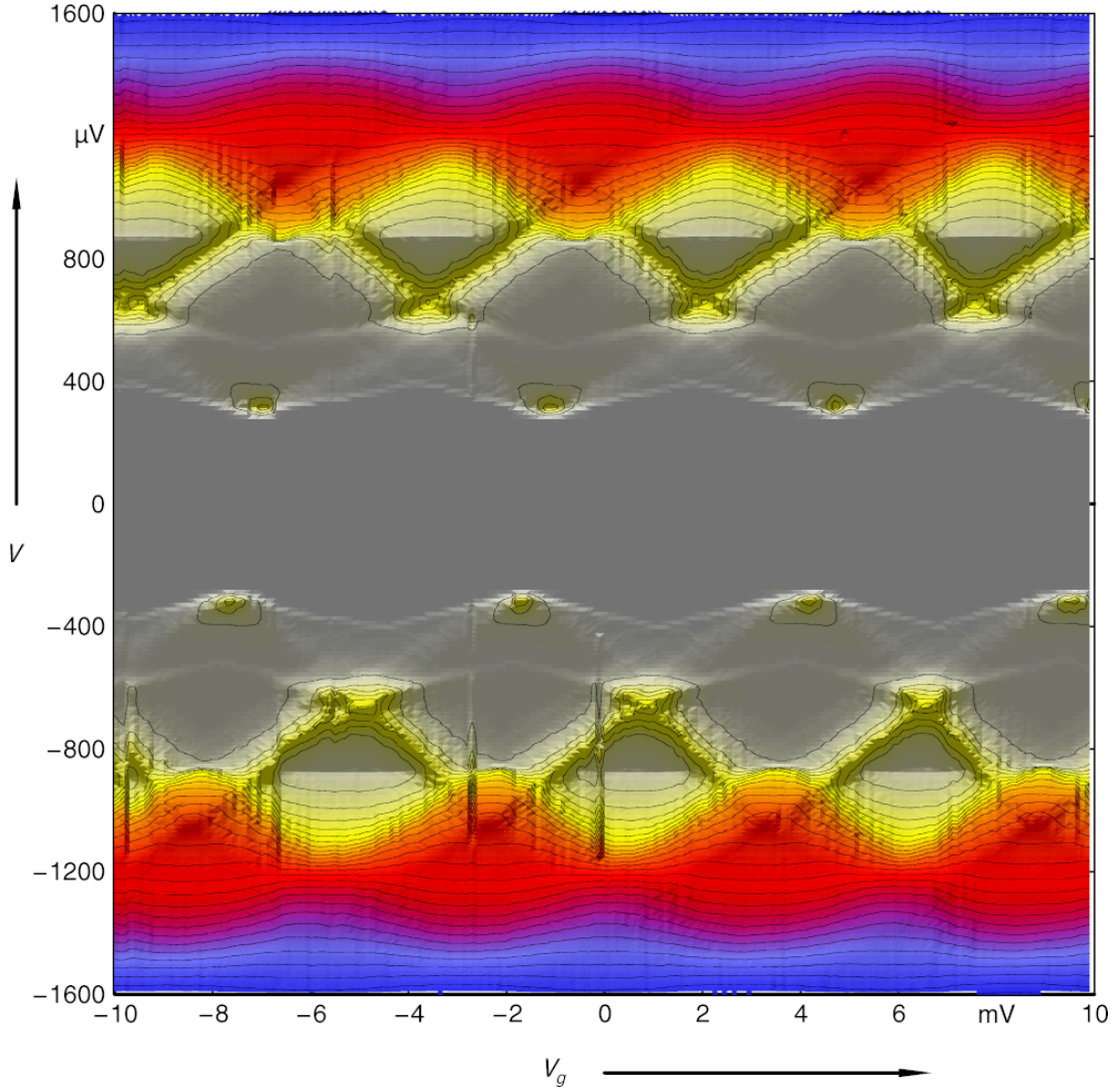


Figure 5.18: The same data as shown in Fig. 5.17 for sample 81III plotted in the 2-dimensional $V/V_g$-plane.

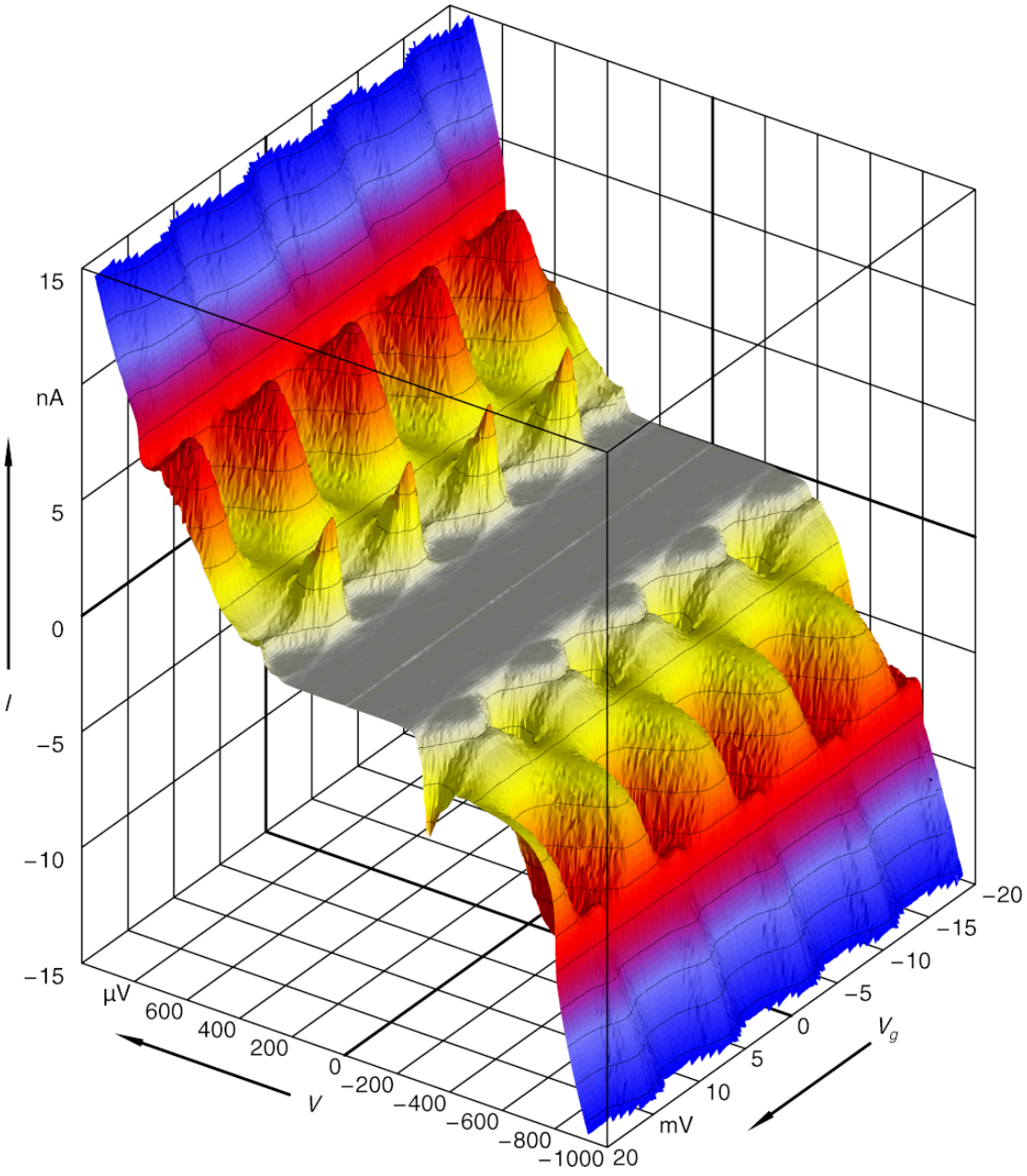


Figure 5.19: 3D plot of the measured current $I$ as a function of bias voltage $V$ and gate voltage $V_g$ for sample 82IIIa.

The tunneling barriers of sample 82IIIa are thinner comparing with 81III due to the lower oxygen pressure during the oxidation step. So the Josephson coupling energy $E_j$ is larger for this sample, which yields quite different current features as a function of the bias voltage and gate voltage, see Fig. 5.19 and Fig. 5.20. Although current peaks at $V$ =290μV and $V$ =600μV

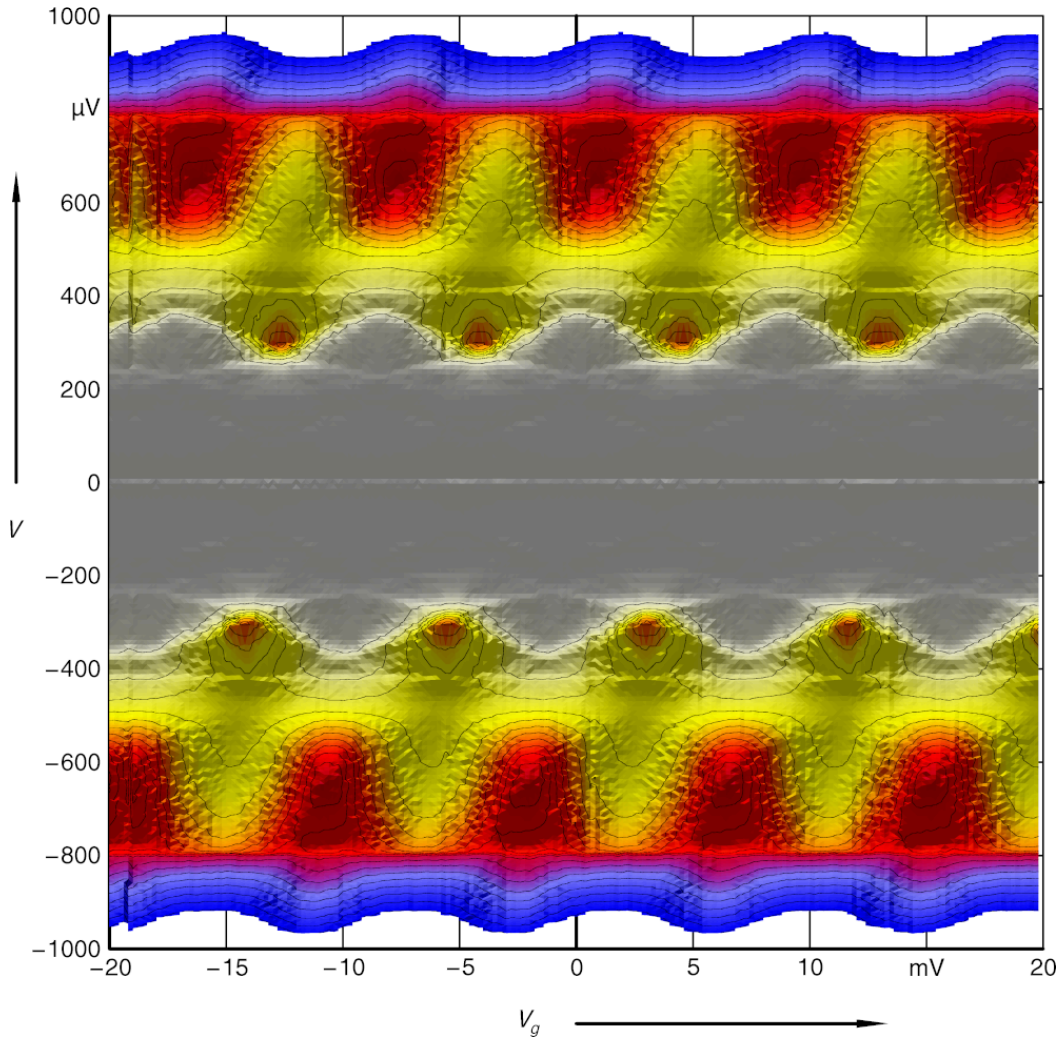


Figure 5.20: The same data as shown in Fig. 5.19 for sample 82IIIa plotted in the 2-dimensional $V/V_g$-plane.

which are due to DJQP and JQP cycles are still visible for this sample, the line defined by the JQP cycle ridges can not be seen any more from these figures.

Instead, sub-gap features which are in the voltage bias range below the DJQP feature are observed in Fig. 5.20. Some of these features below the voltage bias 200μV represent the resonant Cooper pair tunneling. This is the first time that we observed these features. Slightly above the RCPT but below the DJQP, we have further current features which might be due to higher order tunneling processes. Also clearly visible are the 3e features in the bias voltage range from 270μV to 370μV. we see also clear direct line independent on gate voltage $V_g$ at the bias voltage $V$ around 400μV, of yet unsolved origin.

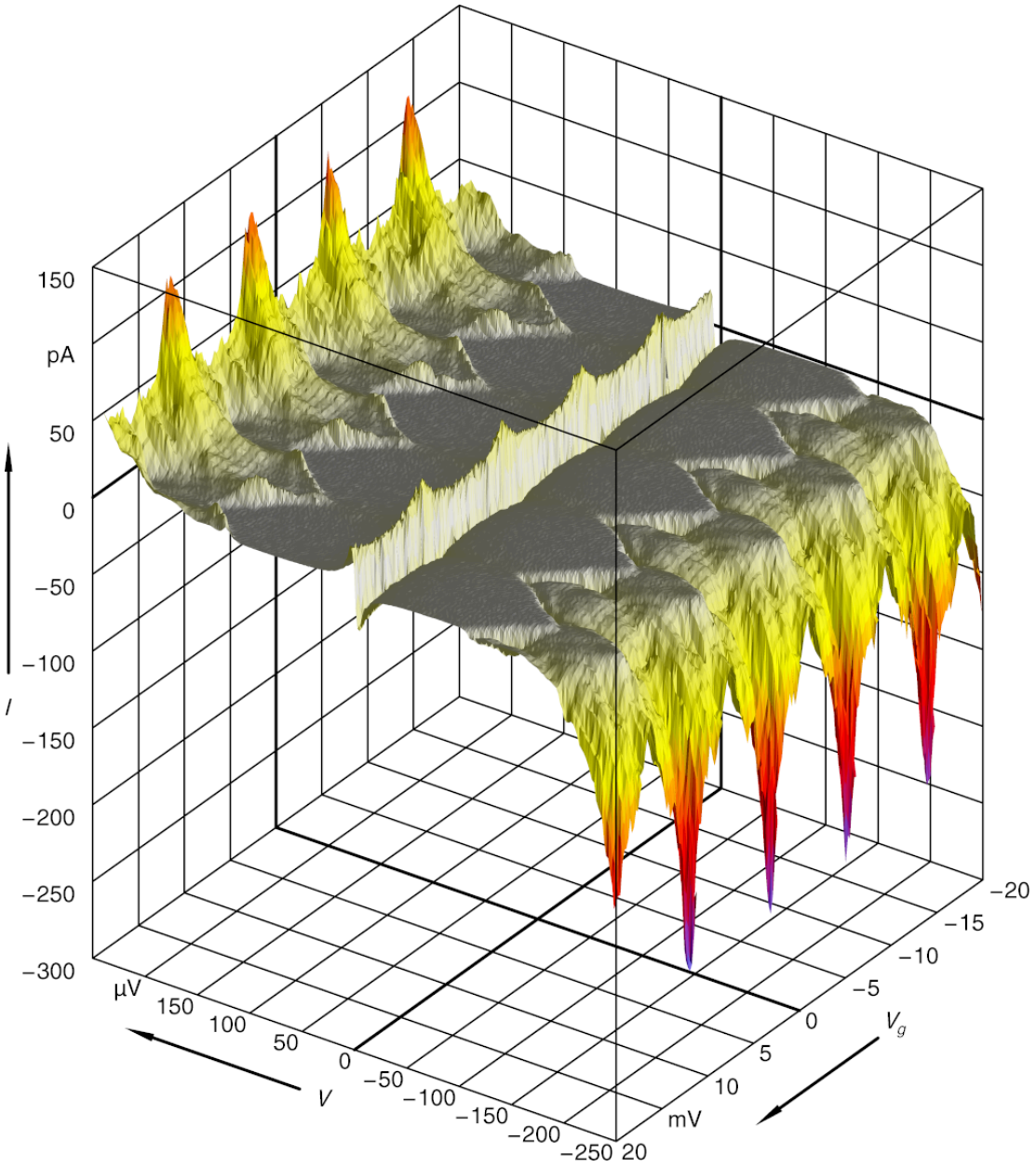


Figure 5.21: Another 3D plot of the measured current $I$ as a function of bias voltage $V$ and gate voltage $V_g$ for sample 82IIIa.

Fig. 5.21 and Fig. 5.22 show a measurement on the sample 82IIIa, focusing on the sub-gap features in the bias range below the DJQP. The lines of the current ridges which are clearly visible follow resonance condition for third order Cooper pair tunneling. This process is expected to persist down to very low biases, where it merges with the maxima in the supercurrent branch

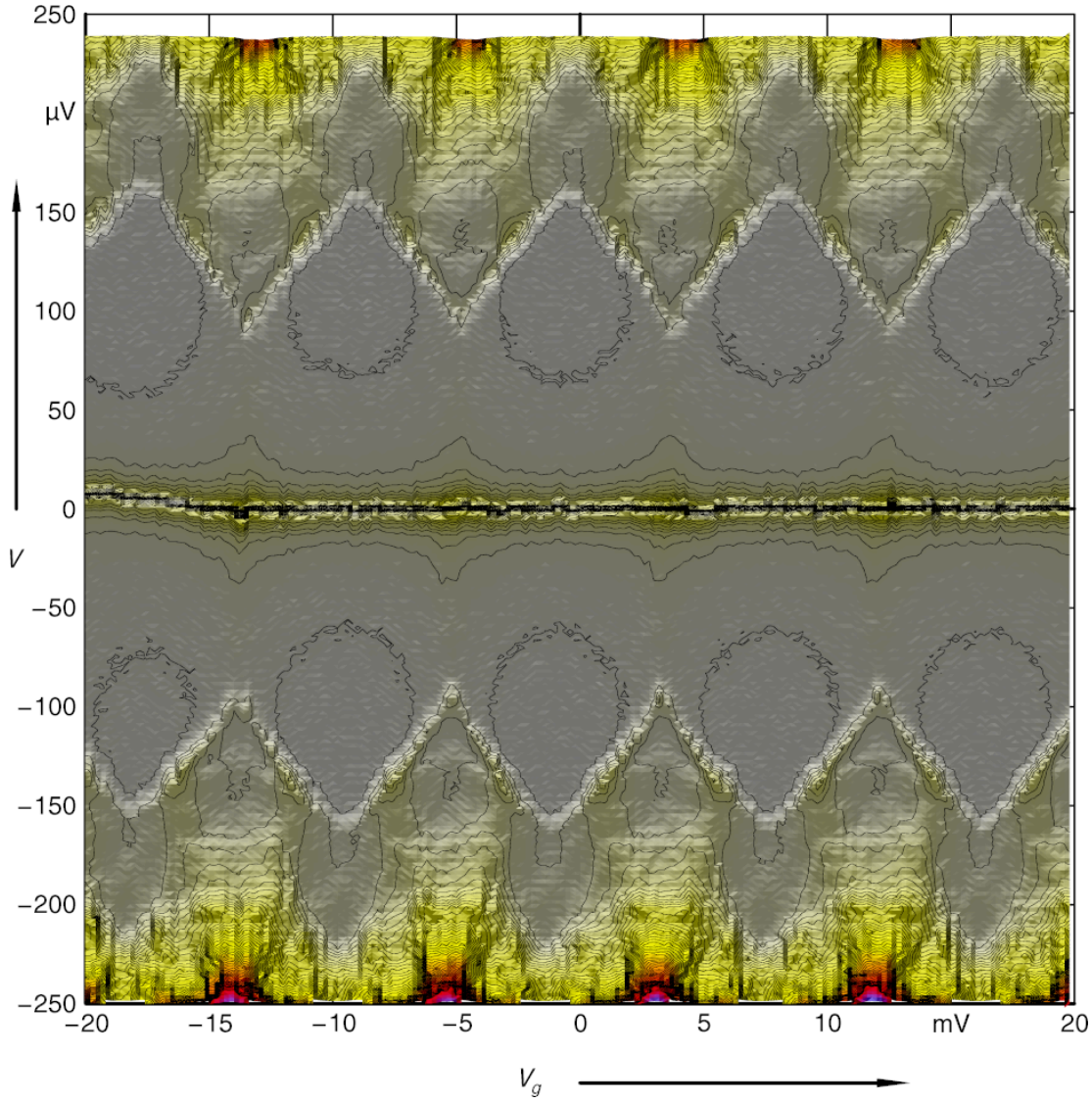


Figure 5.22: The same data as shown in Fig. 5.21 for sample 82IIIa plotted in the 2-dimensional $V/V_g$-plane.

(Joyez, 1995). In our case, they are sharply ending at the crossing point around 100µV. We will come back to this observation in Sec. 5.2.2.

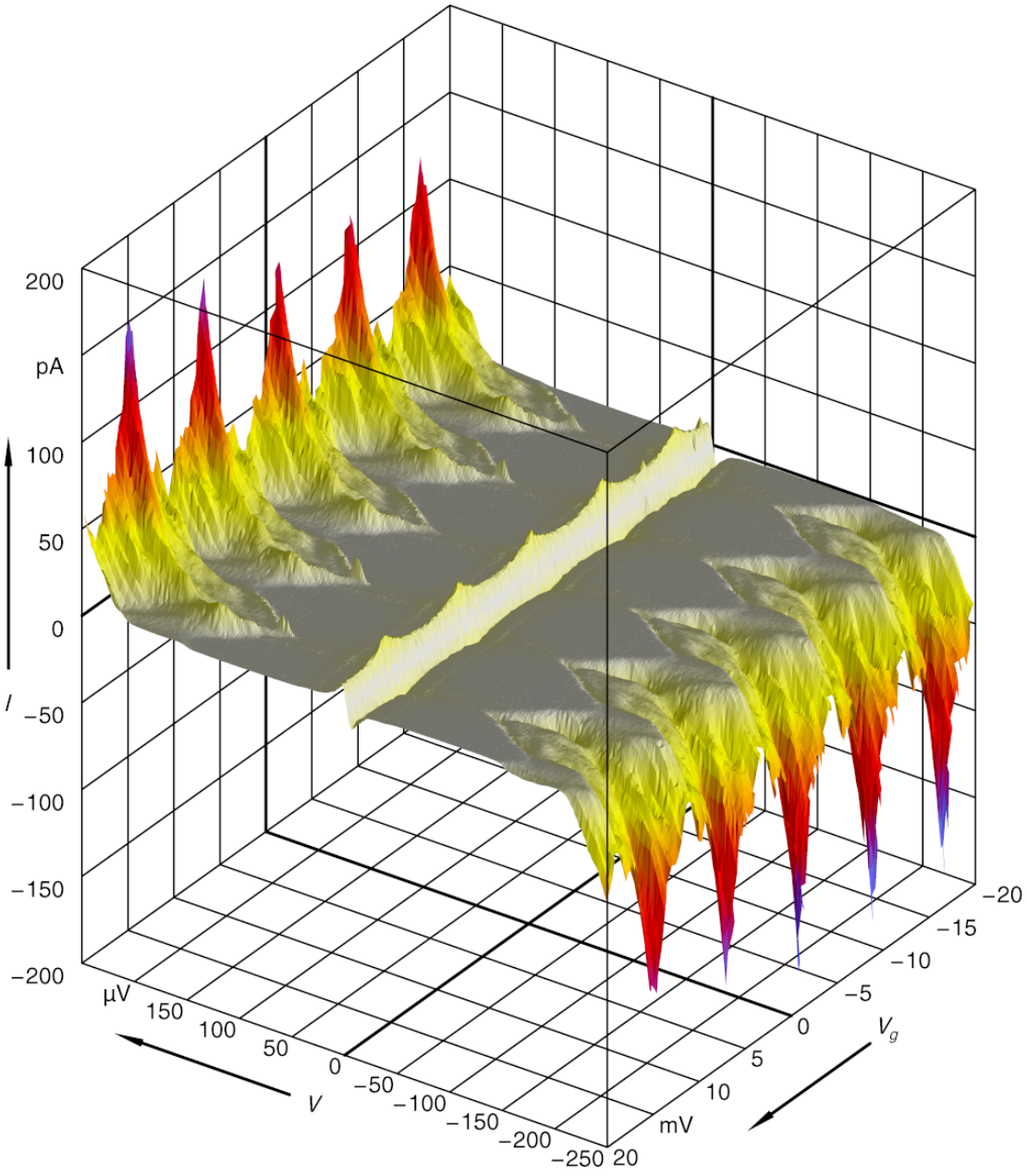


Figure 5.23: 3D plot of the measured current $I$ as a function of bias voltage $V$ and gate voltage $V_g$ for sample 82IVa.

Sample 82IVa has similar characteristics and correspondingly measurements on this sample (shown in Fig. 5.23 and Fig. 5.24) agree with measurements on the last page very well.

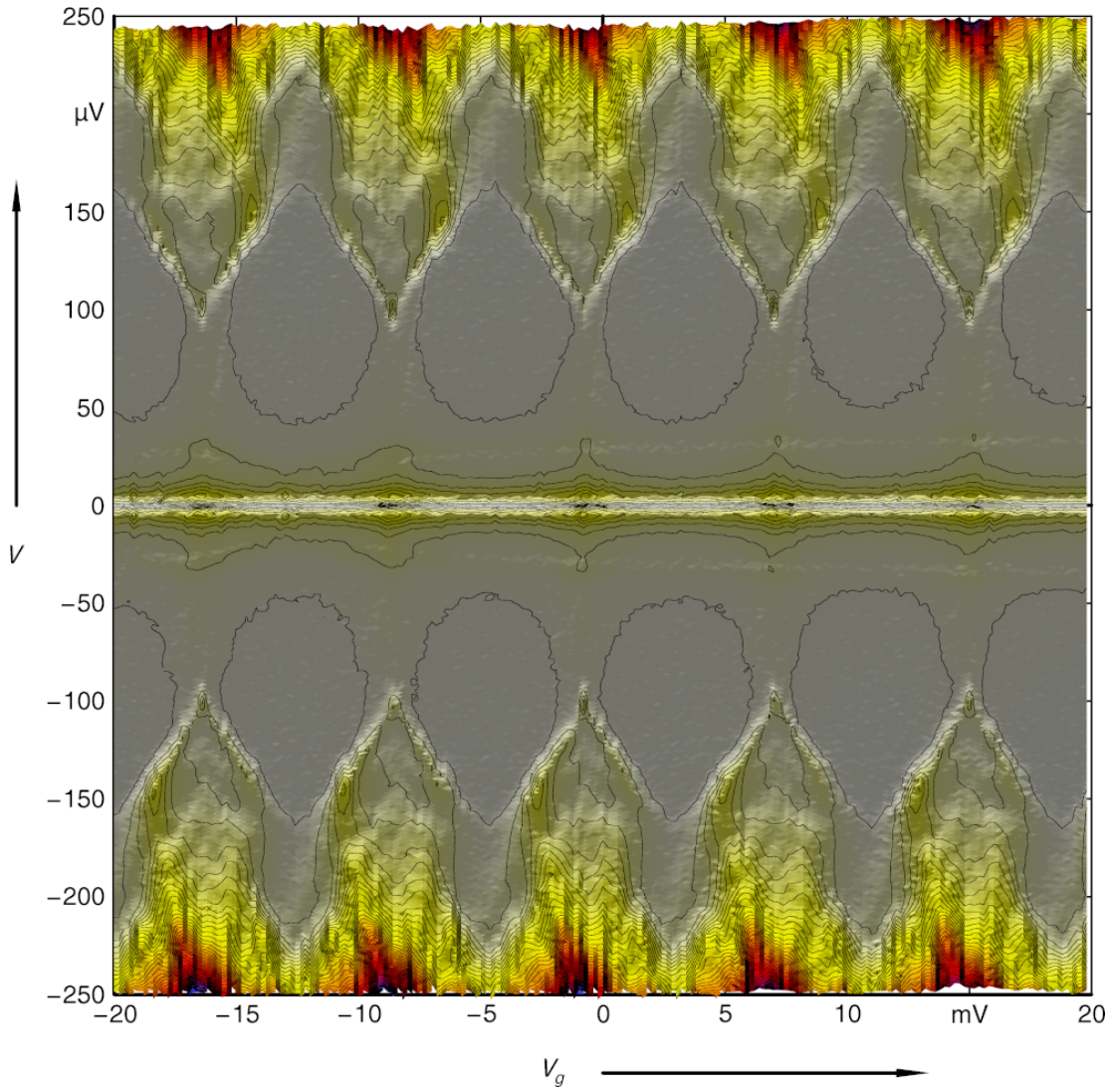


Figure 5.24: The same data as shown in Fig. 5.23 for sample 82IVa plotted in the 2-dimensional $V/V_g$-plane.

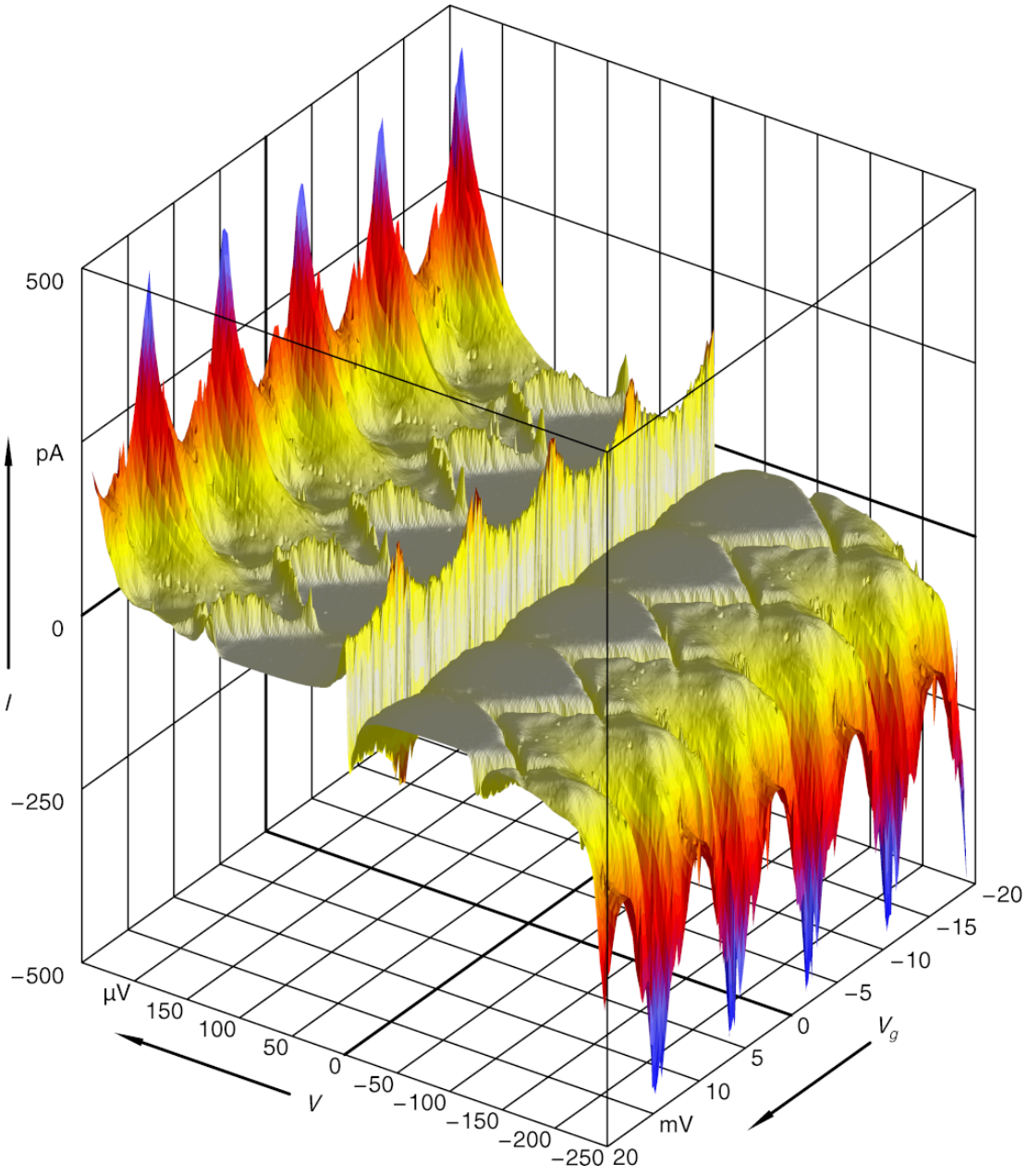


Figure 5.25: 3D plot of the measured current $I$ as a function of bias voltage $V$ and gate voltage $V_g$ for sample 82IVb.

Compared to the last two samples, sample 82IVb has a slightly reduced conductance and correspondingly a smaller $E_j$. The most prominent difference in measurements is that the resonant lines, while still emerging from the lower crossing point, extend to higher bias beyond the crossing at around 160μV.

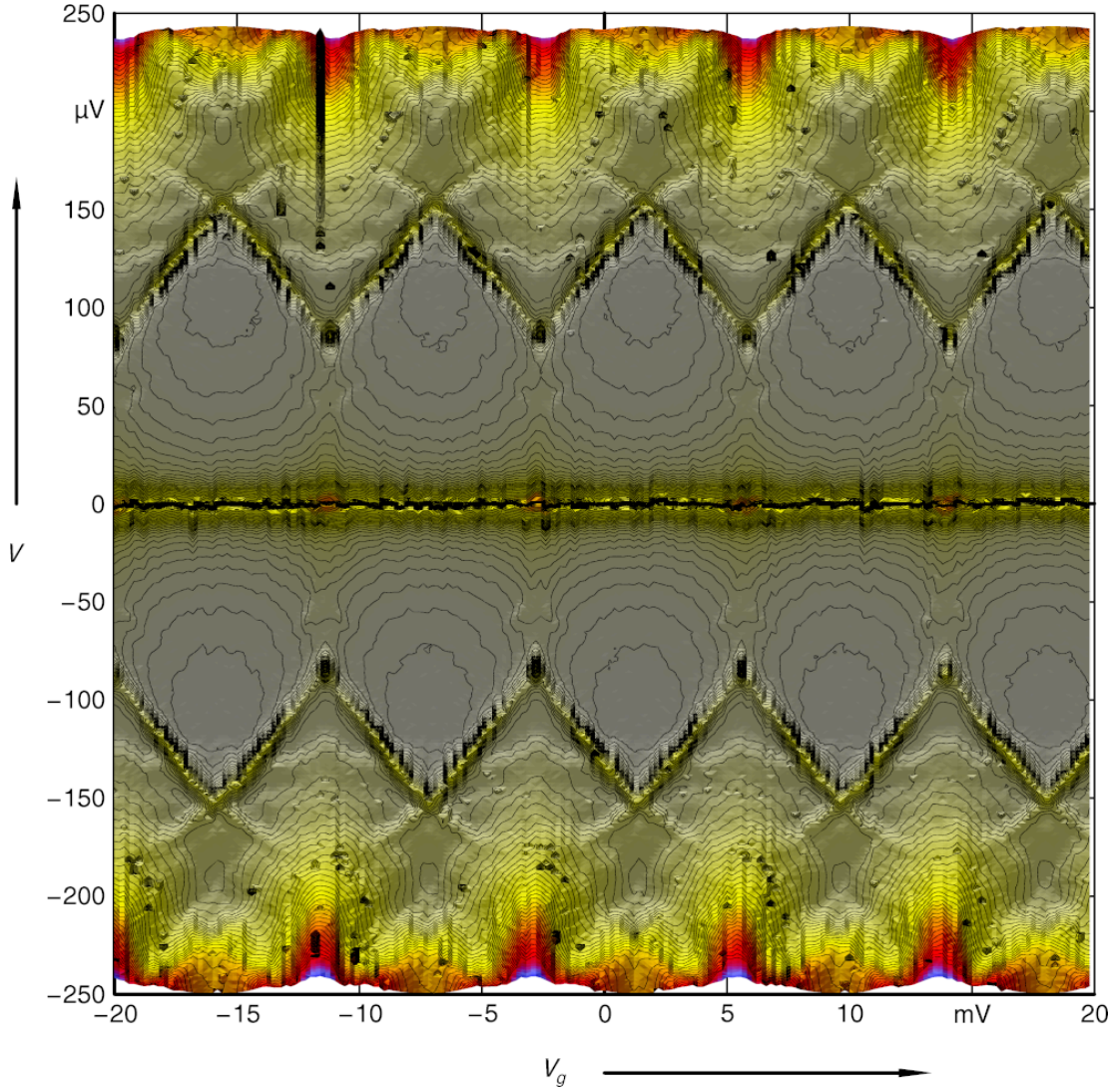


Figure 5.26: The same data as shown in Fig. 5.25 for sample 82IVb plotted in the 2-dimensional $V/V_g$-plane.

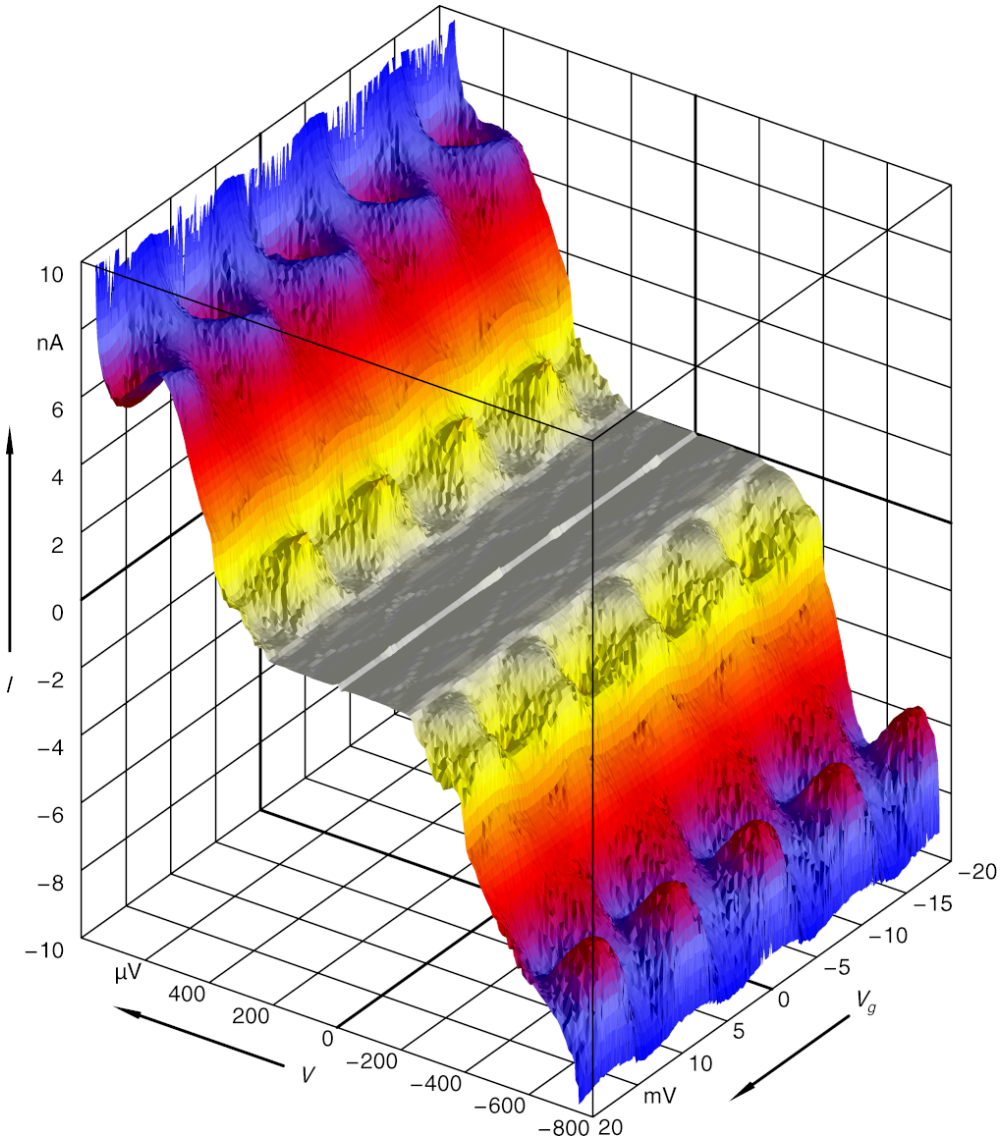


Figure 5.27: 3D plot of the measured current $I$ as a function of bias voltage $V$ and gate voltage $V_g$ for sample 94I.

The main difference between sample 94I presented on this page and the last samples is a change in the material for fabricating the quasiparticle filters (see Chap. 3). If one compares Fig. 5.19 with measurements on the present sample (see Fig. 5.27), one sees reasonable differences, which cannot be explained completely by the change in characteristics. The supercurrent branch is now much more pronounced and clearly show signs of 2e periodicity[2]. This might

[2] Pure 2e periodicity is not seen for this measurement. Instead, if we mark the gate voltage difference between

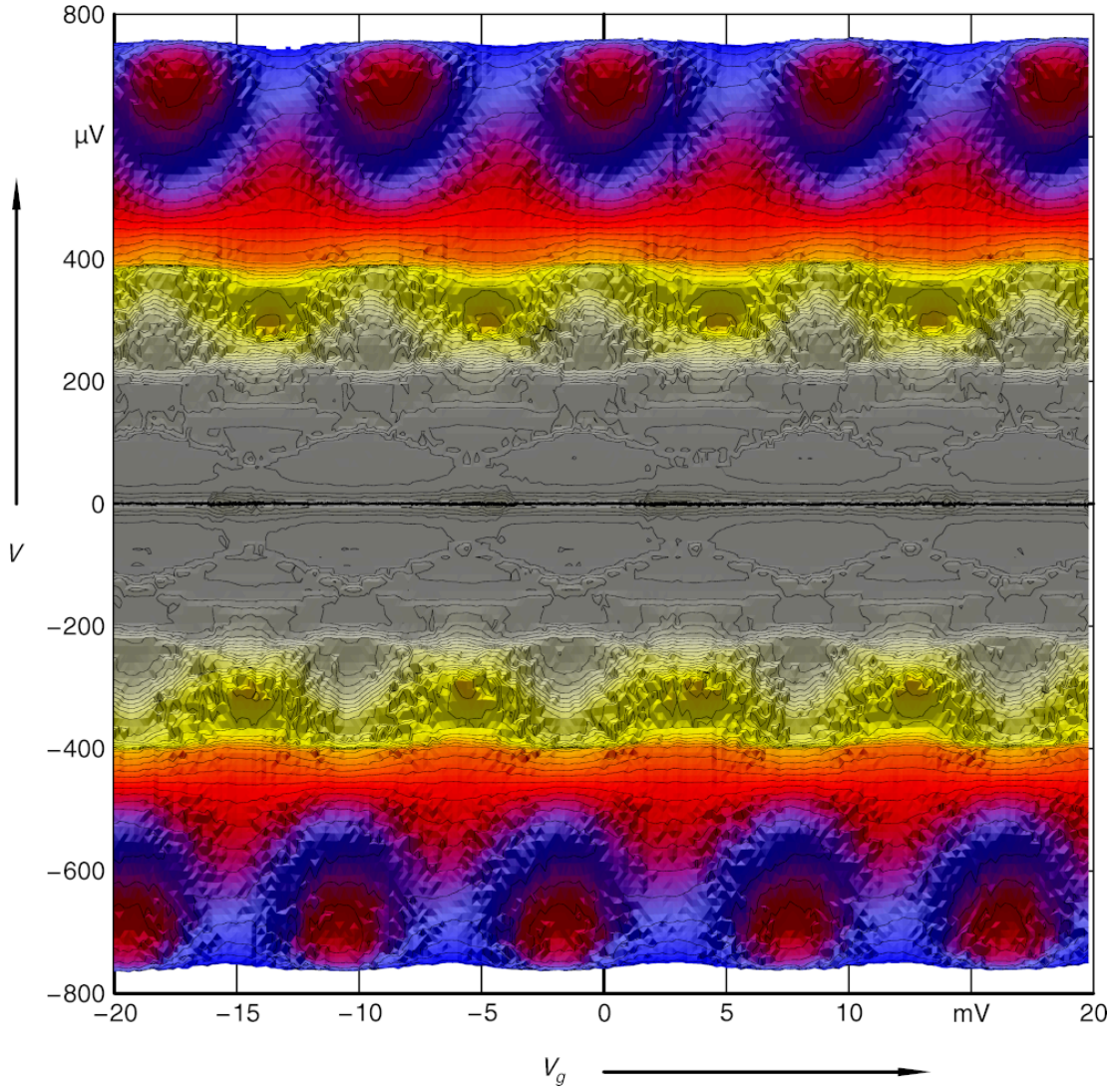


Figure 5.28: The same data as shown in Fig. 5.27 for sample 94I plotted in the 2-dimensional $V/V_g$-plane.

be due to the better filtering of the improved quasiparticle traps. But even at the position of the DJQP and the JQP, prominent differences can be observed. This latter fact might hint to a strong influence by the altered environmental impedance seen by the device due to high resistive parts in the leads.

two adjacent current peaks close to zero bias with $\Delta V_g$, two different $\Delta V_g$ values exist, 10mV and 6mV separately. Therefore a single period becomes 16mV which indicates 2e periodicity. This is in direct contrast to the supercurrent branch in Fig. 5.26, where $\Delta V_g$ has only one value, 8mV.

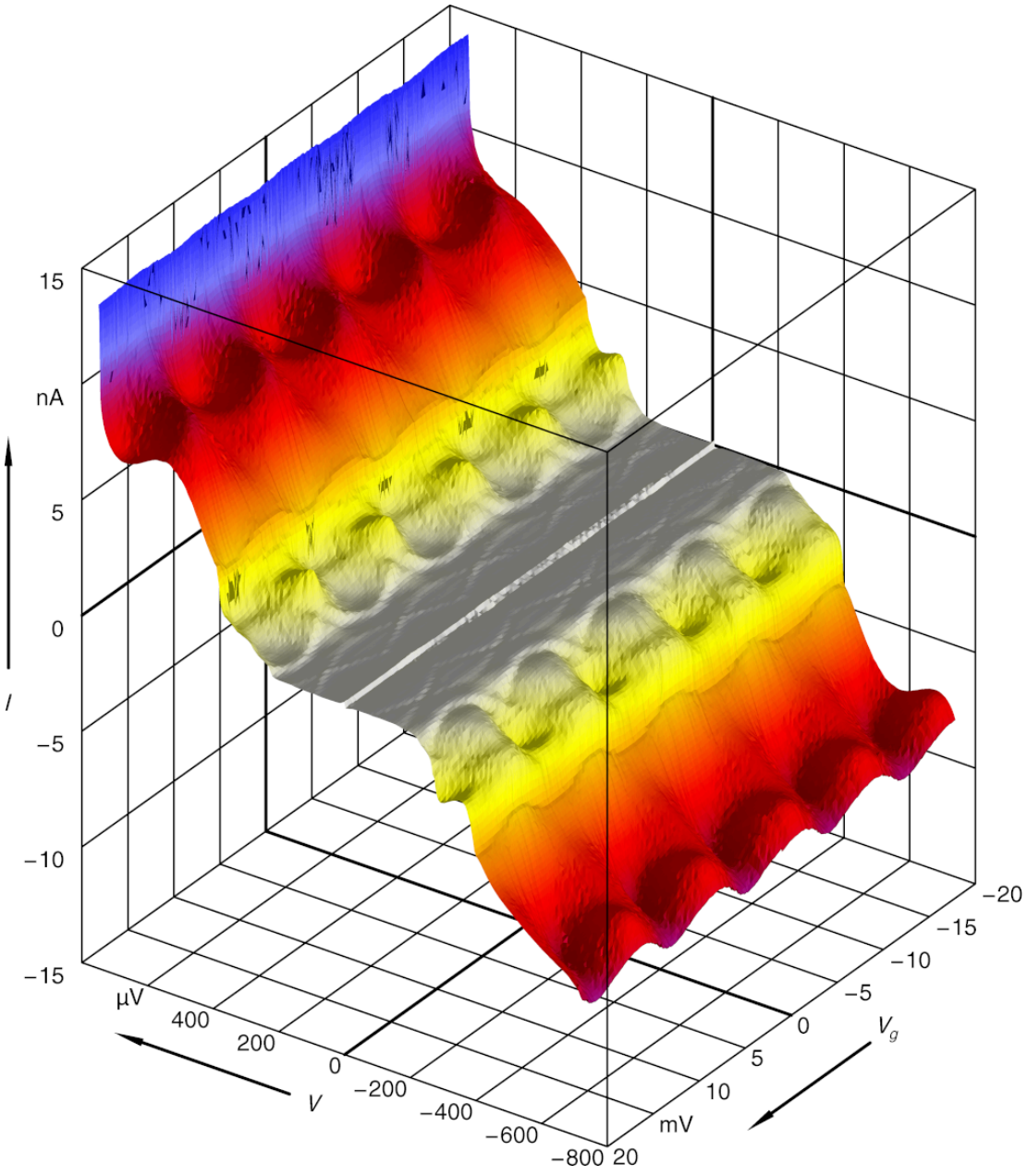


Figure 5.29: 3D plot of the measured current $I$ as a function of bias voltage $V$ and gate voltage $V_g$ for sample 94III.

The last sample of our measurement series comprises Pd/Au quasiparticle traps as well. The DJQP and JQP features have much in common with measurements presented on the last page. However, we do not see any trace of 2e periodicity behavior for this device. This fact is hard to explain. The most significant difference to sample 94I is an increased $\Delta/E_c$ ratio which should

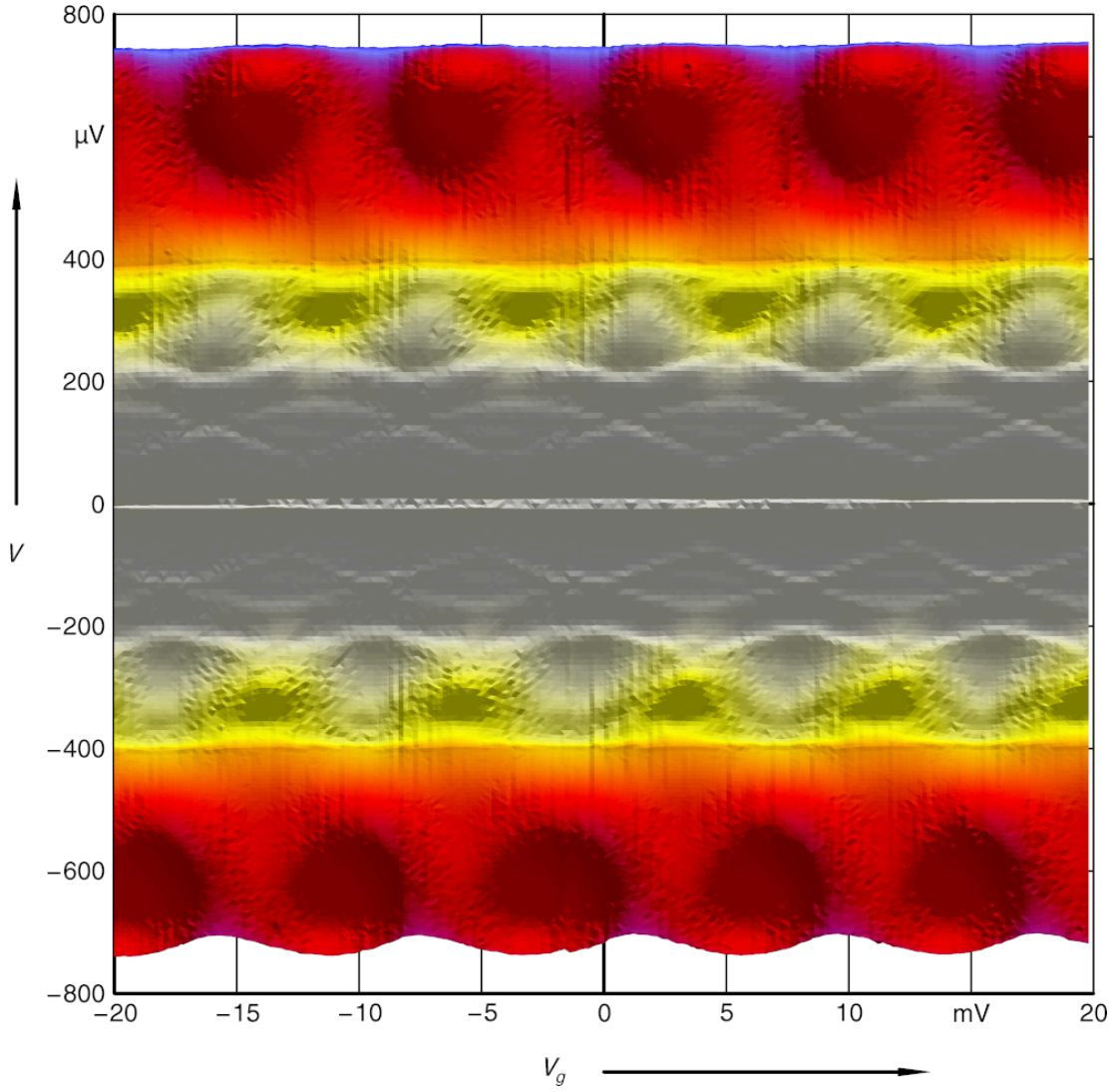


Figure 5.30: The same data as shown in Fig. 5.29 for sample 94III plotted in the 2-dimensional $V/V_g$-plane.

be in favor of 2e periodicity.

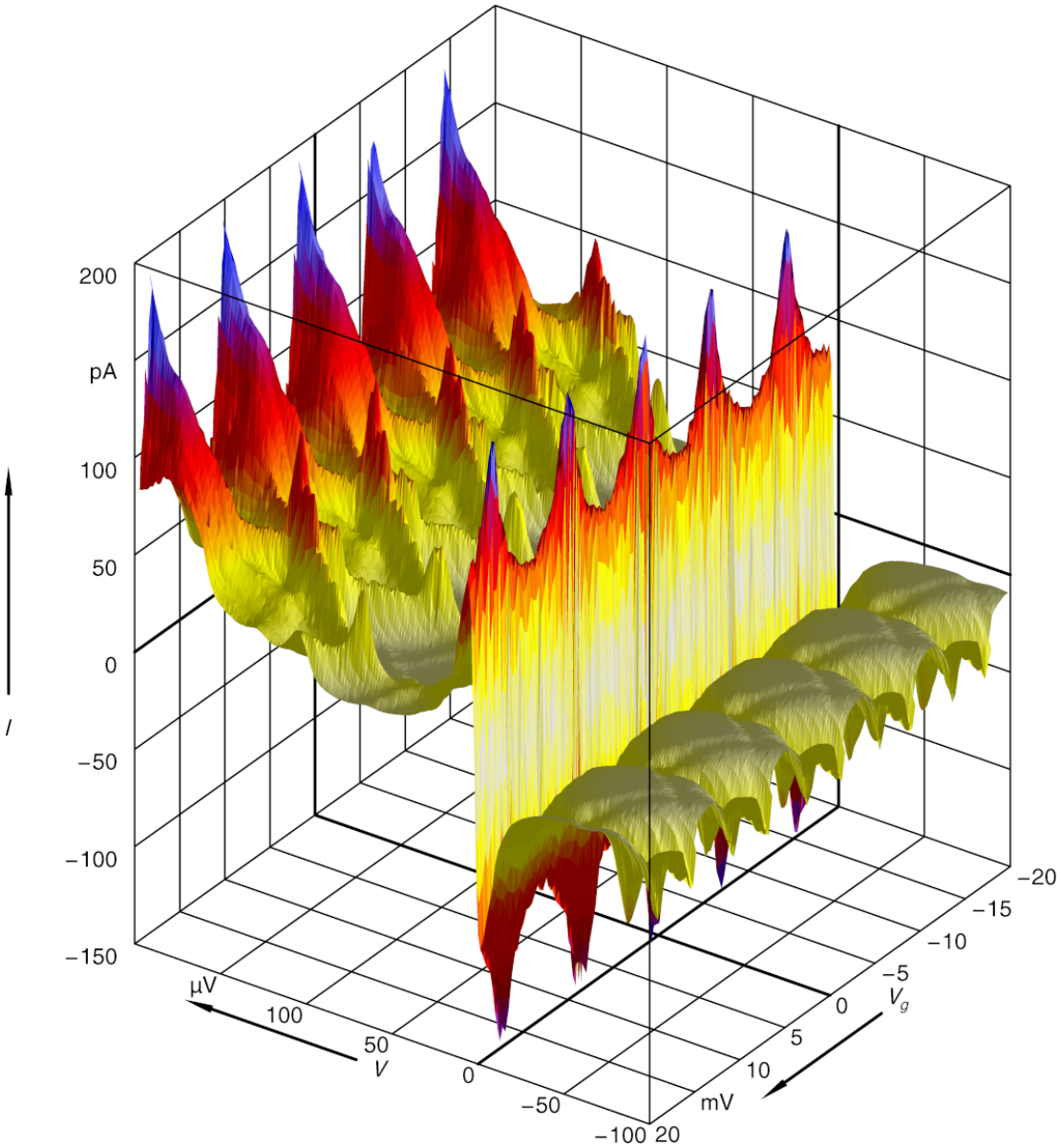


Figure 5.31: Another 3D plot of the measured current $I$ as a function of bias voltage $V$ and gate voltage $V_g$ for sample 94III.

The measurements presented in Fig. 5.31 focus on the RCPT features below the DJQP. In Fig. 5.32, the fifth order RCPT lines can be clearly identified. As the third order, it does not start at small biases, but rather at the first crossing. Note that the third order lines extend beyond the second crossing without any sign of getting weaker.

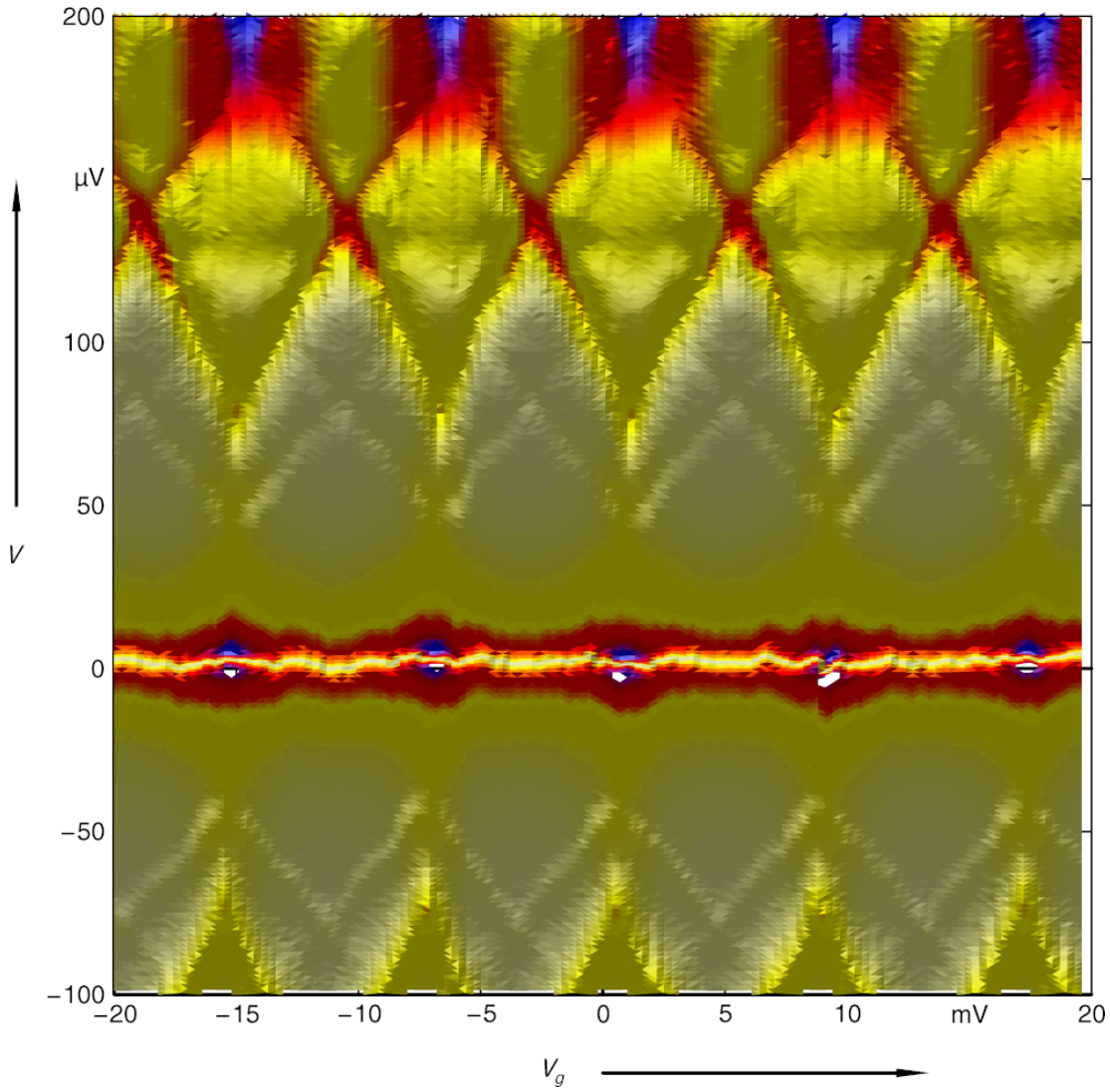


Figure 5.32: The same data as shown in Fig. 5.31 for sample 94III plotted in the 2-dimensional $V/V_g$-plane.

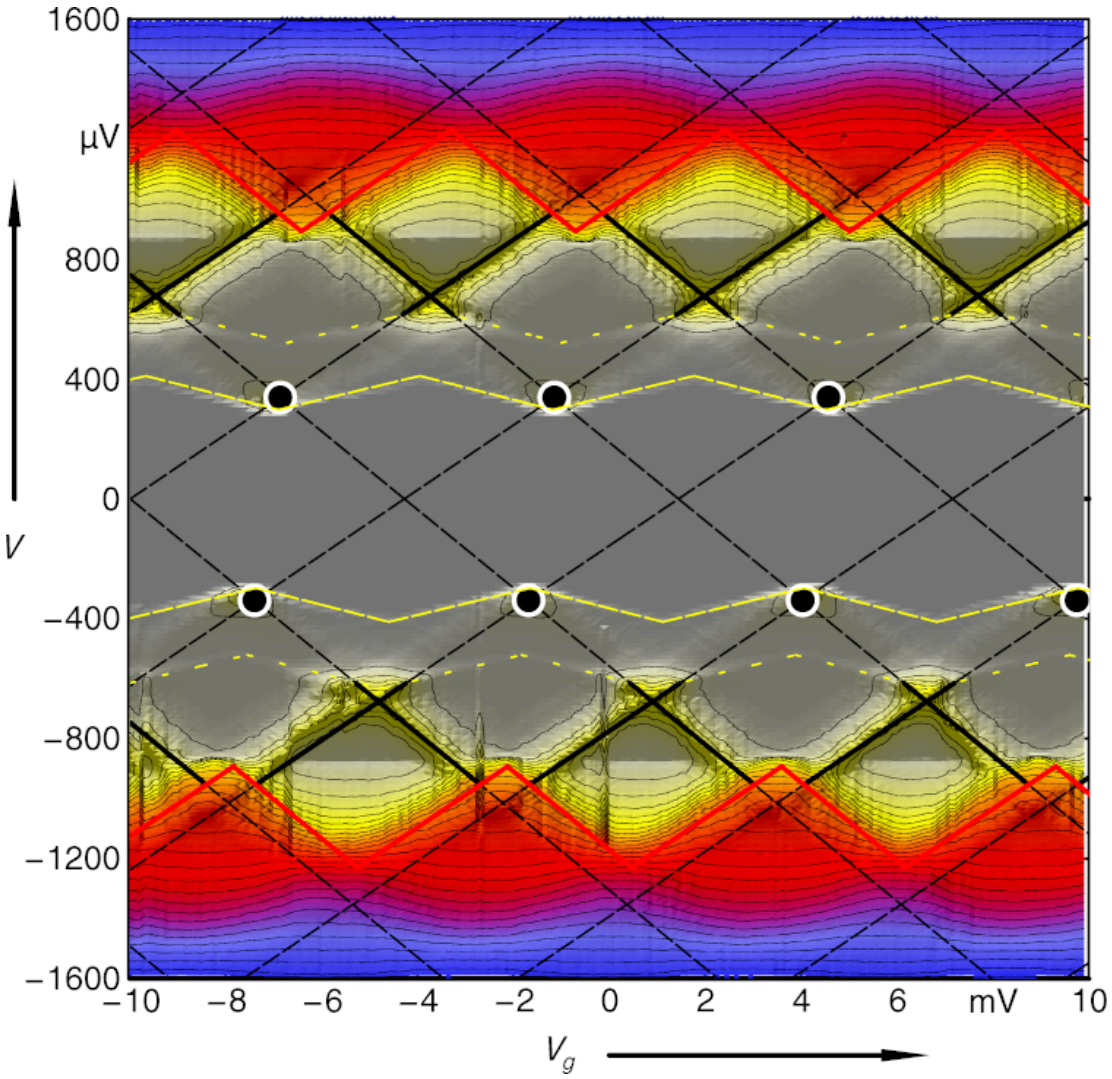


Figure 5.33: Color plot of the current features in the $V/V_g$-plane for sample 81III with the same experimental data already showed in Fig. 5.17. Lines representing theoretically expected positions are added on top of the color plot. Red lines are the thresholds for sequential quasiparticle tunneling. Black solid lines are the resonant positions for Josephson quasiparticle cycle. Yellow dashed lines are the thresholds for 3e tunneling process. Yellow dotted lines are also 3e process (see text). Large black dots show the positions for the DJQP. Black dashed thin lines are where first order resonant Cooper pair tunneling is resonant.

### 5.2.2 Discussion

In Sec. 5.2.1, we presented our experimental results in the finite voltage bias regime at the base temperature of our cryostat. All these samples have a very similar charging energy, except for

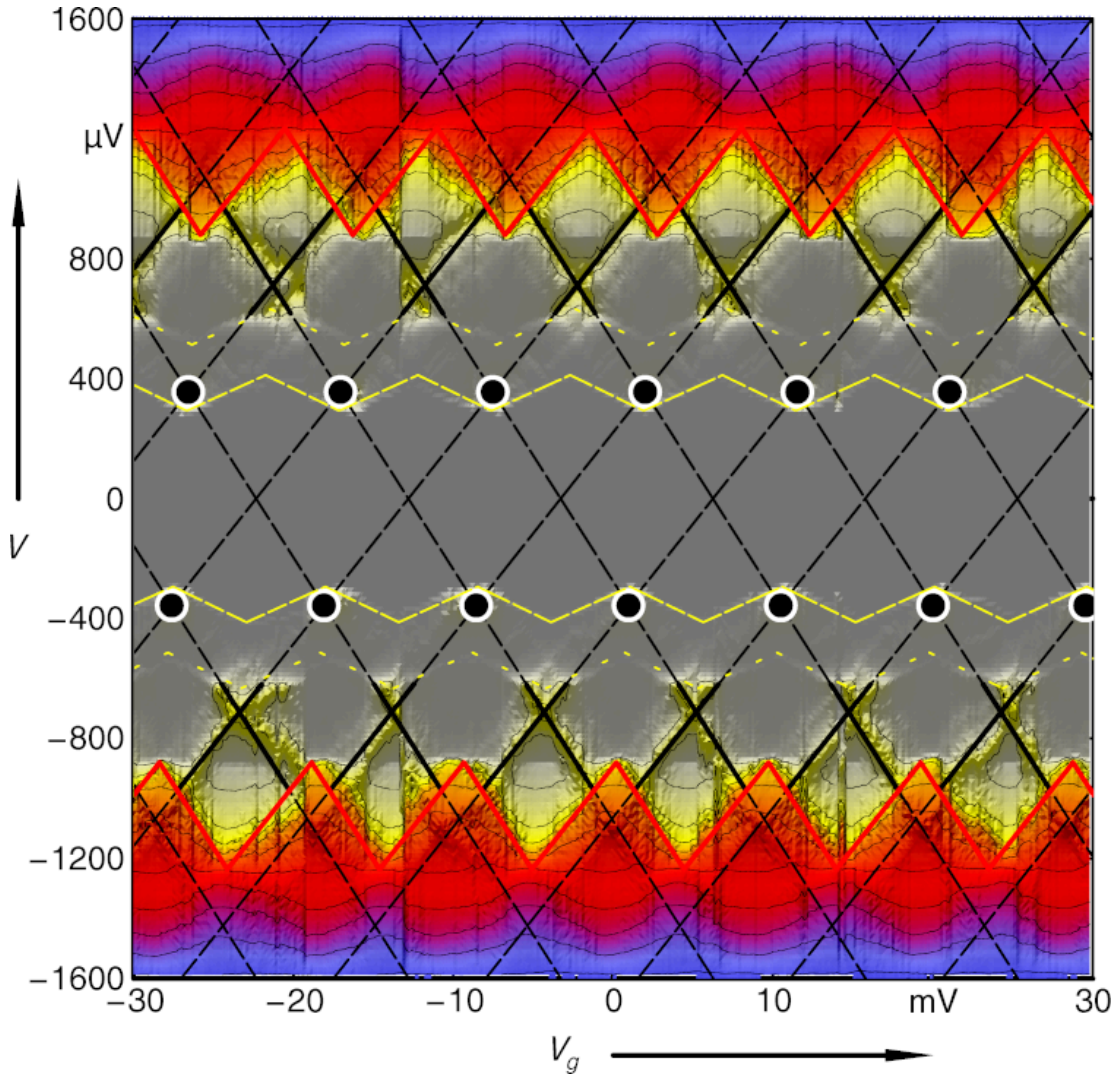


Figure 5.34: Color plot of the current features in the $V/V_g$-plane for sample 81II with the same experimental data showed in Fig. 5.13. Lines of different color and styles represent theoretically expected positions for different current features. They have the same meanings as in Fig. 5.33.

sample 73II which has larger tunneling contacts, resulting in larger capacitances and smaller tunnel resistances. In the following discussion, we do not consider this sample and focus ourselves of the main current features we have seen so far for all the other samples. The samples have charging energies $E_c$ ranging from 103μeV to 174μeV, the Josephson coupling energy differs from 4.55μeV to 26.1μeV. We group our samples into two types, one with large Josephson coupling and one with small Josephson coupling. The current characteristics of our voltage bias measurements are directly related to the charging energy $E_c$, the Josephson coupling energy $E_j$

and the superconducting energy gap $\Delta$.

As has been explained in Sec. 2.3.1.1 and shown in Fig. 2.13, the threshold voltage for single electron tunneling varies zigzag like between $4\Delta/e$ and $4\Delta/e + 2E_c/e$. In Fig. 5.33 and Fig. 5.34, we have superimposed this zigzag line in red with a measurement on sample 81III, which presents the data in the $V/V_g$-plane. This plane is the natural coordinate frame for measurements. It differs from the presentation in the $V/n_0$-plane by a shearing in $n_0$ direction which stems from the $n_0$ dependence on the bias $V$ (see App. A). The shearing has no influence on the bias position of the sub-gap current features. Clearly seen in Fig. 5.33 and Fig. 5.34 is an onset of current at $|V| = 4\Delta$ which is independent of $V_g$. This is due to the incoherent Cotunneling of quasiparticles, a process which preserves the island charge (Averin et. al., 1997).

In the voltage bias range below $|V| < 4\Delta/e$, many current features can be observed, a few of which are marked in Fig. 5.33 and Fig. 5.34 for samples 81III and 81II. Thick lines and singular black dots represents the JQP and DJQP which we observe for all our samples. Also marked is the 3e process with a dashed yellow line, which has been reported by many authors. The dotted yellow line on the other hand is new to us and surprising. It is clear from our measurements that between the higher bias crossing of the standard 3e process and the lower crossing of the dotted yellow line, no current feature aligned with the 3e resonance can be resolved. An abrupt current increase starts after a gap of $2E_c/3$. The onset at the lower crossing of the dotted yellow line is unexpected since the correspondence to non-adjacent states. At the time-being, this process is not well understood.

For sample 81III and 81II, the tunneling rate at the JQP cycle can be expressed by Eq. 2.18. Using this formula, we calculate the current peak at 670µV for sample 81III and achieve $I =$ 0.9nA. This value is completely consistent with the measured current which is around 1nA. This confirms the conclusions of earlier works (Nakamura et. al., 1996; Pohlen et. al., 2000). Samples with larger Josephson couplings do not show the well defined JQP peaks in the $V/V_g$-plane, see Fig. 5.20, Fig. 5.28 and Fig. 5.30. These samples have a larger Cooper pair tunneling rate and it is no longer bottlenecked by the Cooper pair tunneling. As far as we know, no theoretical model has been given for the calculation of the JQP current in the strong Josephson coupling regime yet.

In the voltage bias range from $2\Delta$ and $2\Delta + E_c$, there are several very small current features, as one sees from Fig. 5.34. These current features are due the singularity matching effect (Manninen et. al., 1997; Nakamura et. al., 1997). Our experiments are done at the base temperature of our cryostat so the number of thermally excited quasiparticles are quite small. Therefore, these thermally induced current features are nearly invisible.

For the samples with higher Josephson couplings, lines of enhanced current following higher order RCPT conditions are observed, as shown in Fig. 5.35. Dotted blue lines mark the rim of third order resonant Cooper pair tunneling currents which has a slope of one third the slope for JQP cycles, see Fig. 2.13. However, the appearances differ from what have been observed in earlier measurements of RCPT (Haviland et. al., 1994; Joyez, 1995). Both authors observe resonances down to the rims of the supercurrent branch. Our resonant feature sets on sharply at the first crossing of two adjacent RCPT resonant lines. It is worthwhile noting that the lines which cross at these onset points belong to different parities. To be definite, we consider the crossing point around $V$ =85µV and $V_g = -5$mV in Fig. 5.35a). The rim with negative

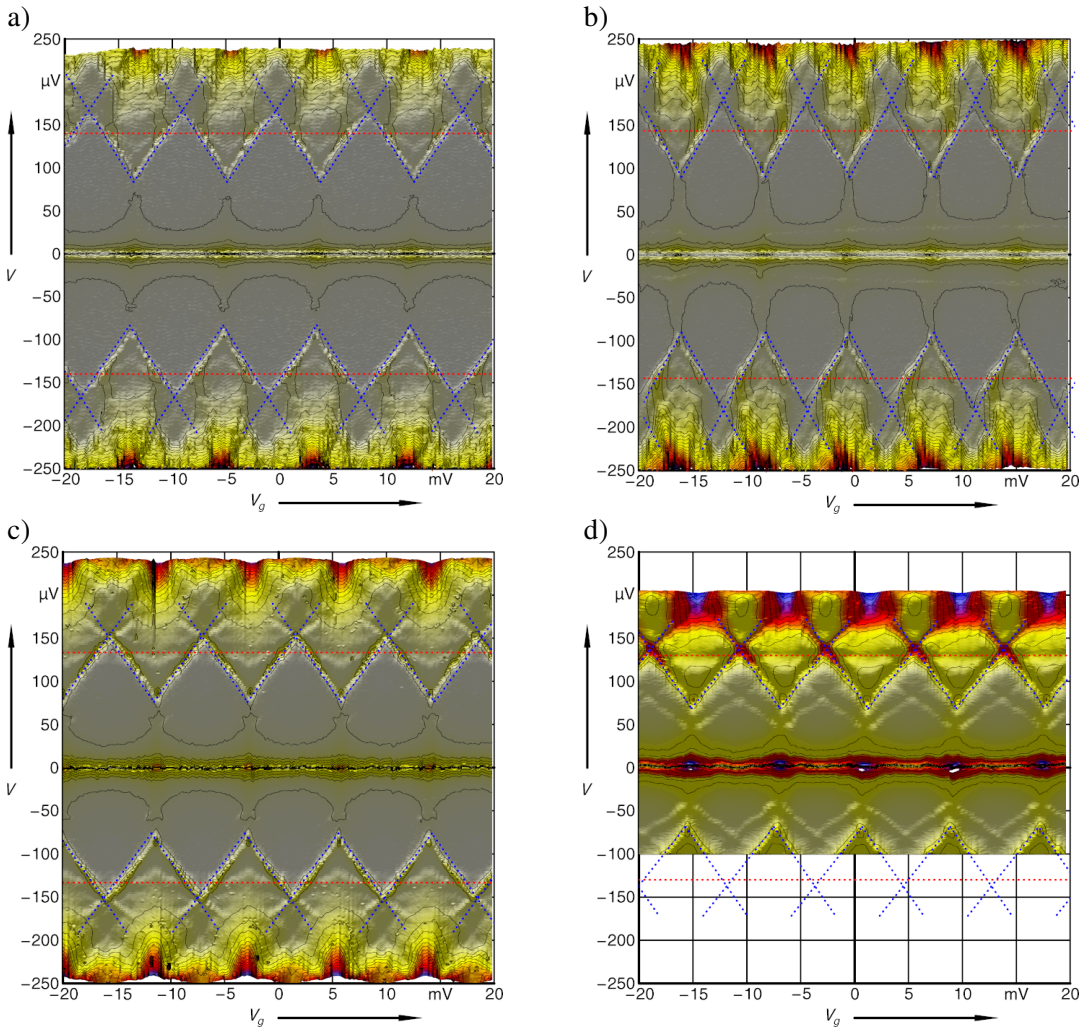


Figure 5.35: Color plots of the sub-gap current features in the bias voltage range from -250μV to 250μV for the same experimental data sets showed in a) Fig. 5.21 for sample 82IIIa; b) Fig. 5.23 for sample 82IVa; c) Fig. 5.25 for sample 82IVb; d) Fig. 5.31 for sample 94III. Red dashed lines are at the bias voltage $|V| = 2\Delta/3e$. Blue dashed lines are the positions for third order resonant Cooper pair tunneling.

slope ending here might correspond to the coupling of two adjacent Cooper pair states with even parity labeled by 0 and 2 excess electrons on the island. On the other hand, the rim with opposite slope corresponds then to the coupling of adjacent Cooper pair states with odd parity, labeled by -1 and 1 excess electrons. Josephson coupling does not mix states of different parity. So it is not obvious how the resonance condition underlying the first line can set a border for the onset of current carrying cycles along the other one.

## 5.3 Current bias measurements

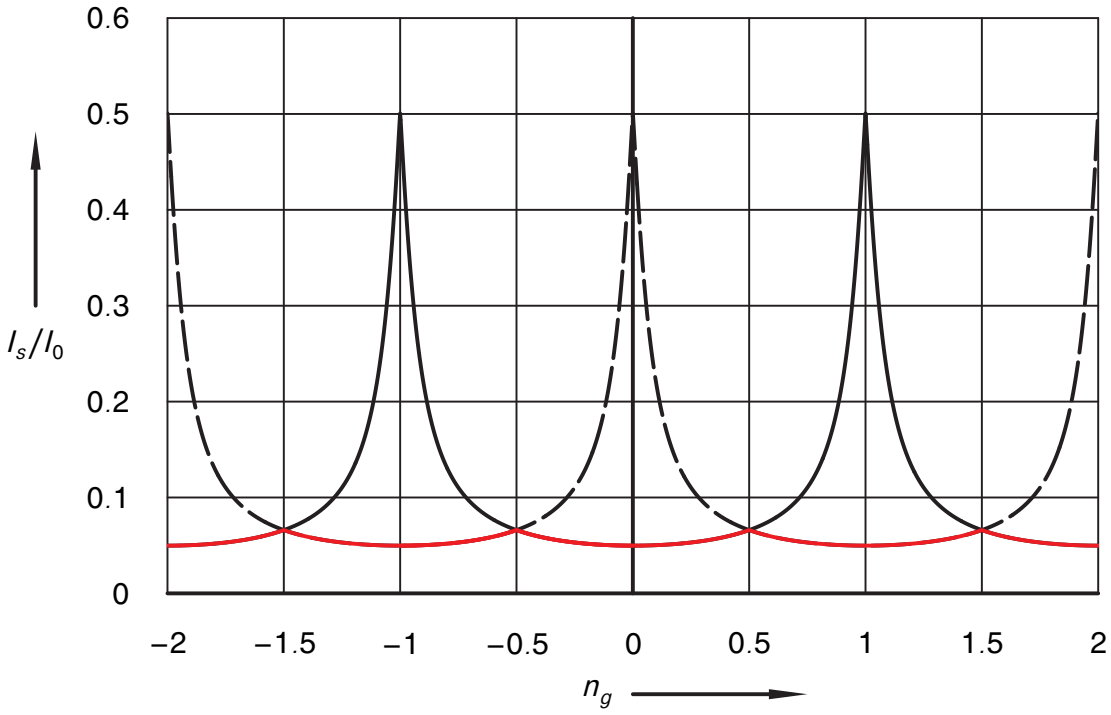


Figure 5.36: Sketch show e-periodic gate dependent switching currents. Black sold curve shows the switching current for pure even parity of the island. Black dashed curve shows the switching current for pure odd parity of the island. Red solid line shows the possible observed switching currents if both even and odd parities are present during one switching current event measuring round.

In this section, we will focus on the results with the current bias setup. We apply a voltage across a serial combination of a large bias resistor $R_b$ and the transistor and measure the resulting voltage drop across the transistor, see Fig. 4.2. The bias current is then $I_b = V_b/R_b$. In this setup, the transistor displays a hysteretic behavior when the current is cycled. When the current of the source is ramped from zero, the $IV$ characteristic first follows the superconducting branch, and then at a given value of the bias current, it suddenly switches to a finite voltage. The current at which it switches defines the switching current $I_s$. It is always considerably lower than the maximal supercurrent $I_0$, see section 2.2.

We have shown in section 2.3.2 that the switching current for a transistor behaves quite similar to a single Josephson junction, except for its gate dependent amplitude. We have presented numerical calculations of the critical current, modulated by the gate-induced charge $n_0$ and the $E_j/E_c$ ratio in Fig. 2.15. The gate-voltage modulation is 2e-periodic with respect to the gate charge $n_0$ in this plot. This 2e-periodicity originates from the even/odd parity asymmetry of the charge states on the island. The odd charge states are lifted above the superconducting energy

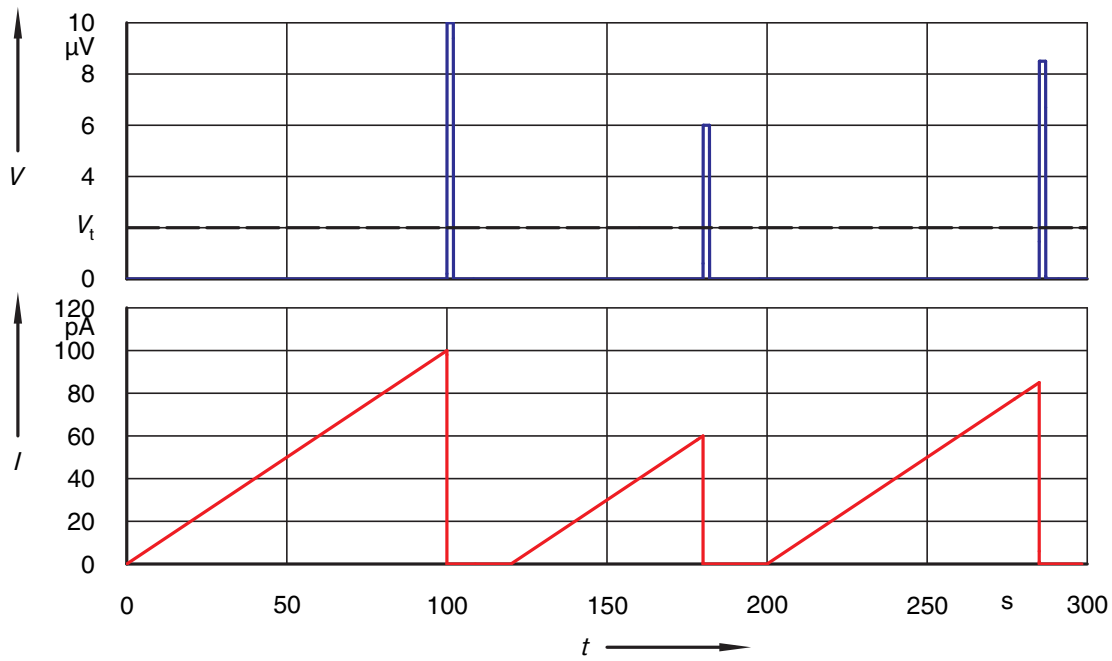


Figure 5.37: Sketch showing our ramping scheme for switching current measurement. Lower plot is the time dependent ramping current. Upper plot shows the triggering of the voltage across the single Cooper pair transistors. If the transistor switches to a voltage state, the bias current is recorded as the switching current and the bias current switches back to zero.

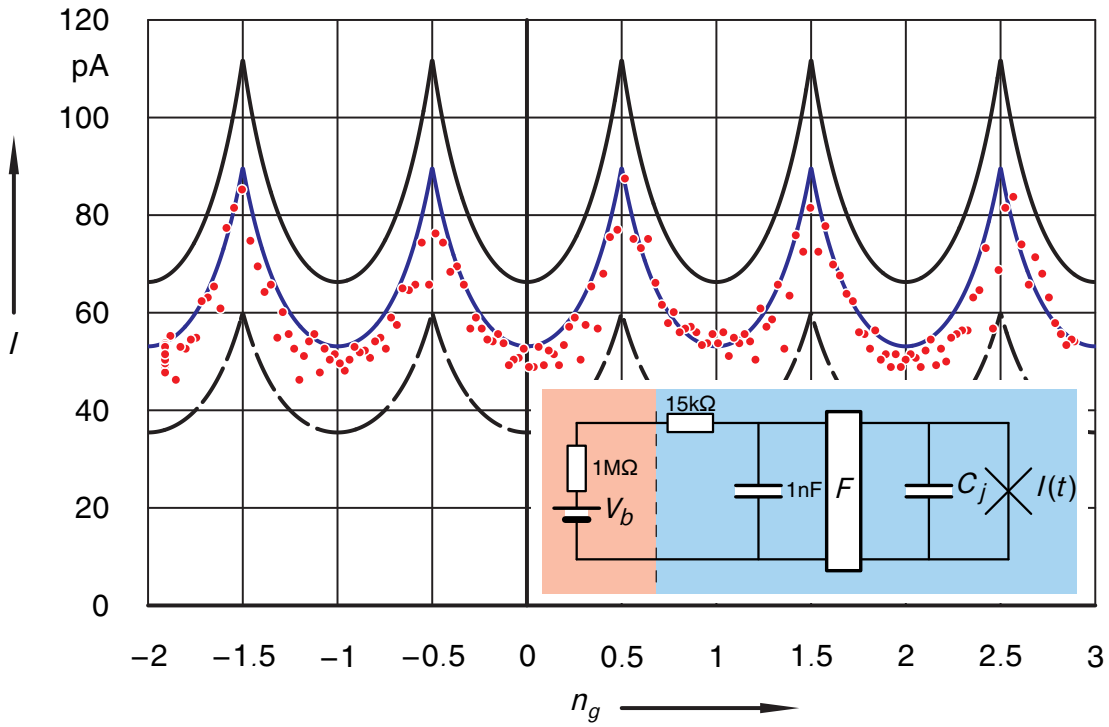


Figure 5.38: Switching current measured for sample 82IVb at 30mK nominal temperature with the bias resistor put in room temperature. Line in this plot shows the theoretical switching current curves obtained within the large friction regime of Josephson junctions. Top to bottom of the three curves shows the switching current for 160mK, 200mK and 300mK. Inset shows the measurement circuit.

gap for the CPT. If the charging energy $E_c$ is smaller than the superconducting energy gap $\Delta$, only even parity states survive on the island, leading to the 2e behavior.

In our sample parameter range, the charing energy is around 150μeV, which is only slightly under the superconducting energy gap $\Delta$ of Aluminum, which is around 200μeV. This slight energy difference leads to the susceptibility of odd parity charge states on the island, see Sec. 2.3.3. As is shown in Fig. 5.36, the odd parity critical current is the same as the even parity critical current but with the gate modulation shifted by one single charge. In the switching current experiments, the availability of both even and odd states leads to two possible switching current values. And it is clear that for slow measurements only the lower switching current can be observed, shown in red curve in Fig. 5.36.

Fig. 5.37 shows the sketch for our switching current measurement. The bottom plot in Fig. 5.37 shows the linear ramping of bias current at a rate of 1pA/s. As the current increases, the transistor follows the supercurrent branch until it suddenly switches to finite voltage state. This switching event is triggered by a voltmeter with a triggering threshold $V_t$, see the upper plot in Fig. 5.37. Then the voltmeter feeds back this event to the current source and the bias

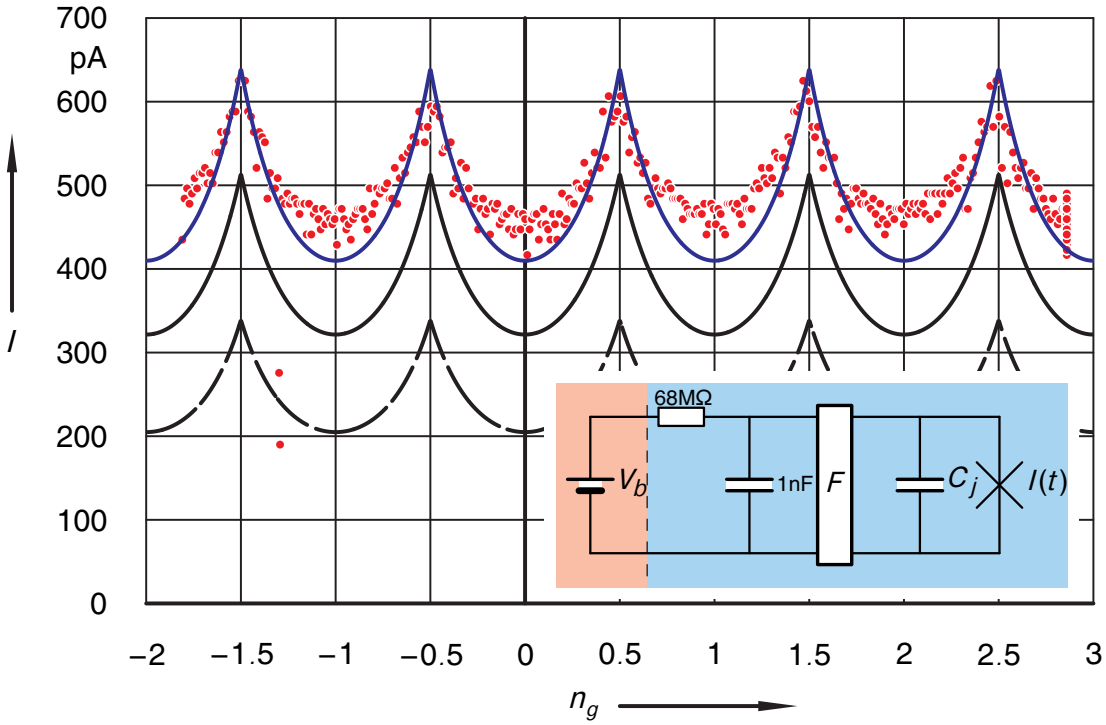


Figure 5.39: Switching current measured for sample 82IVb at 30mK nominal temperature with a 68MΩ bias resistor put in the mixing chamber. Lines in this plot show the theoretical switching current curves obtained within the large friction regime of Josephson junctions. Top to bottom of the three curves shows the switching current for 22mK, 50mK and 100mK. Inset shows the measurement circuit.

current switches to zero. It stays for some seconds at zero bias current to relax the circuit and then restarts the repetition again.

Fig. 5.38 and Fig. 5.39 shows the switching current for sample 82IVb. This sample has three connecting wires to the room temperature setup. One line serves as a common ground. The two other lines on the other side of the transistor are equipped with resistors of 15kΩ and 68MΩ at the mixing chamber. The latter resistor is actually a $RuO_x$ resistor with a strong temperature dependent value. It was chosen by accident since it was marked wrongly as metal sheet resistor. Only at low temperatures, we discovered its semiconductor-like resistance behavior. In addition, the sample was shunted by a 1nF capacitance which together with the resistances forms *RC* filters. We conducted two different measurements of the switching current with this setup. First we put a 1MΩ resistor at room temperature in series with the cold 15kΩ resistor, using this line for the current bias. The voltage drop was monitored between the common ground and the low temperature 68MΩ resistor. The bandwidth of the biasing line is given by $1/(2\pi RC) \sim 10$kHz. The results are shown in Fig. 5.38 as red dots. The lines in the figure represents numerical evaluations of the switching current according to Eq. 2.26 for different

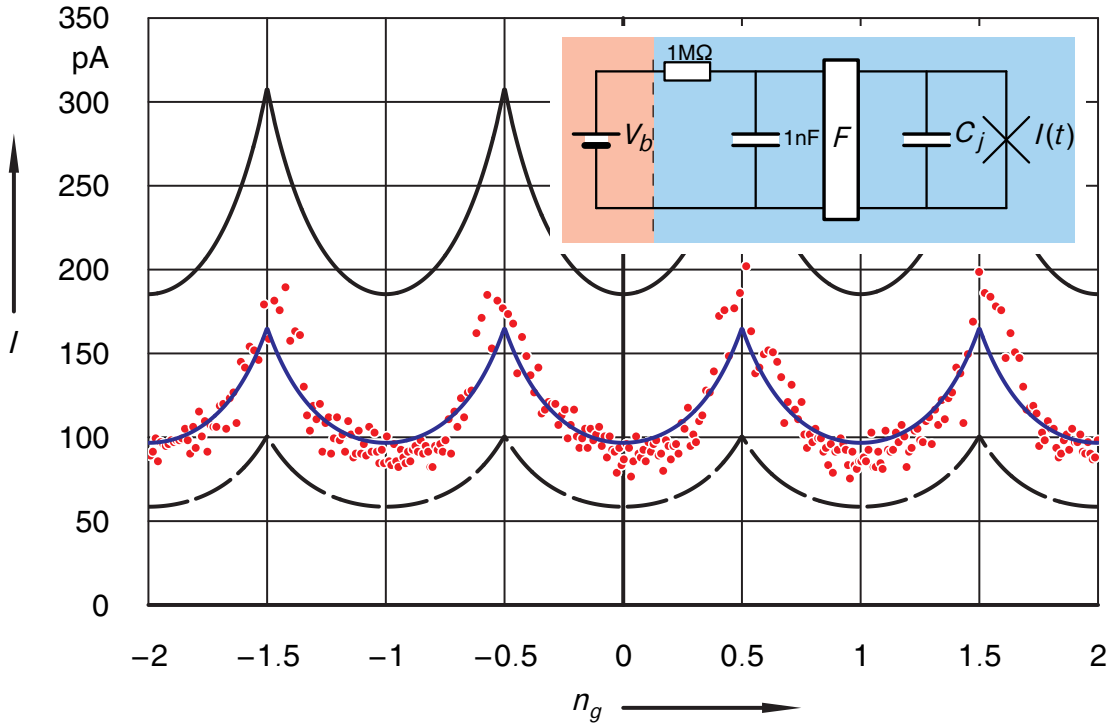


Figure 5.40: Switching current measured for sample 94I at 30mK nominal temperature with 1MΩ bias resistor put in the mixing chamber. Lines in this plot show the theoretical switching current curves obtained within the large friction regime of Josephson junctions. Top to bottom of the three curves shows the switching current for 30mK, 60mK and 100mK. Inset shows the measurement circuit.

temperatures. Eq. 2.26 is applicable whenever the quality factor $Q$ is much smaller than 1 which means an overdamped situation for an Josephson junction. From Tab. 5.1, we find for sample 82IVb $E_c/E_j = 2.27$ which allows us to calculate: 1.3μeV< $E_0(n_0)$ < 1.5μeV. The effective capacitance of our circuit is dominated by the stray capacitance rather than the junction capacitances and is not well known. We estimate it to be not larger than 100fF. For the plasma frequency, this means $\omega_p = (2\pi/\Phi_0)\sqrt{E_j/C}$ is of the order of 4GHz. Then the quality factor is of the order of $Q = RC\omega_p \approx 0.04$, where we have taken $R = 100\Omega$ to be the AC resistance at plasma frequency. This justifies to use Eq. 2.26.

Our experimental result shown in Fig. 5.38 is best fitted with an effective temperature as high as 200mK which is well above the temperature as measured by resistive thermometry. The situation is much more different in Fig. 5.39. In this case, we use the 68MΩ resistor for current biasing the sample and monitor the voltage drop between the cold 15kΩ resistor and the common ground. The bandwidth of the current bias has been reduced to 2Hz. At the same time, the switching current is almost a factor of 10 larger, corresponding to an effective temperature of around 22mK, in good agreement with the resistive thermometry. In Fig. 5.39, we see

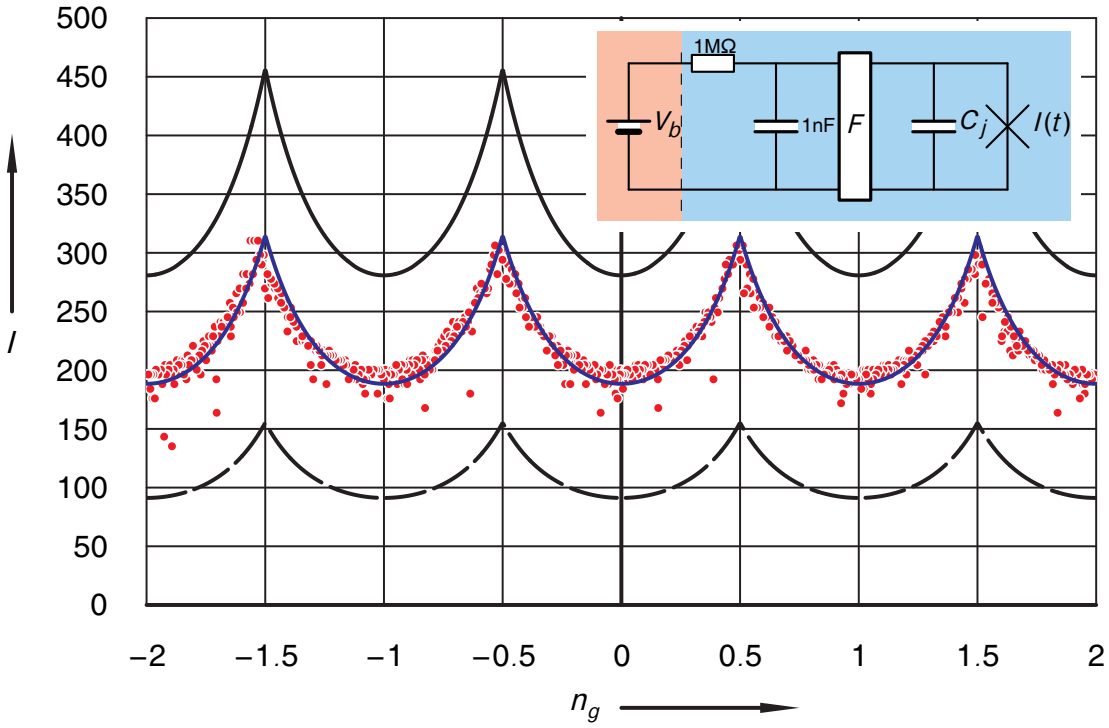


Figure 5.41: Switching current measured for sample 94II at 30mK nominal temperature with 1MΩ bias resistor put in the mixing chamber. Lines in this plot show the theoretical switching current curves obtained within the large friction regime of Josephson junctions. Top to bottom of the three curves shows the switching current for 30mK, 47mK and 100mK. Inset shows the measurement circuit.

slight deviations between the red dots and the fitting curve which we attribute to a temperature variation of the $RuO_x$ biasing resistor due to self-heating. Since the switching current is gate-dependent, the self-heating varies with $n_g$ as well. This effect is hard to quantify but might held responsible for the observed deviations.

In summary, we find from the measurements on sample 82IVb that the observed switching current depends strongly on the low frequency noise filtering. We reach the theoretically expected height, but only when we cut the bandwidth well below 50Hz which is the critical frequency for noise pickup.

In further measurements, we replaced the $RuO_x$ resistor with a proper metal sheet resistor of 1MΩ. This cuts the bandwidth together with the 1nF capacitance down to 160Hz. We did not choose a higher resistance firstly because the low bandwidth leads to extreme requirements for the measurement time, secondly excessively high resistances in the current path at the mixing chamber can lead to considerable self-heating. Fig.5.40 and Fig. 5.41 depict measurements on two different samples 94I and 94II on the same chip.

The effective temperature fitted with the same procedure is now higher (47mk and 60mK,

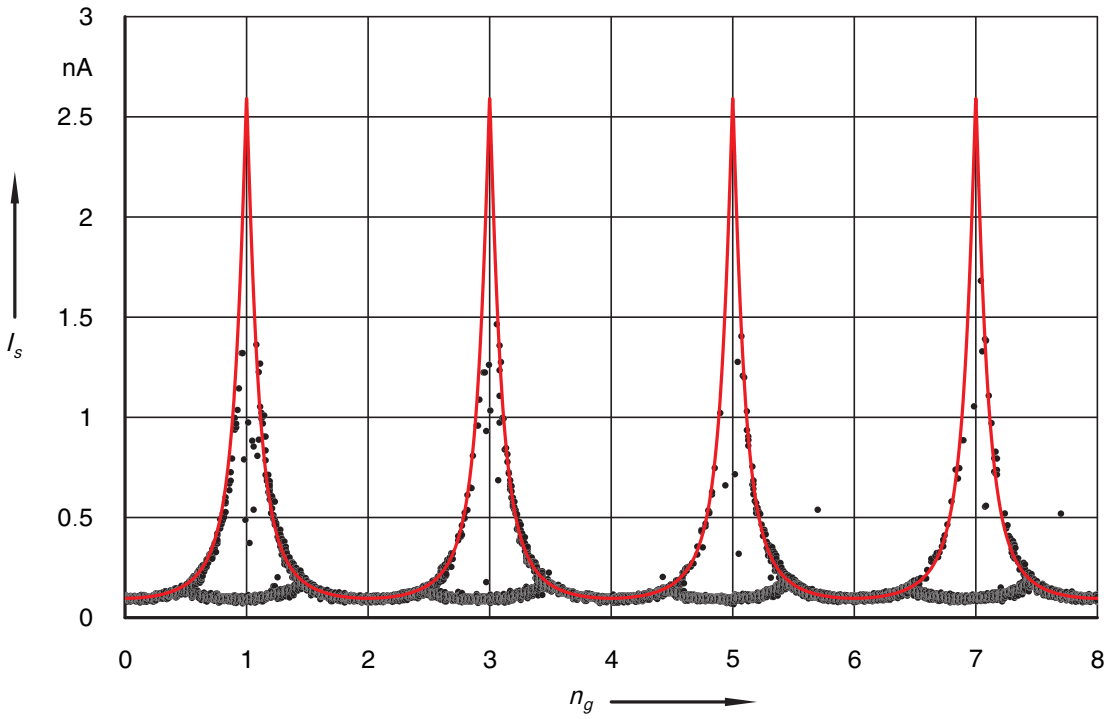


Figure 5.42: Switching current of sample 94I with the same circuit as the measurement shown in Fig. 5.40. These switching current data are collected with a ramping speed of 3nA/s, shown in black dots. Red curve shows the theoretical expected switching currents at 60mK.

respectively), showing that the filtering is not as efficient as before with the $RuO_x$ resistor. With respect to the option to record more switching events in a reasonable time, this filtering strength represents a good compromise. Further optimization will require to put the experiment in a better shielded environment. The difference in effective temperature might be due to the slight different performance of the measurement lines which enter the transistor. We are not using twisted pair cooper powder filters in these measurements because we do not have enough of them to wire all the samples on a single chip. Thus the loop size formed by the measurement lines might be different resulting in different amount of electromagnetic noise pickup.

With a ramping rate of only 1pA/s, it takes hundreds of seconds to reach the switching current. During this long time, any spurious quasiparticle breaks the even parity and leads to e-periodic switching. In order to lower the risk of quasiparticle poisoning, we changed to a fast ramping method which is done by an arbitrary waveform generator. The ramping speed is only limited by the bandwidth of our *RC* filters; several nA per second can be reached. Fig. 5.42 shows the switching current measurement on sample 94I with a ramping speed of 3nA/s. It gives us clear 2e-periodic modulation behaviors although the odd states are still quite pronounced close to the gate ranges where $n_g$ =odd numbers. Since the wiring for this measurement is the same as the measurement shown in Fig. 5.40, the sample is also in the strong

damping regime. By fitting the measured current with the strong damping model, we get the effective temperature again 60mK which is quite consistent with the slow ramping measurement.

### 5.3.1 Discussion

In this section, we showed our measurement results of the switching currents for single Cooper pair transistors, sample 82IVb, sample 94I and sample 94II. All of the measurements are done in the strong damping regime. It has been shown by measurements on sample 82IVb that the bias resistor $R$ has a tremendous effect on the switching current amplitude. The room temperature 1MΩ resistance yields a maximum switching current below 100pA while the low temperature 68MΩ bias resistance gives a maximum switching current of around 650pA. We assume this behavior to be a result of an effective bandwidth cutoff of low frequency noises which might reach the sample and lead to an elevated effective temperature. Within the strong damping regime, the effective temperature with the 1MΩ room temperature resistor is as high as 200mK while the effective temperature for its low temperature counterpart is only 22mK, calculated with the strong damping model. This reminds us that using only high frequency cooper powder filters is not sufficient for such sensitive measurements, further filtering stages such as the simple RC filter stage are needed for effective damping of lower frequency noises, as has been suggested by Bladh et. al. (2003). Measurements on the later two samples 94I and 94II are done with 1MΩ low temperature filters. The switching current fits also pretty well with the strong damping regime and yields an effective temperature below 60mK. Our measurement confirms that the single Cooper pair transistors can be considered as single junctions with gate modulated switching currents. We used the lowest eleven states for calculating our theoretical expected switching current values.

Both slow ramping with an ramping rate of 1pA/s and relatively fast ramping with a ramping rate of 3nA/s are used for obtaining the switching currents of our samples. No 2e gate dependent features have been observed by the slow ramping scheme. It normally takes hundreds of seconds to reach the switching current. This makes the switching event quite vulnerable to the quasiparticle tunneling events which might happen at a smaller time scale. Because of the unexpected quasiparticle tunneling events, the island has both even and odd states available for one single round of switching current measurement. Therefore only the first switching event can be recorded which leads to an e-periodic gate modulation of the switching current. We have shown in Fig. 5.36 in red lines the part of the switching currents which can be observed in such a very slow ramping scheme.

Fast ramping measurement was done on sample 94I. And 2e-periodically gate modulated switching current has been first observed. The magnitude of these switching current fits very well with the strong damping regime for single Josephson junctions, verifying the validity of this model. The effective temperature achieved with the fitting is 60mK which is a bit higher than the base temperature of our cryostat. This discrepancy might be induced by the argument of the so-called "hot electrons", that is, electrons carry higher thermal fluctuations. We haven't got pure 2e switching current for this measurement for this sample which means that odd parity states are still quite prevalent on the island.

Our samples have large charging energy $E_c$, making them quite vulnerable to the quasiparti-

cle poisoning. Besides lowing the charing energy, several other methods have be proposed by several groups. These proposals can be grouped into two types: one is to damping the quasiparticle excitations, e.g. using normal metal quasiparticle traps close to the island (Joyez, 1995), and another one is the so-call superconducting energy band engineering. There are mainly two ways of energy band engineering methods so far, one is to induce defects on the aluminum film by letting in a little bit oxygen during aluminum evaporation while forming the middle island. This method has been extensively used by Aumentado et. al. (2004) and worked quite well to suppress the odd parity states on the island. Another way is to fabricated thinner films for the aluminum island. This can also increase the superconducting energy gap of the island aluminum as proposed by Ferguson et. al. (2006). However, both methods do not eliminate the spurious quasiparticles.

In short, the mechanism for quasiparticle excitations which leads to odd parities on the island is not clear yet. Fig. 5.43 shows the gate dependent switching current for different ramping speeds. It can be seen that quasiparticle poisoning is even more severe at the gate voltage range from -6mV to 4mV. This gate dependent smearing of the imbalance between odd and even parities is not understood for us and we have not found any similar effects in the literatures.

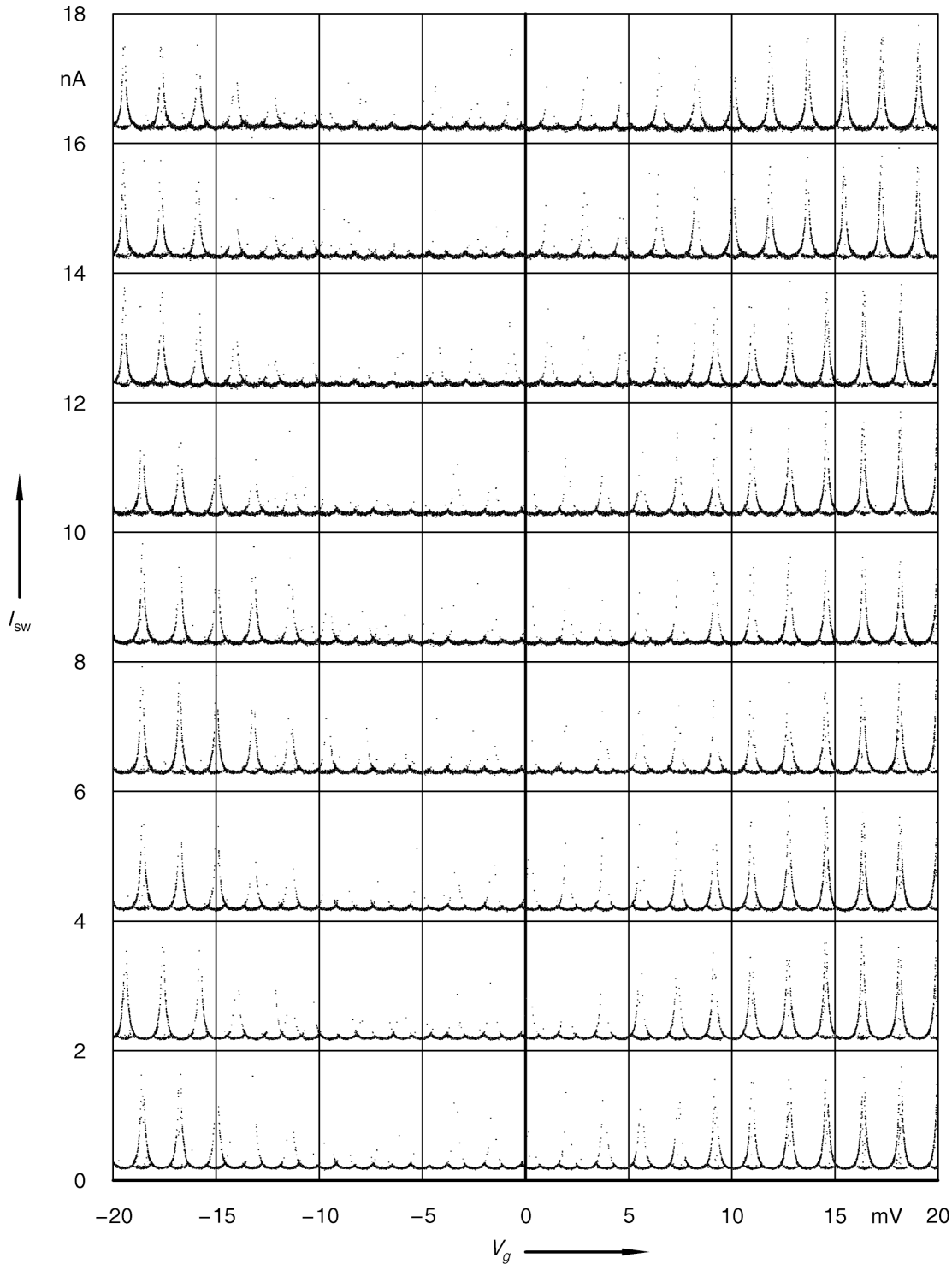


Figure 5.43: Switching current of sample 94I at 30mK nominal temperature as a function of gate voltage for different ramping speeds. From bottom to top: 3nA/s, 4.5nA/s, 6nA/s, 12.5nA/s, 15nA/s, 17.5nA/s, 20nA/s, 22.5nA/s, 25nA/s.

# 6 Conclusion

This thesis has focused on the experimental study of charge transport features in superconducting single electron transistors. The samples have been mainly fabricated in the Institute of Solid State Physics (IFP) with the access to the SEM in the Institute of Nanotechnology for the electron beam writing. The leads of the transistors have been made from a bilayer of copper and gold by optical lithography and the finer structures done by two subsequent electron beam lithography processes. With our fine alignment procedure a precision of 50nm has been reached for the required matching of the structures fabricated in different electron beam lithography steps. The samples have been measured in a $^3$He/$^4$He cryostat with a base temperature of 20 mK with which the thermal fluctuations will not mask the single charge transport effects. We have done the noise filtering by implementing $\pi$-filters at room temperatures and at low temperatures $RC$ filters and home-made metal powder filters. The efficiency of the copper powder filters at frequencies $f > 1$GHz is characterized by single electron transport experiments. RC filters are necessary for canceling low frequency noise.

Most of the observed transport properties of the superconducting single electron transistor are in good agreement with the theoretical expectations and earlier experimental works on this subject. For voltage bias above $|eV| > 4\Delta$ charge transport is dominated by pair-breaking quasiparticle processes. For not too strong Josephson coupling strength, a gate-modulation of quasiparticle current onset between $|eV| = 4\Delta$ and $|eV| = 4\Delta + 2E_c$ is observed. Below $4\Delta$, rich variety of current features due to combination of processes involving resonant Cooper pair tunneling, quasiparticle tunneling and cotunneling have been found. Most of these features have been described earlier by other authors.

3e tunneling comprising of the coherent tunneling of a Cooper pair across one junction and a quasiparticle across the other one is observed at the expected position in the $V/V_g$-plane. It can be easily identified as a higher order process by the difference in slope from most other features. Besides this expected feature, we find a further 3e line at a shifted bias position. The origin of this line has yet to be identified.

Samples with high transparencies show further features below the ordinary 3e line in bias. They lie on top of the condition for higher order resonant Cooper pair tunneling. Remarkably, these features end at crossings marked by lines belonging to states of different parities. For two of our samples, the third order feature of this type is also bordered sharply on the higher bias side, thus giving a zigzag feature as a function of $V_g$. For two further samples, the lines continue, showing in one case no sign of a reduction in current size. The mechanism for switching the resonances on and off at these specified bias voltages is unknown at present. One sample shows fifth order features with similar properties.

The switching currents for some of our samples have also been measured. Most of them show $e$-periodic dependence on the gate. For a later sample with improved quasiparticle filtering, 2e features have been observed. However, it is clear from our data that non-equilibrium

quasiparticles are still present at low rates. This observation is in agreement with investigations by other authors. Fitting the current values by considering the transistor as a single Josephson junction with a gate-dependent Josephson coupling yields an effective temperature which depends strongly on the low frequency filtering. By reducing the bandwidth of the leads to 2Hz, we could achieve a temperature as low as 22mK which is in agreement with the temperature measured by our resistive thermometry. An effect which deserves further attention is the gate dependence of the parity effects.

# Appendix A

# The electrostatics of SET devices

We consider the system of island depicted in Fig. A.1. By the usual definition of the various capacitances we have:

$$Q_1 = C_{12}(U_1 - U_2) + \sum_{i=2}^{N} C_{1i}(U_1 - U_i) + \sum_{i=1}^{m} C_i^1(U_1 - V_i) = U_1 C_{\Sigma 1} - \sum C_{1i} U_i - \sum C_i^1 V_i,$$

with $C_{\Sigma 1} = \sum_j^n C_{j1} + \sum_j^m C_j^1$. And similarly:

$$Q_j = U_j C_{\Sigma j} - \sum C_{ji} U_i - \sum C_i^j V_i, \quad C_{\Sigma j} = \sum_i^n C_{ji} + \sum_i^m C_i^j.$$

In Matrix notation this reads simply $\boldsymbol{Q} = \boldsymbol{C}\boldsymbol{U} - e\boldsymbol{n}_0$. The capacitance matrix $\boldsymbol{C}$ is defined by $(\boldsymbol{C})_{ii} = C_{\Sigma i}$ and (for $i \neq j$) $(\boldsymbol{C})_{ij} = -C_{ij}$. $\boldsymbol{Q}$ and $\boldsymbol{U}$ are vectors indexed by the island number, and the so called "offset charge vector" $\boldsymbol{n}_0$ is defined by $(\boldsymbol{n}_0)_i = \frac{1}{e}\sum_j^m C_j^i V_j$. Note that $(e\boldsymbol{n}_0)_i$ equals minus the charge on island $i$ if all island are grounded[1]. The relation for $\boldsymbol{Q}$ can be inverted to yield

$$-e\hat{\boldsymbol{C}}\Delta\boldsymbol{n} = \boldsymbol{U}. \tag{A.1}$$

Here, $\hat{\boldsymbol{C}}$ is the inverse of $\boldsymbol{C}$ and $\Delta\boldsymbol{n} = \boldsymbol{n} - \boldsymbol{n}_0$, $\boldsymbol{n} = \boldsymbol{Q}/-\boldsymbol{e}$. The charging energy is a function of $\boldsymbol{n}$, $E_{\mathrm{ch}}(\boldsymbol{n})$. We choose the zero of energy accoding to $E_{\mathrm{ch}}(-\boldsymbol{n}_0) = 0$. The charging energy can be calculated by evaluating the following integral:

$$\begin{aligned} E_{\mathrm{ch}}(\boldsymbol{n}) = &\int_{-en_{01}}^{-en_1} \mathrm{d}Q_1 U_1(Q_{i\neq 1} = -en_{0i}) + \\ &\int_{-en_{02}}^{-en_2} \mathrm{d}Q_2 U_2(Q_1 = -en_1, Q_{i>2} = -en_{0i}) + \\ &\cdots + \\ &\int_{-en_{0n}}^{-en_n} \mathrm{d}Q_n U_n(Q_{i\neq n} = -en_i). \end{aligned} \tag{A.2}$$

In this expression we start from the condition at zero energy and put succesively the required charge on the islands starting with island number 1 and ending on island number $n$. Eq. A.2

[1] In the following we use the definitions $n_{0i} = (\boldsymbol{n}_0)_i$ and $n_i = (\boldsymbol{n})_i$

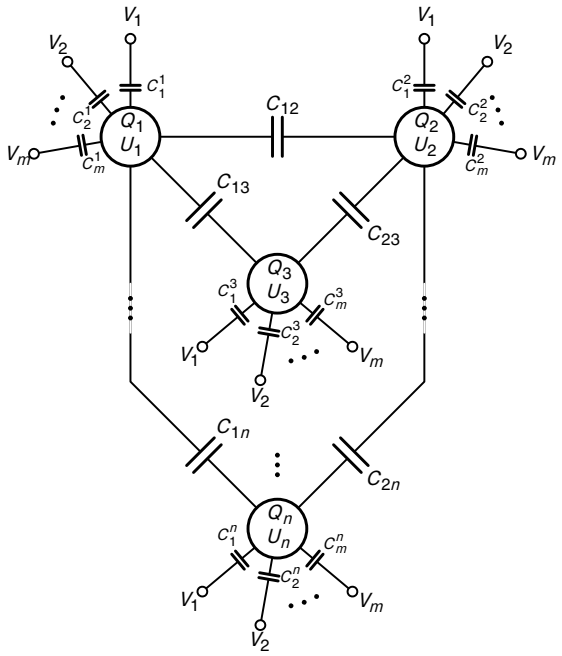


Figure A.1: A system of $n$ island (symbolized as big circles) capacitively coupled among each other and to $m$ reservoirs (symbolized as voltage sources $V_j$). Each island is charged by $Q_i$ and at an electrostatic potential $U_i$.

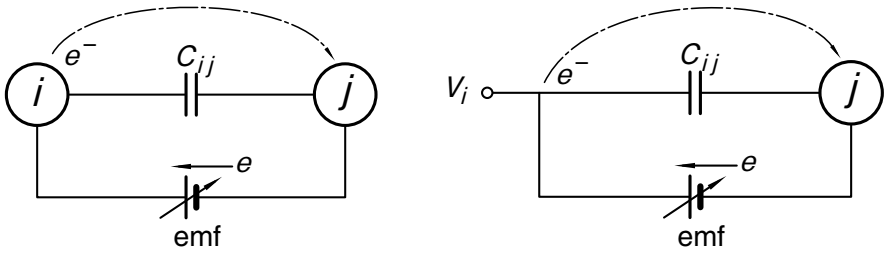


Figure A.2: To calculate the energy consumption of an tunneling event, we connect an emf across the capacitance. The emf is modeled as tunable battery. The voltage of this battery is tuned from an initial to a final condition to force a charge $e$ from one side to the other. Left: Tunneling across an internal capacitance. Right: Tunnling from a reservoir across an external capacitance.

gives in the end:

$$E_{\mathrm{ch}}(\boldsymbol{n}) = \Delta\boldsymbol{n}\boldsymbol{E}_c\Delta\boldsymbol{n}, \quad \boldsymbol{E}_c = \frac{e^2}{2}\hat{\boldsymbol{C}}. \tag{A.3}$$

The diagonal elements of the so called "charging energy matrix" $\boldsymbol{E}_c$ are called "charging energies", the off diagonal elements "coupling coefficients".

If some of the capacitances in the above problem are in fact tunneling contacts, the charge on some island might change by an integer number times elementary charge $e$. For this to happen, an electromotive force (emf) is requiered in general. As an example we now calculate the energy consumption during a tunneling event. In Fig. A.2 we connect an emf represented as tunable battery across an internal (left part of the figure) and a external (right part of the figure) capacitance. The inital voltage of this battery is given by $U^{\mathrm{in}}_{\mathrm{emf}} = U^{\mathrm{in}}_i - U^{\mathrm{in}}_j$ and $U^{\mathrm{in}}_{\mathrm{emf}} = V^{\mathrm{in}}_i - U^{\mathrm{in}}_j$, respectively, where the initial potentials are in accord with the initial charge state as expressed by Eq. A.1. We then transfer the required charge through the emf by tuning its voltage in infinitesimal steps. The final potential difference is again in accord with Eq. A.1 for the final state of the system. In each step the energy consumption amounts to $\mathrm{d}E = e(U_i - U_j)\mathrm{d}n$ where one has to replace $U_i$ by the constant $V_i$ for the case of an external contact. The total energy of the tunneling of an elementary charge is then

$$\Delta E = e\int_0^1 (U_i - U_j)\mathrm{d}n, \quad \Delta E = eV_i - e\int_0^1 U j\mathrm{d}n. \tag{A.4}$$

Eq. A.1 can be used to express $U_j$ and $U_i$ as a function of $\boldsymbol{n}$ and the evaluation of the integral yields:

$$\Delta E = E^{\mathrm{fi}}_{\mathrm{ch}} - E^{\mathrm{in}}_{\mathrm{ch}}, \quad \Delta E = E^{\mathrm{fi}}_{\mathrm{ch}} - E^{\mathrm{in}}_{\mathrm{ch}} + eV_i, \tag{A.5}$$

where $E^{\mathrm{in}}_{\mathrm{ch}}$ and $E^{\mathrm{fi}}_{\mathrm{ch}}$ are the charging energy of the initial and final charge state. This are of course the expected results. The latter of the two relations explicitely shows how energy is exchanged between the system of charged islands and the reservoirs during a tunneling event.

The SET transistor possesses only one island. The charging energy matrix is a scalar $E_c = e^2/2C_\Sigma$ and Eq. A.3 reads:

$$E_{\mathrm{ch}}(n) = E_c(n - n_0)^2, \quad en_0 = C_g V_g + (C_1 - C_2)V/2 \tag{A.6}$$

for a symmetric biasing[2]. Note that for a symmetric transistor—i.e. $C_1 = C_2$—the second term on the right hand side of the equationA.6 vanishes. The general situation is not different in a fundamental way.

For a discussion of the superconducting transistor in Sec. 2.3.1, it is convenient to include the work performed by the external source into the electrostatic part of the Hamiltonian. If $n_1$ and $n_2$ specify the number of electrons transferred through the corresponding junctions, this is done by

$$H_{\mathrm{el}} = E_c(\hat{n} - n_0)^2 + (n_1 + n_2)eV/2. \tag{A.7}$$

It is easy to see that Eq. A.7 is in accord with the second equation in A.5.

[2] I.e. the voltage bias across the transistor is equally distributed: $-V/2$ at the left and $V/2$ at the right junction.

# Bibliography


[Ågren 2002] ÅGREN, P.: *Charging effects in small capacitance Josephson junction circuits*, Royal Institute of Technology, PhD thesis, 2002

[Ågren et. al. 2002] ÅGREN, P. ; WALTER, J. ; HAVILAND, D.: Switching current of a Cooper pair transistor with tunable Josephson junctions. In: *Phys. Rev. B* 66 (2002), p. 014510

[Aleshkin and Averin 1990] ALESHKIN, V. Y. ; AVERIN, D. V.: Resonant tunneling of Cooper pairs in a double Josephson junction system. In: *Physica B* 165 (1990), p. 949–950

[Amar et. al. 1994] AMAR, A. ; SONG, D. ; LOBB, C. J. ; WELLSTOOD, F. C.: 2*e* to *e* periodic pair currents in superconducting Coulomb-blockade electrometers. In: *Phys. Rev. Lett.* 72 (1994), p. 3234–3237

[Ambegaokar and Baratoff 1963a] AMBEGAOKAR, V. ; BARATOFF, A.: Tunneling Between Superconductors. In: *Phys. Rev. Lett.* 10 (1963), p. 486–489

[Ambegaokar and Baratoff 1963b] AMBEGAOKAR, V. ; BARATOFF, A.: Tunneling Between Superconductors. In: *Phys. Rev. Lett.* 11 (1963), p. 104

[Ambegaokar and Halperin 1969] AMBEGAOKAR, Vinay ; HALPERIN, B. I.: Voltage Due to Thermal Noise in the dc Josephson Effect. In: *Phys. Rev. Lett.* 22 (1969), Jun, no. 25, p. 1364–1366

[Anderson and Rowell 1963] ANDERSON, P. W. ; ROWELL, J. M.: Probable Observation of the Josephson Superconducting Tunneling Effect. In: *Phys. Rev. Lett.* 10 (1963), p. 230–232

[Aparshina et. al. 1997] APARSHINA, L. I. ; DUBONOS, S. V. ; MAKSIMOV, S. V. ; SVINTSOV, A. A. ; ZAITSEV, S. I.: Energy dependence of proximity parameters investigated by fitting before measurement tests. In: *J. Vac. Sci. Technol. B* 15 (1997), no. 6, p. 2298–2302

[Aumentado et. al. 2004] AUMENTADO, J. ; KELLER, M. W. ; MARTINIS, J. M. ; DEVORET, M. H.: Nonequilibrium Quasiparticles and 2*e* Periodicity in Single-Cooper-Pair Transistors. In: *Phys. Rev. Lett.* 92 (2004), p. 066802

[Averin and Aleshkin 1989] AVERIN, D. V. ; ALESHKIN, V. Y.: Resonance tunneling of Cooper pairs in a system of two small Josephson junctions. In: *JETP Lett.* 50 (1989), p. 367–369

[Averin et. al. 1997] AVERIN, D. V. ; KOROTKOV, A. N. ; MANNINEN, A. J. ; PEKOLA, J. P.: Resonant Tunneling through a Macroscopic Charge State in a Superconducting Single Electron Transistor. In: *Phys. Rev. Lett.* 78 (1997), p. 4821

[Averin and Likharev 1991] AVERIN, D. V. ; LIKHAREV, K. K.: *Single electronics: a corelated transfer of single electrons and Cooper pairs in systems of small tunnel junctions*. p. 173–271. In: ALTSHULER, B. L. (Ed.) ; LEE, P. A. (Ed.) ; WEBB, R. A. (Ed.): *Mesoscopic Phenomena in Solids*, Niederlande: Elsevier Science Publishers B. V., 1991

[Averin and Likharev 1992] AVERIN, D. V. ; LIKHAREV, K. K.: *NATO ASI series, Series B, Physics*. vol. 294: *Macroscopic quantum tunneling of charge and co-tunneling*. p. 217–247. In: GRABERT, H. (Ed.) ; DEVORET, M. H. (Ed.): *Single Charge Tunneling: Coulomb Blockade Phenomena In Nano structures* vol. 294, New York Plenum Press, 1992. – ISBN 0-306-44229-9

[Averin and Nazarov 1992] AVERIN, D. V. ; NAZAROV, Yu. V.: Single-electron charging of a superconducting island. In: *Phys. Rev. Lett.* 69 (1992), p. 1993

[Bardeen et. al. 1957] BARDEEN, J. ; COOPER, L. N. ; SCHRIEFFER, J. R.: Theory of Superconductivity. In: *Phys. Rev.* 108 (1957), p. 1175–1204

[Baselmans et. al. 1999] BASELMANS, J. J. A. ; MORPURGO, A. F. ; WEES, B. J. van ; KLAPWIJK, T. M.: Reversing the direction of the supercurrent in a controllable Josephson junction. In: *Nature* 397 (1999), Jan, p. 43–45

[Billangeon et. al. 2007] BILLANGEON, P.-M. ; PIERRE, F. ; BOUCHIAT, H. ; DEBLOCK, R.: AC Josephson Effect and Resonant Cooper Pair Tunneling Emission of a Single Cooper Pair Transistor. In: *Phys. Rev. Lett.* 98 (2007), p. 216802

[Bladh et. al. 2003] BLADH, K. ; GUNNARSSON, D. ; HÜRFELD, E. ; DEVI, S. ; KRISTOFFERSSON, C. ; SMALANDER, B. ; PEHRSON, S. ; CLAESON, T. ; DELSING, P. ; TASLAKOV, M.: Comparison of cryogenic filters for use in single electronics experiments. In: *Rev. Sci. Instrum.* 74 (2003), p. 1323–1327

[Bouchiat 1997] BOUCHIAT, V.: *Quantum fluctuations of the charge in single electron and single Cooper pair devices*, l'Universite Paris 6, Thèse de Doctorat, PhD thesis, 1997

[Broers 1981] BROERS, A. N.: Resolution, Overlay and Field Size for Lithography Systems. In: *IEEE Trans. on Elec. Dev.* 28 (1981), no. 11, p. 1268–1278

[Cleuziou et. al. 2006] CLEUZIOU, J.-P. ; WERNSDORFER, W. ; BOUCHIAT, V. ; ONDARCUHU, T. ; MONTHIOUX, M.: Carbon nanotube superconducting quantum interference device. In: *Nat. Nano* 1 (2006), Oct, p. 53–59

[Ferguson et. al. 2006] FERGUSON, A. J. ; COURT, N. A. ; HUDSON, F. E. ; CLARK, R. G.: Microsecond Resolution of Quasiparticle Tunneling in the Single-Cooper-Pair Transistor. In: *Phys. Rev. Lett.* 97 (2006), p. 106603

[Fitzgerald et. al. 1998] FITZGERALD, R. J. ; POHLEN, S. L. ; TINKHAM, M.: Observation of Andreev reflection in all-superconducting single-electron transistors. In: *Phys. Rev. B* 57 (1998), p. R11073

[Fukushima et. al. 1997] FUKUSHIMA, A. ; SATO, A. ; IWASA, A. ; NAKAMURA, Y. ; KOMATSUZAKI, T. ; SAKAMATO, Y.: Attenuation of microwave filters for single-electron tunneling experiments. In: *IEEE Trans. Instrum. Meas.* 46 (1997), p. 289–293

[Fulton and Dolan 1987] FULTON, T. A. ; DOLAN, G. J.: Observation of single-electron charging effects in small tunnel junctions. In: *Phys. Rev. Lett.* 59 (1987), p. 109–112

[Fulton et. al. 1989] FULTON, T. A. ; GAMMEL, P. L. ; BISHOP, D. J. ; DUNKLEBERGER, L. N. ; DOLAN, G. J.: Observation of combined Josephson and charging effects in small tunnel junction circuits. In: *Phys. Rev. Lett.* 63 (1989), p. 1307–1310

[Geerligs et. al. 1990] GEERLIGS, L. J. ; ANDEREGG, V. F. ; ROMIJN, J. ; MOOJ, J. E.: Single Cooper-pair tunneling in small-capacitance junctions. In: *Phys. Rev. Lett.* 65 (1990), p. 377–380

[Glattli et. al. 1997] GLATTLI, D. C. ; JACQUES, P. ; KUMAR, A. ; PARI, P.: A noise detection scheme with 10 mK noise temperature resolution for semiconductor single electron tunneling devices. In: *J. Appl. Phys.* 81 (1997), p. 7350–7356

[Göppert and Grabert 2000] GÖPPERT, G. ; GRABERT, H.: Single electron tunneling in large conductance: the semiclassical approach. In: *Eur. Phys. J. B* 16 (2000), p. 687–706

[Grabert and Devoret 1992] GRABERT, H. ; DEVORET, M. H.: *NATO ASI series, Series B, Physics*. vol. 294: *Single Charge Tunneling: Coulomb Blockade Phenomena In Nanostru ctures*. New York Plenum Press, 1992. – ISBN 0-306-44229-9

[Haviland et. al. 1994] HAVILAND, D. B. ; HARADA, Y. ; DELSING, P. ; CHEN, C. D. ; CLAESON, T.: Observation of the Resonant Tunneling of Cooper Pairs. In: *Phys. Rev. Lett.* 73 (1994), p. 1541–1544

[Hilgenkamp et. al. 2003] HILGENKAMP, Hans ; ARIANDO ; SMILDE, Henk-Jan H. ; BLANK, Dave H. A. ; RIJNDERS, Guus ; ROGALLA, Horst ; KIRTLEY, John R. ; TSUEI, Chang C.: Ordering and manipulation of the magnetic moments in large-scale superconducting $\pi$-loop arrays. In: *Nature* 422 (2003), Mar, p. 50–53

[Hunklinger 2007] HUNKLINGER, S.: *Festkörperphysik*. Oldenbourg Wissenschaftsverlag GmbH, 2007. – ISBN 978-3-486-57562-0

[Ingold and Nazarov 1992] INGOLD, G.-L. ; NAZAROV, Yu. V.: *Charge Tunneling Rates in Ultrasmall Junctions*. p. 21–107. In: GRABERT, H. (Ed.) ; DEVORET, M. H. (Ed.): *Single Charge Tunneling: Coulomb Blockade Phenomena In Nanostru ctures*, New York Plenum Press, 1992

[Ivanchenko and Zilberman 1968] IVANCHENKO, Yu. M. ; ZILBERMAN, L. A.: The Josephson effect in small tunnel contacts. In: *Zh. Eksp. Teor. Fiz* 55 (1968), p. 2395–2402. – [Sov. Phys. JETP, **28**, 1272-1276 (1969)]

[Josephson 1962] JOSEPHSON, B. D.: Possible new Effects in Superconductive Tunnelling. In: *Physics Letters* 1 (1962), p. 251–253

[Joyez 1995] JOYEZ, P.: *Le transistor a une paire de Cooper: Un systeme quantique macroscopique*, l'Universite Paris 6, Thèse de Doctorat, PhD thesis, 1995

[Joyez et. al. 1997] JOYEZ, P. ; BOUCHIAT, V. ; ESTEVE, D. ; URBINA, C. ; DEVORET, M. H.: Strong tunneling in the single electron transistor. In: *Phys. Rev. Lett.* 79 (1997), p. 1349–1352

[Joyez et. al. 1994] JOYEZ, P. ; LAFARGE, P. ; FILIPE, A. ; ESTEVE, D. ; DEVORET, M. H.: Observation of parity-induced supression of Josephson tunneling in the superconducting single electron transistor. In: *Phys. Rev. Lett.* 72 (1994), p. 2458–2461

[Kouwenhoven et. al. 1997] KOUWENHOVEN, L. P. ; SCHÖN, G. ; SOHN, L. L.: *Introduction to Mesoscopic Electron Transport*. p. 1–44. In: SOHN, L. L. (Ed.) ; KOUWENHOVEN, L. P. (Ed.) ; SCHÖN, G. (Ed.): *Mesoscopic Electron Transport*, Kluwer Academic Publisher, Dordrecht/Boston/London, 1997

[Kubala et. al. 2006] KUBALA, B. ; JOHANSSON, G. ; KÖNIG, J: Transport in metallic multi-island Coulomb blockade systems: A systematic perturbative expansion in the junction transparency. In: *Phys. Rev. B* 73 (2006), p. 165316

[Leunissen et. al. 2004] LEUNISSEN, L. H. A. ; JONCKHEERE, R. ; HOFMANN, U. ; ÜNAL, N. ; KALUS, C.: Experimental and simulation comparison of electron-beam proximity correction. In: *J. Vac. Sci. Technol. B* 22 (2004), no. 6, p. 2943–2947

[Likharev 1986] LIKHAREV, K. K.: *Dynamics of Josephson Junctions and Circuits*. Philadelphia: Gordon and Breach, first edition, 1986. – ISBN 2-88124-042-9

[Limbach 1998] LIMBACH, Bernhard: *Untersuchung von Einzelelektronentransistoren auf der Basis von nanostrukturiertem Aluminium*, Universität Karlsruhe, diploma thesis, 1998

[Limbach 2002] LIMBACH, Bernhard: *Metallische Doppelinselstrukturen mit hohen Tunnelleitwerten*, Universität Karlsruhe, PhD thesis, 2002. – published by: Forschungszentrum Karlsruhe, Wissenschaftliche Berichte, FZKA 6791

[Lu et. al. 1996] LU, J. G. ; HERGENROTHER, J. M. ; TINKHAM, M.: Magnetic-field-induced crossover from 2e to e periodicity in the superconducting single-electron transistor. In: *Phys. Rev. B* 53 (1996), p. 3543–3549

[Manninen et. al. 1997] MANNINEN, A. J. ; PASHKIN, Yu. A. ; KOROTKOV, A. N. ; PEKOLA, J. P.: Obervation of thermally excited charge transport modes in a superconducting single-electron transistor. In: *Europhys. Lett.* 39 (1997), p. 305–310

[Martinis et. al. 1987] MARTINIS, John M. ; DEVORET, Michel H. ; CLARKE, John: Experimental test for the quantum behaviour of a macroscopic degree of freedom: the phase difference across a Josephson junc tion. In: *Phys. Rev. B* 35 (1987), p. 4682–4698

[Martinis and Nahum 1993] MARTINIS, John M. ; NAHUM, M.: Effect of environmental noise on the accuracy of Coulomb- blockade devices. In: *Phys. Rev. B* 48 (1993), p. 18316–18319

[Matveev et. al. 1993] MATVEEV, K. A. ; GISSELFÄLT, M. ; GLAZMAN, L. I. ; JONSON, M. ; SHEKHTER, R. I.: Parity-induced suppression of the Coulomb blockade of Josephson tunneling. In: *Phys. Rev. Lett.* 70 (1993), p. 2940–2943

[McCumber 1968] MCCUMBER, D. E.: Effect of ac Impedance on dc Voltage-Current Characteristics of Superconductor Weak-Link Junctions. In: *J. Appl. Phys.* 39 (1968), p. 3113

[Nakamura et. al. 1996] NAKAMURA, Y. ; CHEN, C. ; TSAI, J.: Quantitative analysis of Josephson quasiparticle current in superconducting single electron transistors. In: *Phys. Rev. B* 53 (1996), p. 8234

[Nakamura et. al. 1997] NAKAMURA, Y. ; KOROTKOV, A. N. ; CHEN, C. ; TSAI, J.: Singularity-matching peaks in a superconducting single-electron transistor. In: *Phys. Rev. B* 56 (1997), p. 5116

[Niemeyer 1974] NIEMEYER, Jürgen: Eine einfache Methode zur Herstellung kleiner Josephson-Elemente. In: *PTB-Mitteilungen* 73 (1974), no. 11, p. 2903–2906

[Pohlen et. al. 2000] POHLEN, S. L. ; FITZGERALD, R. J. ; TINKHAM, M.: The Josephson-quasiparticle (JQP) current cycle in the superconducting single-electron transistor. In: *Physica B* 284-288 (2000), p. 1812–1813

[Ryazanov et. al. 2000] RYAZANOV, V. V. ; OBOZNOV, V. A. ; RUSANOV, A. Y. ; VERETENNIKOV, A. V. ; GOLUBOV, A. A. ; AARTS, J.: Coupling of Two Superconductors through a Ferromagnet: Evidence for a $\pi$ Junction. In: *Phys. Rev. Lett.* 86 (2000), p. 2427–2430

[Schäfer et. al. 2007] SCHÄFER, R. ; LIMBACH, B. ; STEIN, P. vom ; WALLISSER, C.: Single-electron pump: Device characterization and linear-response measurements. In: *Electron Correlation in New Materials and Nanosystems* 241 (2007), p. 357–369

[Schoeller and Schön 1994] SCHOELLER, H. ; SCHÖN, G.: Mesoscopic quantum transport: Resonant tunneling in the presence of a strong Coulomb interaction. In: *Phys. Rev. B* 50 (1994), p. 18436–18452

[Stewart 1968] STEWART, W. C.: Current-voltage characteristics of Josephson junctions. In: *Appl. Phys. Lett.* 12 (1968), p. 277

[Sypli 1997] SYPLI, Anke: *Zur Untersuchung von Einzelelektroneneffekten in ultrakleinen Al-$Al_2O_3$-Al-Tunnelkontakten*, Universität Karlsruhe, PhD thesis, 1997. – published by: Forschungszentrum Karlsruhe, Wissenschaftliche Berichte, FZKA 6063

[Thévenin 1883] THÉVENIN: Extension de la loi d'Ohm aux circuits électromoteurs complexes. In: *Annales Télégraphiques* 10 (1883), p. 222–224

[Tinkham 1996] TINKHAM, M.: *Introduction to Superconductivity*. McGraw-Hill, Inc., 2nd ed., 1996

[Tsuei and Kirtley 2000] TSUEI, C. C. ; KIRTLEY, J. R.: Pairing symmetry in cuprate superconductors. In: *Rev. Mod. Phys.* 72 (2000), Oct, no. 4, p. 969

[Tuominen et. al. 1992] TUOMINEN, M. T. ; HERGENROTHER, J. M. ; TIGHE, T. S. ; TINKHAM, M.: Experimental evidence for parity-based 2*e* periodicity in a superconducting single-electron tunneling transistor. In: *Phys. Rev. Lett.* 69 (1992), p. 1997–2000

[Tuominen et. al. 1993] TUOMINEN, M. T. ; HERGENROTHER, J. M. ; TIGHE, T. S. ; TINKHAM, M.: Even-odd electron number effects in a small superconducting island: Magnetic-field dependence. In: *Phys. Rev. B* 47 (1993), p. 11599

[Van Harlingen 1995] VAN HARLINGEN, D. J.: Phase-sensitive tests of the symmetry of the pairing state in the high-temperature superconductors—Evidence for $dx2-y2$ symmetry. In: *Rev. Mod. Phys.* 67 (1995), Apr, no. 2, p. 515–535

[Vion et. al. 1995] VION, D. ; ORFILA, P. F. ; JOYEZ, P. ; ESTEVE, D. ; ; DEVORET, M. H.: Miniature electrical filters for single electron devices. In: *J. Appl. Phys.* 77 (1995), p. 2519–2524

[Wallisser 2002] WALLISSER, C.: *Einzelelektronentransistoren im Regime kleiner Widerstände*, Universität Karlsruhe, PhD thesis, 2002. – published by: Forschungszentrum Karlsruhe, Wissenschaftliche Berichte, FZKA 6712

[Wallisser et. al. 2002] WALLISSER, C. ; LIMBACH, B. ; STEIN, P. vom ; SCHÄFER, R. ; THEIS, C. ; GOPPERT, G. ; GRABERT, H.: Conductance of the single-electron transistor: A comparison of experimental data with Monto Carlo calculations. In: *Phys. Rev. B* 66 (2002), p. 125314

[Zorin 1995] ZORIN, A. B.: The thermocoax cable as the microwave frequency filter for single electron circuits. In: *Rev. Sci. Instrum.* 66 (1995), p. 4296–4300

# Acknowledgments

It has been almost four years since I came to this group and there are several people I would like to take this chance to acknowledge. First of all I would like to thank Prof. Hilbert v. Löhneysen for taking me into this institute and giving me a chance to study here. I am indebted to Professor Alexey Ustinov for his referring my thesis and making important suggestions. I would like to thank Dr. Roland Schäfer for helping me with everything, from every experimental techniques to the theoretical understandings. I really learned a lot from his broad knowledge. I would thank Birgit Kießig for our good cooperation. As well as my work is concerned, it would not be possible for me to do this work without Christoph Kaiser, Stefan Wünsch from IMS, Uni Karlsruhe. I would also like to thank everybody in the IFP, Forschungszentrum Karlsruhe for creating a stimulating and inspiring research environment. Furthermore, I would like to thank our secretary, Frau Maass, for all the administrative things she did for me. Finally, I thank very much my lunch colleagues. Staying with you guys makes me feel like at home.

On a personal, I would like to thank my parents and grandmother for their support and confidence in me. My friends, from China and Germany, thank you for all the fun we shared together. Finally, and above all, I devote this thesis to Liqun. Thank you so much for your unconditional love and support, especially during the process of writing this thesis. Your love is the best treasure I ever found in my life!